Synthesis and Characterization of New Sodium Ion Conductors

Dissertation

Zur Erlangung des Doktorgrades

der Naturwissenschaften (Dr. rer. nat.) der Fakultät für

Chemie und Pharmazie

der Universität Regensburg

submitted by

Franziska Kamm

from Regensburg

2024

The practical work was performed from July 2021 to June 2024 at the Institute of Inorganic Chemistry at the University of Regensburg in the working group of Prof. Dr. Arno Pfitzner.
This work incorporates results of my master thesis *"Präparative und strukturchemische Untersuchungen an neuen Na Ionenleitern"* which was submitted to the Faculty of Chemistry and Pharmacy at the University of Regensburg in 2021.

This work was supervised by Prof. Dr. Arno Pfitzner.
Submission of the PhD: 16.09.2024
Date of the oral exam: 06.12.2024

Examination Committee:
Chairman: Prof. Dr. Dominik Horinek
1. Examiner: Prof. Dr. Arno Pfitzner
2. Examiner: Prof. Dr. Richard Weihrich
Further examiner: Prof. Dr. Frank-Michael Matysik

Danksagung

Die Anfertigung der vorliegenden Arbeit wäre ohne die Unterstützung vieler Menschen nicht möglich gewesen. Aus diesem Grund möchte ich folgenden Personen danken:

Prof. Dr. Arno Pfitzner für die Möglichkeit zur Durchführung dieser Arbeit, die Freiheiten bei der Themenwahl, die fachlichen Diskussionen und seine fortwährende Unterstützung.

Dr. Florian Pielnhofer für seine Unterstützung bei allen theoretischen Fragestellungen und für die vielen fachlichen Diskussionen und freundschaftlichen Gespräche.

Dr. Marc Schlosser für die Unterstützung in allen Angelegenheiten rund um die Pulverdiffraktometrie und seine große Hilfsbereitschaft.

Bianca Heiligtag, Katharina Trögl und Steffi Meinel für die Hilfe bei allen organisatorischen Angelegenheiten.

Dr. Stefanie Gärtner und Dr. Michael Bodensteiner für die Messzeit am Einkristalldiffraktometer und die Unterstützung bei allen Fragestellungen rund um die Einkristalldiffraktometrie.

Ulrike Schießl für die Durchführung der thermischen Analysen.

Florian Truksa für seine Unterstützung bei allen technischen Angelegenheiten und die Präparation der DTA-Proben.

Florian Wegner für die Einweisung in die Bedienung der Impedanzanlage und der Gloveboxen, die Einführung in die Pulverdiffraktometrie, die vielen Ratschläge und freundschaftlichen Gespräche und die sehr gute Laborkameradschaft.

Elisabeth Huf für die hervorragende Zusammenarbeit, die sehr gute Laborkameradschaft und die vielen freundschaftlichen Gespräche.

Martin Schmid für die sehr gute Zusammenarbeit, die vielen wissenschaftlichen Diskussionen und freundschaftlichen Gespräche.

Sven Schedlowski für die vielen fachlichen und freundschaftlichen Gespräche und aufmunternde Worte.

Daniel Schmidhuber für seine große Hilfsbereitschaft und Unterstützung bei allen IT-Problemen und die vielen freundschaftlichen Gespräche.

Susan Rank, Lea Huber, Rafal Samp, Julian Schiller, Martin Rosenhammer, Dr. Philipp Schmid, Dr. Maximilian Sehr, Dr. Salil Bal, Ferdinand Gigl und allen anderen aktuellen und ehemaligen Mitgliedern des Lehrstuhls von Prof. Dr. Arno Pfitzner für den angenehmen Arbeitsalltag und die tolle Stimmung.

Meinen Forschungspraktikanten Hornela-Emma Motoum-Defo, Francesco Cirigliano und Georg Nowotny für die Unterstützung bei präparativen Arbeiten.

Mein besonderer Dank gilt meiner Familie und meinem Freund Michael für ihre stetige Unterstützung während dieser Zeit.

Eidesstattliche Erklärung

Ich erkläre hiermit an Eides statt, dass ich die vorliegende Arbeit ohne unzulässige Hilfe Dritter und ohne Benutzung anderer als die angegebenen Hilfsmittel angefertigt habe. Die aus anderen Quellen direkt oder indirekt übernommenen Daten und Konzepte sind unter Angabe des Literaturzitats gekennzeichnet. Die Arbeit wurde bisher weder im In- noch im Ausland in gleicher oder ähnlicher Form einer anderen Prüfungsbehörde vorgelegt. Ich versichere an Eides statt, dass ich nach bestem Wissen die reine Wahrheit gesagt und nichts verschwiegen habe.

Regensburg, September 2024

Franziska Kamm

Preface

These results have already been published during the preparation of this work. The relevant content is reprinted with the permission of the respective scientific publisher. Each chapter includes a list of authors and a description of the individual contribution of each author.

In the beginning of this thesis, a general introduction and objectives of the work are presented together with a comprehensive conclusion at the end of this thesis.

Publications

The presented results have already been published:

Franziska Kamm, Florian Pielnhofer, Marc Schlosser, Arno Pfitzner
Synthesis and Characterization of $Na_4Si_2Se_6$-$tP24$ and $Na_4Si_2Se_6$-$oP48$, Two Polymorphs with different anionic structures
Inorganic Chemistry **2023**, *62*, 11064-11072.

Franziska Kamm, Florian Pielnhofer, Arno Pfitzner
Sodium Selenotetrelates with isolated TtSe$_4$-Tetrahedra (Tt = Si, Ge, Sn): Synthesis, Crystal Structures, Thermal Behavior, DFT Modeling and Na Ion Conductivities
Chemistry of Materials **2024**, *36*, 5643-5650.

Franziska Kamm, Florian Pielnhofer, Marc Schlosser, Arno Pfitzner
Enhanced sodium ion mobility in sodium tellurosilicates and crystal structures of Na_4SiTe_4 and $Na_{10}Si_2Te_9$ with isolated $[SiTe_4]^{4-}$ tetrahedra and isolated Te^{2-} anions
Dalton Transactions **2024**, DOI: 10.1039/d4dt01717j.

Contributions were also made to the following publications:

Florian Wegner, Franziska Kamm, Florian Pielnhofer, Arno Pfitzner
Li_3P und Li_3As revisited: DFT modelling on phase stability and ion conductivity
Zeitschrift für anorganische und allgemeine Chemie **2022**, *648*, e202100358.

Florian Wegner, Franziska Kamm, Florian Pielnhofer, Arno Pfitzner
Li_3TrAs_2 (Tr = Al, Ga In) - Derivatives of the antifluorite type structure, Conductivities and electronic structures
Zeitschrift für anorganische und allgemeine Chemie **2022**, *649*, e202200330.

Xiaoyu Song, Ratnadwip Singha, Guangming Cheng, Yao-Wen Yeh, Franziska Kamm, Jason F. Khoury, Brianna L. Hoff, Joseph W. Stiles, Florian Pielnhofer, Philip E. Batson, Nan Yao, Leslie M. Schoop
Synthesis of an aqueous, air-stable, superconducting 1T'-WS_2 monolayer ink
Science Advances **2023**, *9*, eadd6167.

Xiaoyu Song, Brianna Hoff, Ratnadwip Singha, Joseph W. Stiles, Grigorii Skorupskii, Jason F. Khoury, Guangming Cheng, Franziska Kamm, Ayelet J. Uzan, Stephanie Dulovic, Sanfeng Wu, Florian Pielnhofer, Nan Yao, Leslie M. Schoop
Acid-Assisted Soft Chemical Route for Preparing High-Quality Superconducting 2M-WS_2
Chemistry of Materials **2023**, *35*, 5487-5496.

Connor J. Pollak, Grigorii Skorupskii, Martin Gutierrez-Amigo, Ratnadwip Singha, Joseph W. Stiles, Franziska Kamm, Florian Pielnhofer, N. P. Ong, Ion Errea, Maia G. Vergniory, Leslie M. Schoop
Chemical Bonding Induces One-Dimensional Physics in Bulk Crystal $BiIr_4Se_8$
Journal of the American Chemical Society **2024**, *146*, 6784-6795.

Table of Contents

1 Introduction

In recent years, there has been a continuously growing consciousness for the protection of the environment. Hence, energy production from renewable sources is favoured over the usage of fossil resources to reduce the carbon emissions and the development and expansion of photovoltaic and wind power plants is being promoted. Besides reduction of carbon emissions these energy production systems offer further advantages. They can be built in decentralized locations near consumers of the produced energy without environmental pollution and without severe security hazards which can occur, for example at nuclear power plants.

A great disadvantage of photovoltaic and wind plants is their changing energy output over time because of the weather dependency. Thus, a highly efficient energy storage system is needed to enable a constant supply of energy, which is not dependent on daytime or seasonal climatic changes. The development of energy storage systems with high efficiency and high capacity has become more important in recent years. There are various possibilities to store electricity.[1,2] Pumped-storage of water offers high capacities but requires special locations. It is also possible to store electricity via production and storage of hydrogen which can then be used in fuel cells, but especially the storage of hydrogen remains challenging.[3] A further option is the usage of batteries for energy storage.

In principle, batteries are composed of several electrochemical cells. Each cell contains two electrodes which are separated by an electrolyte. For electrodes and electrolytes several possible materials can be used. Due to their high energy density, lithium-ion batteries are the most common rechargeable batteries.[4] Therein, electrodes are made of host structure materials where lithium can be inserted and extracted reversibly. Materials like spinels ($LiMn_2O_4$), phosphates ($LiFePO_4$) and oxides ($Li[Ni_xCo_yMn_z]O_2$) are employed as cathodes.[5–9] Graphite is used as an anode material commonly, where lithium can be inserted and extracted.[10] The main disadvantage of commercially available lithium ion batteries is the contained liquid organic electrolytes which are flammable and raise safety concerns.[11] This disadvantage is eliminated in all-solid-state batteries, making them a promising option for future battery systems.[12]

After concentrating on lithium based systems, research on sodium based batteries recently emerged.[1] Due to the higher abundance of sodium in comparison to lithium (2.7 wt% vs. 0.002 wt% in the earth's crust) sodium based battery systems could be produced cheaper.[13] Furthermore, lithium is unevenly distributed in the earth's crust. Its limited

availability in only a few countries leads to concerns on sustainability and political issues. In contrast, sodium is largely abundant, e.g. in seawater. The setup and working principle of batteries does not change upon the exchange of lithium by sodium so that facilities and equipment for lithium batteries could be also used for the production of sodium batteries.[14] Despite that, also new challenges arise from the exchange of lithium with sodium, as the cell chemistry differs.[4]

With the discovery of very high sodium ion conductivity in β-alumina ($NaAl_{11}O_{17}$) two types of high-temperature sodium batteries, the Na/S and the ZEBRA (**Ze**olite **B**attery **R**esearch **A**frica) batteries, were developed.[15–17] Both battery types are usually operated at 300 °C to 350 °C where the sodium anode is molten and the ion conductivity in solid β-alumina is enhanced.

Analogous to the lithium battery technology, sodium ion batteries based on intercalation materials are conceivable for room temperature applications. The use of graphite as anode material is not possible for sodium batteries as Na^+ can not be intercalated efficiently. Instead, different anode materials have been developed.[18] As negative electrode materials hard carbon[19–21] can be used, which is composed of graphene-like carbon layers and micropores or metal oxides.[22] Sodium intercalation compounds like transition metal oxides or ferrocyanides as prussian white ($Na_{1.92}Fe[Fe(CN)_6]$) can be deployed as cathodes.[23,24] In recent years, several companies announced to be close to commercialization of sodium ion batteries.[25,26] CATL, a manufacturer of lithium ion batteries, presented its first sodium ion battery in 2021.[27] In 2023, Northvolt also added a sodium ion battery to its portfolio.[28] Both batteries are built with prussian-white cathodes and hard-carbon anodes.

For future battery systems, all-solid-state batteries (ASSBs) became promising concepts. Non-flammable ceramic electrolytes could eliminate safety issues and allow new battery designs to improve the packing efficiency of the cells.[12] They are also favorable due to their possible high energy density, especially upon usage of Li or Na metal anodes.[29]

One of the key components of these ASSBs is the solid electrolyte which must fulfill various requirements such as high ionic conductivity ($> 1 \times 10^{-3}\,S\,cm^{-1}$) and chemical stability.[30] High sodium ion conductivities were found in NASICON-type (**Na**-**S**uper**i**onic **Con**ductor) compounds, e.g. $Na_{1+x}Zr_2P_{3-x}Si_xO_{12}$ ($0 \leq x \leq 3$).[31,32] By incorporation of NASICON electrolytes all-solid-state batteries can be even operated at room temperature.[33,34]

Another promising candidate for solid electrolytes are thiophosphates, e.g. Na_3PS_4.[35,36]

To enhance the ionic conductivity Na_3PS_4 can be doped with halides X (X = Cl, Br) to increase the amount of vacancies.[37,38] Also the incorporation of tetrels Tt (Tt = Si, Ge, Sn) results in an enhanced ionic conductivity.[39–42] The substitution of S with Se increases the ionic conductivity further.[43–45] This is explained by the hypothesis that a softer lattice leads to lower activation barriers of ion migration.[46]

In the present work, compounds in the systems Na-Tt-Q with Tt = Si, Ge, Sn and Q = Se, Te were investigated. Only few materials containing these elements were characterized in the past. The focus was set on the structural investigation but their physical and chemical properties are still unknown. The emerging interest in sodium ion conductors arouses interest in a reinvestigation of the corresponding system. Using mechanochemical methods allows synthesis of phase pure powder samples of literature known compounds which are needed for the investigation of sodium ion conductivities. It also gives access to new compounds and new modifications of already known compounds.
In the following, a general overview of already known compounds in the considered systems is given. They can be classified e.g. with respect to their anionic unit. In Table 1.1 literature known compounds are listed including their space groups and structure types. Several new compounds, which were synthesized and characterized during this work, are also included. In most compounds, the anionic units consist of TtQ_4 tetrahedra which are connected in different ways. The simplest anionic units are isolated tetrahedra which are e.g. found in sodium selenotetrelates Na_4TtSe_4 (Chapter 3) and Na_4SiTe_4 (Chapter 5). The first example of edge-sharing tetrahedra is $Na_4Si_2Se_6$-$tP24$ (Chapter 4). The compound is also the first representative of a material with two different polymorphs containing different anionic units.
Besides anionic units based on TtQ_4 tetrahedra, ethane-like units with a Tt-Tt bond were found, e.g. in $Na_6Si_2Te_6$[47] and $Na_8Si_4Te_{10}$[48] (Chapter 5).

Table 1.1 Overview of new and literature known sodium chalcogenotetrelates.

Anionic Unit	Compound	Space Group	Structure Type
isolated tetrahedra TtQ_4^{4-}	Na_4SiSe_4-$oP36$[49]	$Pnma$ (no. 62)	K_4SnSe_4[50]
	Na_4SiSe_4-$cP72$	$P\bar{4}3n$ (no. 218)	Ba_4SiAs_4[51]
	Na_4GeSe_4[52]	$Pnma$ (no. 62)	own type
	Na_4SnSe_4-$tP18$[50]	$P\bar{4}2_1c$ (no. 114)	Na_4SnS_4[53]
	Na_4SnSe_4-$tI216$	$I4_1/acd$ (no. 142)	Na_4SnTe_4-$tI216$[54]
	Na_4SiTe_4	$Pa\bar{3}$ (no. 208)	own type
	$Na_{10}Si_2Te_9$	$Pna2_1$ (no. 33)	own type
	Na_4SnTe_4[55]	$P2_12_12_1$ (no. 19)	own type
edgesharing tetrahedra $Tt_2Q_6^{4-}$	$Na_4Si_2Se_6$-$tP24$[56]	$P4_2/mcm$ (no. 132)	own type
cornersharing tetrahedra $Tt_2Q_7^{6-}$	$Na_6Si_2Se_7$[57]	$C12/c1$ (no. 15)	$Na_6Sn_2Se_7$
	$Na_6Ge_2Se_7$[58]	C12/c1 (no. 15)	$Na_6Sn_2S_7$[59]
	$Na_6Sn_2Se_7$[60]	C12/c1 (no. 15)	$Na_6Sn_2S_7$
Tt dumbbells $Tt_2Q_6^{6-}$ / $Tt_4Q_{10}^{8-}$	$Na_6Ge_2Se_6$[61]	$P12_1/c1$ (no. 14)	$K_6Sn_2Te_6$[62]
	$Na_6Si_2Te_6$[47]	$P12_1/c1$ (no. 14)	$K_6Sn_2Te_6$
	$Na_6Ge_2Te_6$[63]	$P12_1/c1$ (no. 14)	$K_6Sn_2Te_6$
	$Na_8Ge_4Se_{10}$[64]	$P12_1/c1$ (no. 14)	$Na_8Ge_4Te_{10}$[48]
	$Na_8Ge_4Se_{10}$[61]	$P\bar{1}$ (no. 2)	own type
	$Na_8Si_4Te_{10}$[48]	$P12_1/c1$ (no. 14)	$Na_8Ge_4Te_{10}$
	$Na_8Ge_4Te_{10}$[48]	$P12_1/c1$ (no. 14)	own type
	$Na_8Ge_4Te_{10}$[65]	$P\bar{1}$ (no. 2)	own type
Se-Se bond	$Na_6Si_2Se_8$[66]	$P12_1/c1$ (no. 14)	own type
Adamantan analogous Tt_4Q_{10} 4^-	$Na_4Si_4Se_{10}$[64]	$Cmcm$ (no. 63)	$Na_4Ge_4S_{10}$[67]
	$Na_4Ge_4Se_{10}$[68]	$Cmcm$ (no. 63)	$Na_4Ge_4S_{10}$
chains	$Na_4Si_2Se_6$-$oP48$[56]	$Pbca$ (no. 61)	own type
	$Na_4Ge_2Se_6$[64]	$P12_1/c1$ (no. 14)	Na_2GeS_3
	$Na_4Sn_2Se_6$[69]	$P12_1/c1$ (no. 14)	Na_2GeS_3
	$Na_{12}Sn_6Se_{18}$[70]	$Pnma$ (no. 62)	own type
layered structures	$Na_2Ge_2Se_5$[71]	$Pna2_1$ (no. 33)	own type
	$Na_2Sn_2Se_5$[72]	$Pbca$ (no. 61)	$Ga_2Pb_2S_5$[73]

References

[1] Delmas, C. *Adv. Energy Mater.* **2018**, *8*, 1703137.

[2] Dunn, B.; Kamath, H.; Tarascon, J.-M. *Science* **2011**, *334*, 928–935.

[3] Stetson, N.; Wieliczko, M. *MRS Energy & Sustainability* **2020**, *7*, 41.

[4] Nayak, P. K.; Yang, L.; Brehm, W.; Adelhelm, P. *Angew. Chem. - Int. Ed.* **2018**, *57*, 102–120.

[5] Goodenough, J. B.; Kim, Y. *Chem. Mater.* **2010**, *22*, 587–603.

[6] Thackeray, M.; Johnson, P.; de Picciotto, L.; Bruce, P.; Goodenough, J. *Mater. Res. Bull.* **1984**, *19*, 179–187.

[7] Padhi, A. K.; Nanjundaswamy, K. S.; Goodenough, J. B. *J. Electrochem. Soc.* **1997**, *144*, 1188.

[8] Ohzuku, T.; Makimura, Y. *Chem. Lett.* **2003**, *30*, 642–643.

[9] Noh, H.-J.; Youn, S.; Yoon, C. S.; Sun, Y.-K. *J. Power Sources* **2013**, *233*, 121–130.

[10] Winter, M.; Besenhard, J. O.; Spahr, M. E.; Novák, P. *Adv. Mater.* **1998**, *10*, 725–763.

[11] Goodenough, J. B. *J. Solid State Electr.* **2012**, *16*, 2019–2029.

[12] Li, J.; Ma, C.; Chi, M.; Liang, C.; Dudney, N. J. *Adv. Energy Mater.* **2015**, *5*, 1401408.

[13] Wiberg, N.; Wiberg, E.; Holleman, A. F., *Anorganische Chemie*, 103rd ed.; De Gruyter: 2017.

[14] Hu, Y.-S.; Lu, Y. *ACS Energy Lett.* **2019**, *4*, 2689–2690.

[15] Kummer, J. *Prog. Solid State Chem.* **1972**, *7*, 141–175.

[16] Dustmann, C.-H. *J. Power Sources* **2004**, *127*, 85–92.

[17] Lu, X.; Xia, G.; Lemmon, J. P.; Yang, Z. *J. Power Sources* **2010**, *195*, 2431–2442.

[18] Kang, H.; Liu, Y.; Cao, K.; Zhao, Y.; Jiao, L.; Wang, Y.; Yuan, H. *J. Mater. Chem. A* **2015**, *3*, 17899–17913.

[19] Babu, R. S.; Pyo, M. *J. Electrochem. Soc.* **2014**, *161*, A1045.

[20] Hong, K.-l.; Qie, L.; Zeng, R.; Yi, Z.-q.; Zhang, W.; Wang, D.; Yin, W.; Wu, C.; Fan, Q.-j.; Zhang, W.-x.; Huang, Y.-h. *J. Mater. Chem. A* **2014**, *2*, 12733–12738.

[21] Zhou, X.; Guo, Y.-G. *ChemElectroChem* **2014**, *1*, 83–86.

[22] Jiang, Y.; Zhang, Z.; Liao, H.; Zheng, Y.; Fu, X.; Lu, J.; Cheng, S.; Gao, Y. *ACS Nano* **2024**, DOI: 10.1021/acsnano.4c00613.

[23] Billaud, J.; Clément, R. J.; Armstrong, A. R.; Canales-Vázquez, J.; Rozier, P.; Grey, C. P.; Bruce, P. G. *J. Am. Chem. Soc.* **2014**, *136*, 17243–17248.

[24] Wang, L.; Song, J.; Qiao, R.; Wray, L. A.; Hossain, M. A.; Chuang, Y.-D.; Yang, W.; Lu, Y.; Evans, D.; Lee, J.-J.; Vail, S.; Zhao, X.; Nishijima, M.; Kakimoto, S.; Goodenough, J. B. *J. Am. Chem. Soc.* **2015**, *137*, 2548–2554.

[25] Hasa, I.; Barker, J.; Elia, G.; Passerini, S. In *Reference Module in Chemistry, Molecular Sciences and Chemical Engineering*; Elsevier: 2023.

[26] Bartoli, M. et al. *Renewable Sustainable Energy Rev.* **2024**, *194*, 114304.

[27] CATL Unveils Its Latest Breakthrough Technology by Releasing Its First Generation of Sodium-ion Batteries, https://www.catl.com/en/news/665.html, accessed: 11.03.2024.

[28] Northvolt develops state-of-the-art sodium-ion battery validated at 160 Wh/kg, https://northvolt.com/articles/northvolt-sodium-ion, accessed: 08.03.3024.

[29] Janek, J.; Zeier, W. G. *Nat. Energy* **2016**, *1*, 16141.

[30] Zhang, Z.; Shao, Y.; Lotsch, B.; Hu, Y.-S.; Li, H.; Janek, J.; Nazar, L. F.; Nan, C.-W.; Maier, J.; Armand, M.; Chen, L. *Energy Environ. Sci.* **2018**, *11*, 1945–1976.

[31] Hong, H.-P. *Mater. Res. Bull.* **1976**, *11*, 173–182.

[32] Goodenough, J.; Hong, H.-P.; Kafalas, J. *Mater. Res. Bull.* **1976**, *11*, 203–220.

[33] Naranjo-Balseca, J. M.; Martínez-Cisneros, C. S.; Pandit, B.; Várez, A. *J. Eur. Ceram. Soc.* **2023**, *43*, 4826–4836.

[34] Pandit, B.; Johansen, M.; Andersen, B. P.; Martínez-Cisneros, C. S.; Levenfeld, B.; Ravnsbæk, D. B.; Varez, A. *Chem. Eng. J.* **2023**, *472*, 144509.

[35] Jansen, M.; Henseler, U. *J. Solid State Chem.* **1992**, *99*, 110–119.

[36] Hayashi, A.; Noi, K.; Tanibata, N.; Nagao, M.; Tatsumisago, M. *J. Power Sources* **2014**, *258*, 420–423.

[37] De Klerk, N. J. J.; Wagemaker, M. *Chem. Mater.* **2016**, *28*, 3122–3130.

[38] Chu, I.-H.; Kompella, C. S.; Nguyen, H.; Zhu, Z.; Hy, S.; Deng, Z.; Meng, Y. S.; Ong, S. P. *Sci. Rep.* **2016**, *6*, 33733.

[39] Tanibata, N.; Noi, K.; Hayashi, A.; Tatsumisago, M. *RSC Adv.* **2014**, *4*, 17120–17123.

[40] Richards, W. D.; Tsujimura, T.; Miara, L. J.; Wang, Y.; Kim, J. C.; Ong, S. P.; Uechi, I.; Suzuki, N.; Ceder, G. *Nat. Commun.* **2016**, *7*, 11009.

[41] Duchardt, M.; Ruschewitz, U.; Adams, S.; Dehnen, S.; Roling, B. *Angew. Chem. - Int. Ed.* **2018**, *57*, 1351–1355.

[42] Zhang, Z.; Ramos, E.; Lalère, F.; Assoud, A.; Kaup, K.; Hartman, P.; Nazar, L. F. *Energy Environ. Sci.* **2018**, *11*, 87–93.

[43] Zhang, L.; Yang, K.; Mi, J.; Lu, L.; Zhao, L.; Wang, L.; Li, Y.; Zeng, H. *Adv. Energy Mater.* **2015**, *5*, 1501294.

[44] Krauskopf, T.; Pompe, C.; Kraft, M. A.; Zeier, W. G. *Chem. Mater.* **2017**, *29*, 8859–8869.

[45] Krauskopf, T.; Muy, S.; Culver, S. P.; Ohno, S.; Delaire, O.; Shao-Horn, Y.; Zeier, W. G. *J. Am. Chem. Soc.* **2018**, *140*, 14464–14473.

[46] Brüesch, P.; Pietronero, L.; Strässler, S.; Zeller, H. R. *Phys. Rev. B* **1977**, *15*, 4631–4637.

[47] Eisenmann, B.; Schwerer, H.; Schäfer, H. *Z. Naturforsch. B* **1981**, *36*, 1538–1541.

[48] Eisenmann, B.; Schwerer, H.; Schäfer, H. *Rev. Chim. Minér.* **1983**, *20*, 78–87.

[49] Preishuber-Pflügl, H.; Klepp, K. O. *Z. Kristallogr. - New Cryst. Struct.* **2003**, *218*, 383–384.

[50] Klepp, K. O. *Z. Naturforsch. B* **1992**, *47*, 411–417.

[51] Eisenmann, B.; Jordan, H.; Schäfer, H. *Z. Anorg. Allg. Chem.* **1981**, *475*, 74–80.

[52] Klepp, K. O. *Z. Naturforsch. B* **1985**, *40*, 878–882.

[53] Jumas, J.-C.; Philippot, E.; Vermot-Gaud-Daniel, F.; Ribes, M.; Maurin, M. *J. Solid State Chem.* **1975**, *14*, 319–327.

[54] Zagler, R. Darstellung und Strukturchemie von Chalkogenido-Polyanionen und Chalkogenidoindaten, -germanaten, -stannaten, -arsenaten, -antimonaten bzw. -telluraten mit komplexierten und nicht komplexierten Kationen, Ph.D. Thesis, Universität Darmstadt, 1988.

[55] Eisenmann, B.; Schäfer, H.; Schrod, H. *Z. Naturforsch. B* **1983**, *38*, 921–923.

[56] Kamm, F.; Pielnhofer, F.; Schlosser, M.; Pfitzner, A. *Inorg. Chem.* **2023**, *62*, 11064–11072.

[57] Eisenmann, B.; Hansa, J. *Z. Kristallogr. - Cryst. Mater.* **1993**, *203*, 295–296.

[58] Eisenmann, B.; Hansa, J.; Schäfer, H. *Rev. Chim. Minér.* **1986**, *23*, 8–13.

[59] Krebs, B.; Schiwy, W. *Z. Anorg. Allg. Chem.* **1973**, *398*, 63–71.

[60] Eisenmann, B.; Hansa, J. *Z. Kristallogr. - Cryst. Mater.* **1993**, *203*, 297–298.

[61] Eisenmann, B.; Hansa, J.; Schäfer, H. *Mater. Res. Bull.* **1985**, *20*, 1339–1346.

[62] Dittmar, G. *Z. Anorg. Allg. Chem.* **1979**, *453*, 68–78.

[63] Eisenmann, B.; Kieselbach, E.; Schäfer, H.; Schrod, H. *Z. Anorg. Allg. Chem.* **1984**, *516*, 49–54.

[64] Eisenmann, B.; Hansa, J.; Schäfer, H. *Z. Naturforsch. B* **1985**, *40*, 450–457.

[65] Eisenmann, B.; Schäfer, H.; Schwerer, H. *Z. Naturforsch. B* **1983**, *38*, 924–929.

[66] Eisenmann, B.; Hansa, J.; Schäfer, H. *Z. Anorg. Allg. Chem.* **1985**, *526*, 55–59.

[67] Philippot, E.; Ribes, M.; Lindqvist, O. *Rev. Chim. Minér.* **1971**, *8*, 477–489.

[68] Eisenmann, B.; Hansa, J. *Z. Kristallogr. - Cryst. Mater.* **1993**, *205*, 325–326.

[69] Eisenmann, B.; Hansa, J. *Z. Kristallogr. - Cryst. Mater.* **1993**, *203*, 291–292.

[70] Eisenmann, B.; Hansa, J. *Z. Kristallogr. - Cryst. Mater.* **1993**, *203*, 293–294.

[71] Eisenmann, B.; Hansa, J.; Schäfer, H. *Rev. Chim. Minér.* **1984**, *21*, 817–823.

[72] Klepp, K. O.; Hainz, M. *Z. Anorg. Allg. Chem.* **2000**, *626*, 863–866.

[73] Mazurier, A.; Jaulmes, S.; Guittard, M. *Acta Crystallogr. B* **1980**, *36*, 1990–1993.

2 Theory and Methods

2.1 Ionic Conductivity

The conductivity of solid state materials is based on the diffusion of particles through the material. In case of electrons and holes as mobile particles this conductivity is called electronic conductivity. In case of ions as mobile particles it is referred to as ionic conductivity. Generally, ionic conductivity can be understood as a hopping process from an occupied to a neighboring unoccupied lattice site. To enable this process, an activation barrier must be overcome.

The conductivity is specified as σ_{spec} in $\Omega^{-1}\,\mathrm{cm}^{-1}$ or $\mathrm{S}\,\mathrm{cm}^{-1}$, respectively. The aforementioned conduction mechanisms differ in their temperature dependence. The electronic conductivity of metals decreases with increasing temperature because of the increasing lattice vibrations. In contrast, for semiconductors and ion conductors the conductivity increases with increasing temperature. In many materials, e. g. CuCl, electronic and ionic conductivity occur simultaneously.[1] These materials are referred to as mixed conductors.

To enable the application of solid ionic conductors electrolytes in solid state batteries, the materials must exhibit a very high ionic conductivity. In particular defects in the crystal lattice are decisive for ionic conductivity. Ion diffusion can only occur if there are either vacant sites available or some interstitial sites are occupied. This is again linked to the temperature as higher defect concentrations are generated by increasing temperature.

Lattice defects can be classified by their dimensionality as 0D, 1D-, 2D- oder 3D-defects. The most important zero-dimensional defects, also known as point defects, are Frenkel and Schottky defects. In Frenkel defects, interstitial lattice sites are occupied, resulting in vacant positions in the crystal lattice. Schottky defects involve missing cations and anions resulting in vacant lattice positions.[2–4]

Apart from vacancy-mediated conduction there are some materials exhibiting conductivities as high as liquid electrolytes. The so called superionic conductors often possess crystal structures with tunnels or layers through which the ions can move. In order to obtain a significantly high ionic conductivity several conditions must be satisfied. There should be a large number of the mobile species and enough empty sites available in the crystal structure for the ions to diffuse into.[4] A similar potential energy between initial and final state of the ion jump increases the probability of successful jumps.[5] During the jump, an activation barrier needs to be passed. This barrier is lower for face-sharing polyhedra

than for edge-sharing polyhedra.[6] Furthermore, a highly polarisable anion framework can lower the migration barriers.[7]

2.2 Impedance Spectroscopy

2.2.1 Theory

Electrochemical impedance spectroscopy is an important and widely used measurement method for the characterization of ion conducting materials. During a measurement, an alternating current (AC) is applied to the sample in a wide frequency range (typically 1 mHz to 1 MHz) and the resulting electric resistance or impedance is measured.

Electronic conductors, e.g. metals, are called ohmic materials if the current through this material is directly proportional to the applied voltage. According to Ohm's law, the resistance R can be determined from the applied voltage U and current I (equation 2.1).

$$R = \frac{U}{I} \tag{2.1}$$

However, most real systems do not exhibit purely ohmic behavior when an AC voltage is applied. This results in a phase shift of current and voltage.

A simple example for a frequency dependent system is a capacitor. At low frequencies, the impedance is high and only a low current can be measured. With increasing frequencies, the impedance is decreasing. The phase difference between current and voltage is 90° for an ideal capacitor.

The hopping of ions, which occurs in ionic conductors, is also a frequency dependent phenomenon.

The electric resistance in an AC system, the impedance Z, can be determined from voltage *U(t)* and current *I(t)* (equation 2.2). Thereby, the phase shift between current (ϕ_I) and voltage (ϕ_U) must be considered.

$$Z = \frac{U(t)}{I(t)} = \frac{U_0 \cdot sin(\omega t + \phi_U)}{I_0 \cdot sin(\omega t + \phi_I)} \tag{2.2}$$

The voltage *U(t)* and current *I(t)* are defined by their amplitude U_0 and I_0 and their phaseshift ϕ and the angular frequency ω.

For the following description voltage and current are expressed as the complex quantities $\hat{U}$ and $\hat{I}$.

$$\hat{U} = U_0 \cdot e^{j(\omega t + \phi_U)} \tag{2.3}$$

$$\hat{I} = I_0 \cdot e^{j(\omega t + \phi_I)} \tag{2.4}$$

This results in

$$\hat{Z} = \frac{\hat{U}(t)}{\hat{I}(t)} = \frac{U_0}{I_0} \cdot e^{j(\phi_U - \phi_I)} = Z \cdot e^{j\phi} \tag{2.5}$$

The impedance $\hat{Z}$ comprises the Ohmic resistance as real part (Z_{Re}) and the complex resistance with frequency dependent behavior as the imaginary part (Z_{Im}). By applying Euler's formula, Z_{Re} and Z_{Im} can be defined as follows

$$Z \cdot e^{j\phi} = Z\cos\phi + Zj\sin\phi \tag{2.6}$$

$$|Z| = \sqrt{(Z_{Re})^2 + (Z_{Im})^2} \tag{2.7}$$

$$\phi = \arctan\left(\frac{-Z_{Im}}{Z_{Re}}\right) \tag{2.8}$$

$$Z_{Re} = |Z|\cos\phi \tag{2.9}$$

$$Z_{Im} = |Z|\sin\phi \tag{2.10}$$

Measurement results from impedance spectroscopy are commonly plotted in two different diagrams. In the Nyquist plot the real part of the impedance (Z_{Re}) is plotted against the imaginary part of the impedance (Z_{Im}). The course of the graph in the Nyquist plot depends on the underlying conductivity phenomenon. For semiconductors a semicircle is visible in the Nyquist diagram. The typcial course for an ion conductor is a semicircle at high frequencies followed by a linear spike at lower frequencies.
The second plotting option is the Bode plot where the phase shift between voltage and current and the impedance are plotted against the frequency.
Resistances, capacities and conductivities can be determined from these diagrams. Therefore it is desirable to describe the complex real system by an equivalent circuit which consists of several electronic components. This circuit can include, among others, resistors (R), Warburg elements (W), capacitors and constant phase elements (CPE). There is not a unique model ciruit for a given impedance spectrum so it is important that each component correlates to an underlying physical process. In Figure 2.1 a R-C equivalent circuit and the corresponding Nyquist plot, a semi circle, is shown.

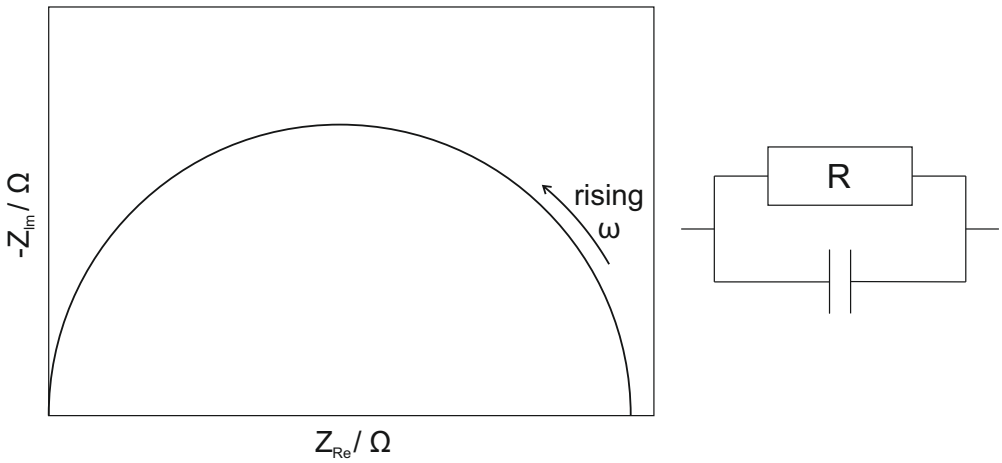

Figure 2.1 Schematic representation of Nyquist plot for a R-C equivalent circuit.

To describe grain boundary resistance in real systems, a second R-C circuit can be added in serial (Figure 2.2). This results in a second semi circle in the Nyquist plot.
To fit impedance spectra of ion conductors, a R-C circuit combined with a Warburg element is used (Figure 2.3). The Warburg element is defined as a CPE with a constant phase angle of 45° and represents the mass transfer towards the ion-blocking electrodes.
The specific resistances, which are determined from the Nyquist diagrams, are related to the specific conductivity.

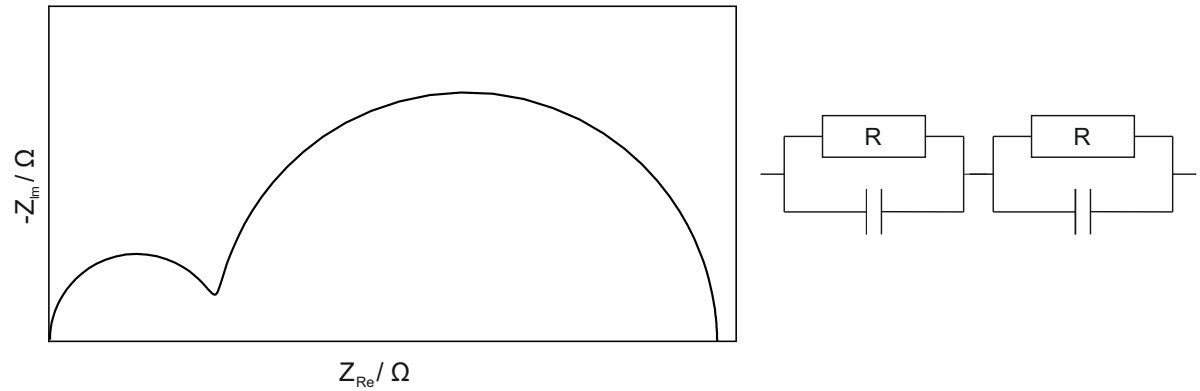

Figure 2.2 Schematic representation of Nyquist plot for a (R-C)-(R-C) equivalent circuit.

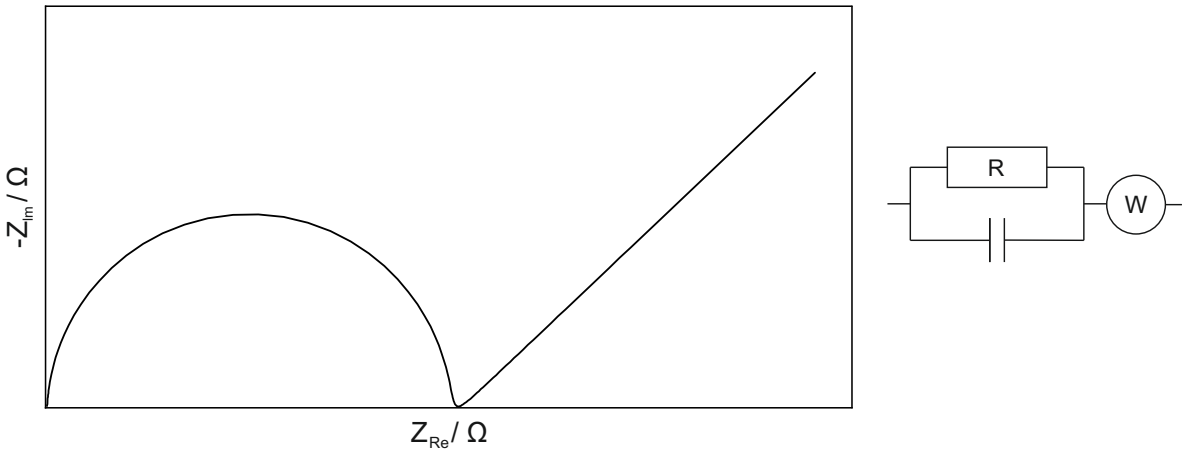

Figure 2.3 Schematic representation of Nyquist plot a (R-C)-W equivalent circuit.

$$R = R_{spec}\frac{l}{A} = \frac{1}{\sigma_{spec}}\frac{l}{A} \tag{2.11}$$

$\frac{l}{A}$ describes the cylindrical geometry of the sample with length l and base area A. The so determined specific conductivity has to be corrected by including the pellet density factor ρ which has to be determined from the density of sample pellet ρ_p and the calculated density. To reduce grain boundary effects during the measurements, pellet densities should be as high as possible (larger than 90 %).

$$\rho_p = \frac{m_p}{V_p} \tag{2.12}$$

$$\rho_x = \frac{Z \cdot M}{V \cdot N_A} \tag{2.13}$$

$$\rho = \frac{\rho_p}{\rho_x} \tag{2.14}$$

In most cases, the specific conductivities exhibit an Arrhenius-like behavior.

$$\sigma_{spec} = \sigma_0 \cdot e^{-\frac{E_A}{k_B T}} \tag{2.15}$$

Taking the logarithm of the Arrhenius equation yields

$$\ln \sigma_{spec} = \ln \sigma_0 + \left(-\frac{E_A}{k_B}\right) \cdot \frac{1}{T} \tag{2.16}$$

or

$$\log \sigma_{spec} = \log \sigma_0 + \left(-\frac{E_A}{\ln 10 k_B}\right) \cdot \frac{1}{T} \tag{2.17}$$

A plot of $\log \sigma_{spec}$ versus T^{-1} results in a linear relationship. The activation energy E_A can be determined from the slope of this straight line.

2.2.2 Measurement Setup

Impedance measurements were performed in a glovebox under Ar atmosphere. Powder samples were finely ground and then pressed to pellets using a mechanical press. Depending on the respective sample a pressure of 4 t to 5 t for up to 5 min was applied. The pellet was then mounted in the measurement cell which is installed in a tube furnace inside a glovebox. The measurement cell was constructed and built according to the design of *Freudenthaler*.[8] A schematic representation of the measurement setup is shown in Figure 2.4. The sample pellet is enclosed with Au plates which are contacted with Pt plates. To insulate the cell, corundum plates are attached outside of the platinum sheets. Metal springs are used to compress the cell and to ensure good contact between the sample and the electrodes. The measurement cell is connected to a *Zahner Zennium* Impedance Analyzer via Pt wires and Cu connectors. The *ThalesFlink* software was used to control the measurements.[9] A detailed description of the measurement setup is given by *Huber*.[10]

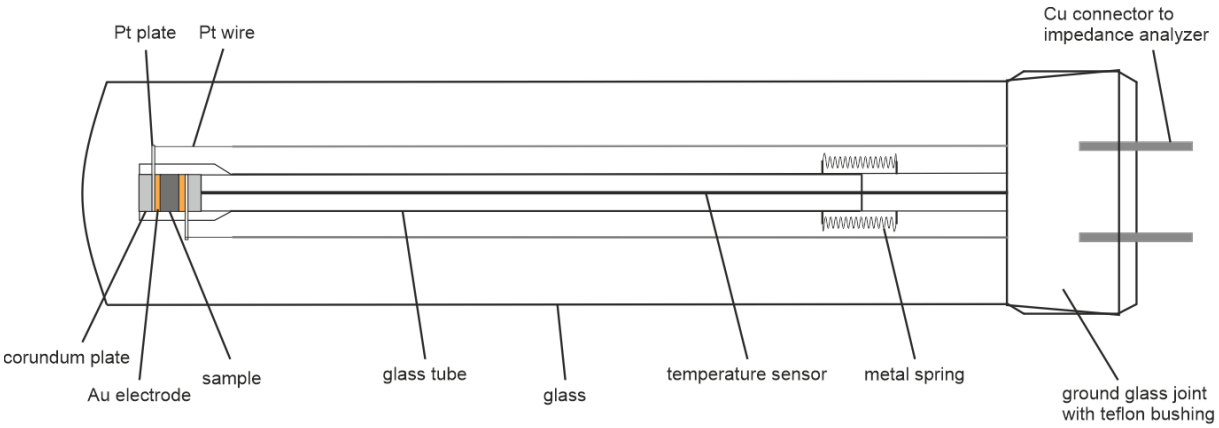

Figure 2.4 Schematic representation of the measurement setup for impedance spectroscopy.

2.3 Density Functional Theory

2.3.1 Quantum mechanical background

Common practice for the quantum mechanical description of crystalline materials is the application of density functional theory (DFT). It allows the investigation of many-body systems like molecules and condensed phases with relatively low computational costs compared to other methods like Hartree-Fock theory.
DFT is based on the theorems of *Hohenberg* and *Kohn*.[11] The first theorem demonstrates that the ground-state properties of a system can be determined from the ground-state electron density $\rho_0(r)$. Therefore, the many-body problem of N electrons with $3N$ spatial coordinates can be reduced to only 3 spatial coordinates. The wavefunction can be described as functional of the density:

$$\Psi = \Psi[\rho(r)] \tag{2.18}$$

The second theorem describes that the ground-state energy $E[\rho(r)]$ of a system is minimized at the ground-state density $\rho_0(r)$ (Hohenberg-Kohn density variational principle).

$$\langle \Psi^* | H | \Psi \rangle = E \geq E_0 \tag{2.19}$$

Kohn and *Sham* developed a formalism to determine all properties of a system from the electron density.[12] For a system of non-interacting particles, the hamiltonian can be expressed as sum of one-particle-operators.

$$\left[-\frac{\hbar^2}{2m}\nabla^2 + V(r) + V_H(r) + V_{xc}(r)\right]\Psi_i(r) = \epsilon_i\Psi_i(r) \tag{2.20}$$

where $V(r)$ is the external potential, $V_H(r)$ is the Hartree potential which describes electron-electron Coulomb repulsion and $V_{xc}(r)$ is the exchange-correlation potential which is defined as the derivation of the exchange-correlation energy $E_{xc}(r)$. The exchange-correlation term corrects the difference in energy for the fictitious non-interacting system and the real interacting system. There are different approaches for the approximation of this energy. The simplest one is the *local density approximation* (LDA) where the exchange-correlation potential is replaced for the electron density $\rho(r)$.[13–15] Since LDA tends to overestimate binding,[16] the gradient of the local density was added resulting in *generalized gradient methods* (GGA). In this work, for the GGA calculations mostly the PBE functional derived by *Perdew*, *Burke* and *Ernzerhof* was used.[17] To improve accuracy, especially for electronic structure calculations, hybrid functionals were developed. In hybrid functionals GGA exchange is mixed with nonlocal exact exchange. The mainly used hybrid functional in this work is HSE06 which was utilized for electronic structure calculations.[18]

2.3.2 Gaussian Basis Sets

The electronic structures of periodic systems in CRYSTAL[19,20] are calculated using Bloch functions. The crystal orbitals are expressed as linear combinations of atom-centered Gaussian-type functions that are centered at each nucleus.[21] In contrast to plane-wave based basis sets Gaussian-type basis functions cannot be used universally for all types of compounds. Instead, various basis sets are available for most elements in the periodic table which can be found in libraries such as the CRYSTAL Basis Sets library.[22] The accuracy and the computational cost of quantum-chemical calculations strongly depend on the chosen basis set. Hence, it is necessary to check if the basis set is suitable for the given system. As a first step, different basis sets were tested. Therefore, lattice constants and atomic positions were optimized and compared with the experimentally determined values. The chosen basis sets were then optimized for the respective systems by modifying the orbital exponents of the outer shells. The optimization procedure was performed within a python-script where the exponents were adjusted gradually to minimize the total energy of the system. The exponents were restricted to be equal or larger than 0.1 to avoid stability issues during the calculations.

2.3.3 Geometry Optimization

The first step of most quantum-chemical calculations are geometry optimizations starting from experimentally determined structure data. Therefore, the interatomic forces F between two atoms with distance R are calculated *ab initio* by applying the *Hellmann-Feynman* theorem.[23,24]

$$F = -\frac{dE}{dR} = -\left\langle \Psi \middle| \frac{\partial H}{\partial R} \middle| \Psi \right\rangle \tag{2.21}$$

The atoms are then subsequently moved in the direction of the calculated forces. After each step, the electronic structure and the forces are calculated again until the determined forces are below a given threshold. By minimizing the total energy with respect to the atomic positions a energy minimum is reached were the forces acting on atoms are close to zero. A Quasi-Newton scheme is implemented for automatic geometry optimizations in CRYSTAL.[19,20,25]

2.3.4 Equation of State Calculation

Also the calculation of physical properties like phase transition pressure is possible by using DFT. To examine energetic differences of various modifications of a crystalline materials energy vs. volume curves (E-V-curves) are calculated. Thereby, the several geometry optimizations at different fixed volumes are performed. The resulting E and V values can be fitted with the Birch-Murnaghan equation of state[26–28] (EOS):

$$E(V) = E_0 + \frac{9V_0B_0}{16}\left\{\left[\left(\frac{V_0}{V}\right)^{\frac{2}{3}} - 1\right]^3 B_0' + \left[\left(\frac{V_0}{V}\right)^{\frac{2}{3}} - 1\right]^2 \left[6 - 4\left(\frac{V_0}{V}\right)^{\frac{2}{3}}\right]\right\} \tag{2.22}$$

where B_0 is the equilibrium bulk modulus of a crystal. This quantity is a measure of the resistance of a material to bulk compression.

$$B_0 = V\frac{\partial p}{\partial V} \tag{2.23}$$

$$B_0' = \frac{\partial B_0}{\partial p} \tag{2.24}$$

After fitting and determination of B_0, the transition pressure can be calculated:

$$P(V) = -\left(\frac{\partial E}{\partial V}\right)_S = \frac{3B_0}{2}\left[\left(\frac{V_0}{V}\right)^{\frac{7}{3}} - \left(\frac{V_0}{V}\right)^{\frac{5}{3}}\right]\left[1 + \frac{3}{4}(B_0' - 4)\left[\left(\frac{V_0}{V}\right)^{\frac{2}{3}} - 1\right]\right] \quad (2.25)$$

2.3.5 Electronic Structure

The electronic structure of crystalline materials can be displayed as electronic band structure which plots energy vs. wavevector (k). Because of the high number of atoms in solid state materials instead of discrete energy values there are bands. Band structures are usually plotted along a k path within the first Brillouin zone which is a primitive cell in the reciprocal space. Band paths for different Bravais lattice types can be determined with the SeeK-path online tool.[29]

For more complex systems often the density of states (DOS) is considered. It is a summation of infinitesimal small energy ranges and, in other words, corresponds to the projection of the bands onto E.

The electronic conductivity of crystalline materials depends, among others, on the size of the band gap which is clearly visible in the DOS. Analyzing the DOS around the Fermi niveau, which is defined as the energy of the highest occupied state, can give indications about the conductivity of a material. Insulators show a large band gap above the Fermi level whereas for metallic systems no gap is observed. For an exact determination of band gap sizes, calculation of exited states would be necessary. Especially for systems with small band gaps the calculated values often differ from experimentally determined values significantly. Usage of the HSE hybrid functional reduces errors compared to LDA or GGA functionals.[30]

References

[1] Brune, A.; Wagner, J. *Mater. Res. Bull.* **1995**, *30*, 573–579.

[2] Frenkel, J. *Z. Phys.* **1926**, *35*, 652–669.

[3] Schottky, W. *Z. Phys. Chem. B* **1935**, *29*, 335–355.

[4] West, A. R., *Solid state chemistry and its applications*, 2nd ed.; John Wiley & Sons, Ltd.: 2014.

[5] Funke, K. *Prog. Solid State Chem.* **1993**, *22*, 111–195.

[6] Wang, Y.; Richards, W. D.; Ong, S. P.; Miara, L. J.; Kim, J. C.; Mo, Y.; Ceder, G. *Nat. Mater.* **2015**, *14*, 1026–1031.

[7] Kraft, M. A.; Culver, S. P.; Calderon, M.; Böcher, F.; Krauskopf, T.; Senyshyn, A.; Dietrich, C.; Zevalkink, A.; Janek, J.; Zeier, W. G. *J. Am. Chem. Soc.* **2017**, *139*, 10909–10918.

[8] Freudenthaler, E. Kupfer(I)-halogenid-Addukte mit polymeren Phosphor- bzw. Phosphorchalcogenid-Teilstrukturen: Darstellung, Strukturen und elektrische Eigenschaften, Ph.D. Thesis, Universität Siegen, 1997.

[9] Zahner-Elektrik Thales Flink; I. Zahner-Schiller GmbH & Co. KG, Kronach, 2014.

[10] Huber, S. Lithiumionenleiter - Strukturelle und impedanzspektroskopische Untersuchungen an neuartigen Lithiumfeststoffelektrolyten, Ph.D. Thesis, Universität Regensburg, 2015.

[11] Hohenberg, P.; Kohn, W. *Phys. Rev.* **1964**, *136*, 864–871.

[12] Kohn, W.; Sham, L. J. *Phys. Rev.* **1965**, *140*, A1133–A1138.

[13] Perdew, J. P.; Zunger, A. *Phys. Rev. B* **1981**, *23*, 5048–5079.

[14] Vosko, S. H.; Wilk, L.; Nusair, M. *Can. J. Phys.* **1980**, *58*, 1200–1211.

[15] Perdew, J. P.; Wang, Y. *Phys. Rev. B* **1992**, *45*, 13244–13249.

[16] Becke, A. D. *Phys. Rev. A* **1986**, *33*, 2786–2788.

[17] Perdew, J. P.; Burke, K.; Ernzerhof, M. *Phys. Rev. Lett.* **1996**, *77*, 3865–3868.

[18] Heyd, J.; Scuseria, G. E.; Ernzerhof, M. *J. Chem. Phys.* **2003**, *118*, 8207–8215.

[19] Dovesi, R.; Erba, A.; Orlando, R.; Zicovich-Wilson, C. M.; Civalleri, B.; Maschio, L.; Rérat, M.; Casassa, S.; Baima, J.; Salustro, S.; Kirtman, B. *WIREs Comput. Mol. Sci.* **2018**, *8*, e1360.

[20] Dovesi, R. et al. CRYSTAL23 User's Manual; University of Torino, 2023.

[21] Dovesi, R.; Orlando, R.; Erba, A.; Zicovich-Wilson, C. M.; Civalleri, B.; Casassa, S.; Maschio, L.; Ferrabone, M.; Pierre, M. D. L.; D'Arco, P.; Noël, Y.; Causà, M.; Rérat, M.; Kirtman, B. *Int. J. Quantum Chem.* **2014**, *114*, 1287–1317.

[22] Basis Set Library, `https://www.crystal.unito.it/basis_sets.html`, accessed: 16.04.3024.

[23] Hellmann, H., *Einführung in die Quantenchemie*; Franz Deuticke: 1937.

[24] Feynman, R. P. *Phys. Rev.* **1939**, *56*, 340–343.

[25] Shanno, D. F. *Math. Comp.* **1970**, *24*, 647–656.

[26] Murnaghan, F. D. *Amer. J. Math.* **1937**, *59*, 235–260.

[27] Murnaghan, F. D. *Proc. Natl. Acad. Sci.* **1944**, *30*, 244–247.

[28] Birch, F. *Phys. Rev.* **1947**, *71*, 809–824.

[29] Hinuma, Y.; Pizzi, G.; Kumagai, Y.; Oba, F.; Tanaka, I. *Comput. Mater. Sci.* **2017**, *128*, 140–184.

[30] Heyd, J.; Peralta, J. E.; Scuseria, G. E.; Martin, R. L. *J. Chem. Phys.* **2005**, *123*, 174101.

3 Sodium Selenotetrelates with Isolated $TtSe_4$-Tetrahedra (Tt = Si, Ge, Sn): Synthesis, Crystal Structures, Thermal Behavior, DFT Modeling and Na Ion Conductivities

3.1 Preface and Abstract

This chapter is reprinted and adapted from *Chemistry of Materials* **2024**, *36*, 5643-5650. Several people contributed to this work:

- Franziska Kamm performed the experimental work and the DFT calculations and wrote and improved the manuscript.
- Dr. Florian Pielnhofer supervised the DFT calculations, contributed with discussions and improved the manuscript.
- Prof. Dr. Arno Pfitzner supervised the experimental work, contributed with discussions and improved and corrected the manuscript.

Abstract

Selenotetrelate compounds Na_4TtSe_4 (Tt = Si, Ge, Sn) were synthesized by solid state reactions. A new modification of Na_4SiSe_4 (Na_4SiSe_4-$cP72$), which crystallizes in the cubic space group $P\bar{4}3n$ (no. 218) with a = 12.130(1) Å and V = 1784.453(5) Å^3, and a new modification of Na_4SnSe_4 (Na_4SnSe_4-$tI216$), which crystallizes in the tetragonal space group $I4_1/acd$ (no. 142) with a = 14.4053(4) Å, c = 28.5751(8) Å and V = 5929.7(3) Å^3, were discovered. All title compounds exhibit moderate to good sodium ion conductivities, as revealed by electrochemical impedance spectroscopy. The formation reaction of Na_4SiSe_4 was further investigated by high temperature X-ray powder diffraction of the ball milled reaction mixture. Density functional based quantum chemical calculations were performed

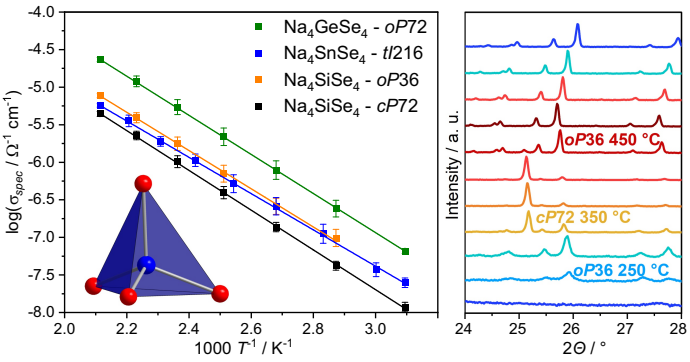

to compare the different modifications of Na_4SiSe_4 and Na_4SnSe_4 energetically. Further modifications of Na_4SiSe_4 and Na_4GeSe_4 seem plausible as revealed by density functional theory modeling. The stability of the hypothetic modifications was examined by phonon dispersion calculations.

3.2 Introduction

All-solid-state-batteries (ASSBs) became promising options for battery systems.[1,2] One of the key components in ASSBs is the solid electrolyte, which must exhibit high ionic conductivities. After concentrating on lithium based systems for a long time, research focused on solid sodium ion conductors recently.[3–5] In particular for stationary applications sodium based batteries are a valuable alternative to lithium based systems. Due to the higher abundance of sodium the costs for battery systems can be significantly lowered.
Some of the highest sodium ion conductivities were found in sulfides such as the thiophosphate Na_3PS_4.[6,7] By substitution of S with Se, the ionic conductivity could be further increased.[8–10] Furthermore, the charge carrier density and therefore also the ionic conductivity can be increased by the incorporation of tetrels, for example in $Na_{10}SnP_2S_{12}$.[11–13] Despite that, ternary sodium selenotetrelates are less investigated regarding their sodium ion conductivity.
A variety of structure types including different anions exist among ternary alkali metal, tetrel (Tt = Si, Ge, Sn) and chalcogenide (Q = S, Se, Te) containing materials. Most of them consist of TtQ_4 tetrahedra which are connected in different ways. This includes isolated TtQ_4 tetrahedra,[14–20] dimers Tt_2Q_7 from corner-sharing tetrahedra,[21] infinite chains Tt_2Q_6 of tetrahedra sharing two corners[22] or layers of corner-sharing $GeSe_4$-tetrahedra.[23] In the perselenodisilicate $Na_6Si_2Se_8$, two $SiSe_4$ tetrahedra are connected by a Se-Se bond to form $Si_2Se_8^{6-}$ units.[24] Adamantan-analogous units are found in $Na_4Si_4Se_{10}$[22] and $Na_4Ge_4Se_{10}$.[25] Even Tt-Tt bonds are present in hypoditetrelates to form ethane molecule analogous anions.[26–28] Edge-sharing $SiSe_4$ tetrahedra dimers are exclusively observed in $Na_4Si_2Se_6$-$tP24$.[29] Especially the physical and chemical characterization of sodium selenotetrelates is very scarce in literature. To date, the focus has been mostly set on crystal growth and determination of crystal structures. Minor interest arose for the phase pure synthesis and investigation of physical properties, e.g. ion conductivity, when these compounds were first discovered. In contrast to the selenides, the sulfides Na_4SiS_4,[30] Na_4GeS_4[31] and Na_4SnS_4[32,33] were characterized regarding their chemical and physical properties. All sodium thiotetrelates show sodium ion con-

Table 3.1 Compounds and structure types of alkali selenotetrelates.

structure type	examples	space group
Li_4GeS_4[34]	Li_4GeSe_4-$oP36$,[15] Li_4SnSe_4-$oP36$[14a]	$Pnma$ (no. 62)
Na_4GeSe_4[16]	Na_4GeSe_4-$oP72$	$Pnma$ (no. 62)
Na_4SnS_4[35]	Na_4SnSe_4-$tP18$[17]	$P\bar{4}2_1c$ (no. 114)
K_4SnSe_4[17]	Na_4SiSe_4-$oP36$,[18] K_4SnSe_4-$oP36$	$Pnma$ (no. 62)
Ba_4SiAs_4[19]	K_4GeSe_4-$cP72$,[36] Cs_4SiSe_4-$cP72$[20]	$P\bar{4}3n$ (no. 218)

[a]Both compounds have the same building principle and the same space group, but show minor differences in the Li substructure

ductivity. It can therefore be assumed that also sodium selenotetrelates show sodium ion conductivity and should be examined systematically. Two selenide compounds were already checked for sodium ion mobility. Impedance spectroscopy measurements reveal moderate to good ionic conductivities for $Na_4Si_2Se_6$-$oP48$[29] ($1.4 \times 10^{-8}\,S\,cm^{-1}$ at 50 °C) and Na_4SnSe_4-$tP18$[32] ($1.13 \times 10^{-8}\,S\,cm^{-1}$ at 20 °C).

Herein we focus on sodium selenotetrelates with isolated $TtSe_4$ tetrahedra (Tt = Si, Ge and Sn). Many alkali metal compounds containing this structural motif are already known (Table 3.1). Most of the selenotetrelates described in the literature were synthesized by classical high temperature solid state routes. Other methods, such as the use of ball mills, open the possibility to synthesize new compounds in the already well established system. Besides the determination of sodium ion conductivity in already known sodium selenotetrelates Na_4TtSe_4, new modifications of Na_4SiSe_4 and Na_4SnSe_4 were discovered. The two-step synthesis procedure consisting of ball milling followed by annealing was examined for Na_4SiSe_4. Starting from the ball-milled reaction mixture, the formation of the two modifications of Na_4SiSe_4 can be followed with in-situ high-temperature X-ray powder diffraction. The stability of the new modifications was further studied by density functional theory (DFT) modeling including yet unknown hypothetical modifications. Ionic conductivities were determined for all of the title compounds.

3.3 Experimental Section

3.3.1 Synthesis

All preparations and sample treatments were performed under an Ar atmosphere.
The title compounds were synthesized from the elements. Sodium (Sigma-Aldrich, 99.8 %), silicon (siltronic, silicon wafer), tin (ChemPur, 99+%) and selenium (ChemPur, 99.99 %) were used as received. Germanium (ChemPur, 99.99 %) was purified in H_2-atmosphere at 600 °C and stored in Ar atmosphere. Syntheses were performed in an FRITSCH pulverisette 7 premium line ball mill with 25 mL zirconia grinding bowls and 10 zirconia grinding balls with a diameter of 10 mm. In each case, 0.3 g of the ball milled mixture was transferred to silica ampules which were subsequently evacuated, flame sealed and transferred to tube furnaces. In case the reaction temperature was higher than 600 °C, silica ampules with a graphite coating from pyrolized acetone were used to prevent reactions with the glass.
Na_4SiSe_4-*oP*36 and Na_4SiSe_4-*cP*72 were synthesized by ball milling Na, Si and Se with a molar ratio of 4 : 1 : 4 in 12 milling cycles at a top speed of 600 rpm for 3 min each. For Na_4SiSe_4-*cP*72, the mixture was then heated to 375 °C with a heating rate of 1 °C min^{-1}. After 10 days, the ampule was quenched in air. Small amounts of Na_2Se_2 (3.8 % according to Rietveld refinements) were detected as side phase. To synthesize Na_4SiSe_4-*oP*36 the mixture was heated to 500 °C for 3 days. Both heating and cooling rates were set to 1 °C min^{-1}.
Na_4GeSe_4-*oP*72 was synthesized by ball milling Na, Ge and Se with a molar ratio of 4 : 1 : 4. Twelve milling cycles at a top speed of 600 rpm were performed. The mixture was then heated to 400 °C for 7 days. Both heating and cooling rates were set to 1 °C min^{-1}.
Na_4SnSe_4-*tI*216 was synthesized by ball milling Na, Sn and Se with a molar ratio of 4.1 : 1 : 4. Three milling cycles with a top speed of 300 rpm followed by 25 milling cycles at 400 rpm were performed. The mixture was then heated to 800 °C with a heating rate of 0.5 °C min^{-1} and kept at this temperature for 1 h. After cooling down slowly within 1 day, orange crystals were observed.

3.3.2 X-ray Powder Diffraction

Finely ground samples were filled in quartz capillaries ($\varnothing$ = 0.3 mm) that were subsequently flame sealed. The capillaries were mounted on a STOE STADI P diffractometer (Stoe & Cie) equipped with a Mythen 1 K detector and measured using Cu$K\alpha_1$ radi-

ation (λ = 1.5406 Å). The high temperature diffraction experiment was performed in a graphite furnace which was mounted on the diffractometer. For raw data handling the *WinXPow*[37] software package (Stoe & Cie) was used. Le Bail refinements, structure solution and Rietveld refinements were done with *Jana2006*[38] and the implemented *Superflip*[39] algorithm.

3.3.3 Single Crystal X-ray Diffraction

The single crystal diffraction experiment was performed at 296 K on a Rigaku SuperNova diffractometer with an AtlasS2 detector using MoKα radiation (λ = 0.710 73 Å). For cell determination, data reduction and absorption correction the *CrysAlis Pro* software[40] was used. The structure was solved using the *Superflip*[39] algorithm which is implemented in *Jana2006*.[38] Structure refinement was also performed with *Jana2006*.

3.3.4 Differential Thermal Analysis

For differential thermal analysis (DTA) measurements, a SETARAM TG-DTA 92.16.18 was used. Samples were transferred into quartz tubes ($\varnothing$ = 2 mm) which were evacuated and flame sealed. Thermal properties were investigated up to 800 °C.

3.3.5 Impedance Spectroscopy

Electrochemical impedance spectroscopy (EIS) was performed with a *Zahner Zennium* impedance analyzer coupled to a homemade furnace. The complete setup was installed in a glovebox under an Ar atmosphere to prevent reactions of the samples with air or moisture during the measurements. Because of this setup, no measurements below 50 °C were possible. Powder samples were cold-pressed and contacted with gold electrodes. Pellets had a density of 96 % (Na_4SiSe_4-*oP*36), 86 % (Na_4SiSe_4-*cP*72), 96 % (Na_4GeSe_4) and 90 % (Na_4SnSe_4-*tI*216). In each case, two temperature cycles in the frequency range from 1 MHz to 100 mHz were recorded. For the different compounds different temperature ranges and temperature steps were used. Na_4SiSe_4-*oP*36, Na_4SiSe_4-*cP*72 and Na_4GeSe_4 were analyzed in the temperature range from 50 °C to 200 °C in steps of 25° and Na_4SnSe_4-*tI*216 from 50 °C to 200 °C in steps of 20 °C. The excitation voltage was set to 50 mV in each case. Ionic conductivities were determined from the second heating and cooling cycles, since the contact between pellets and electrodes is much better. For data processing and fitting the *Zahner Analysis* software[41] was used. Nyquist plots were fitted by different equivalent

circuits (see Figure A.14). The so determined resistance R was corrected by including the density of the pellet to calculate the specific conductivity σ_{spec}. Activation energies E_A were determined from the slopes in the Arrhenius plots. For Na_4SiSe_4-$oP36$, the evaluation of the ionic conductivity at 50 °C was not possible due to the bad quality of the measured data. After the measurements, all samples were checked for decomposition or phase transitions by X-ray powder diffraction. Apart from the expected peak broadening, all samples were identical to the starting material, which is especially important for the cubic modification.

3.3.6 DFT Modeling

All quantum chemical calculations were performed using the CRYSTAL17 code.[42,43] Basis sets (Na,[44] Si,[45] Ge,[46] Sn[47] and Se[48]) were taken from the literature. The outer shells of all basis sets were additionally adjusted to minimize the calculated energy. Full structure optimizations within the given space groups were performed with the hybrid HSE06[49,50] using a k mesh sampling of $6 \times 6 \times 6$. The convergence criterion for the energy was set to 10×10^{-8} a u . Geometries were optimized using experimentally determined structure data as starting point. For calculation of electronic energy E vs. volume per formula unit V curves constant volume optimizations were performed using the GGA functional PBE.[51] Data was fitted with the Birch-Murnaghan equation of state.[52–54] For electronic band structure calculations the hybrid HSE06 was used. k paths were determined using the SeeK-path online tool.[55] Phonon frequencies including LO-TO splitting were calculated as implemented in CRYSTAL17.[56,57] Because of the high computational effort, calculations were performed on the PBE level with a $2 \times 2 \times 2$ super cell and a k mesh sampling of $4 \times 4 \times 4$. To increase accuracy for phonon frequency calculation, the SCF convergence criterion was set to 10×10^{-10} a u .

3.4 Results and Discussion

3.4.1 Crystal Structure of Na_4SiSe_4-*cP*72

The new modification Na_4SiSe_4-*cP*72 crystallizes in the cubic space group $P\bar{4}3n$ (no. 218) with $a = 12.1295(1)$ Å and $V = 1784.543(5)$ Å^3; Z = 8. The crystal structure was determined by powder X-ray diffraction via *Superflip* and the Rietveld method (Figure 3.1). Further crystallographic data and structure determination details can be found in Table 3.2 and in Tables A.1 and A.2.

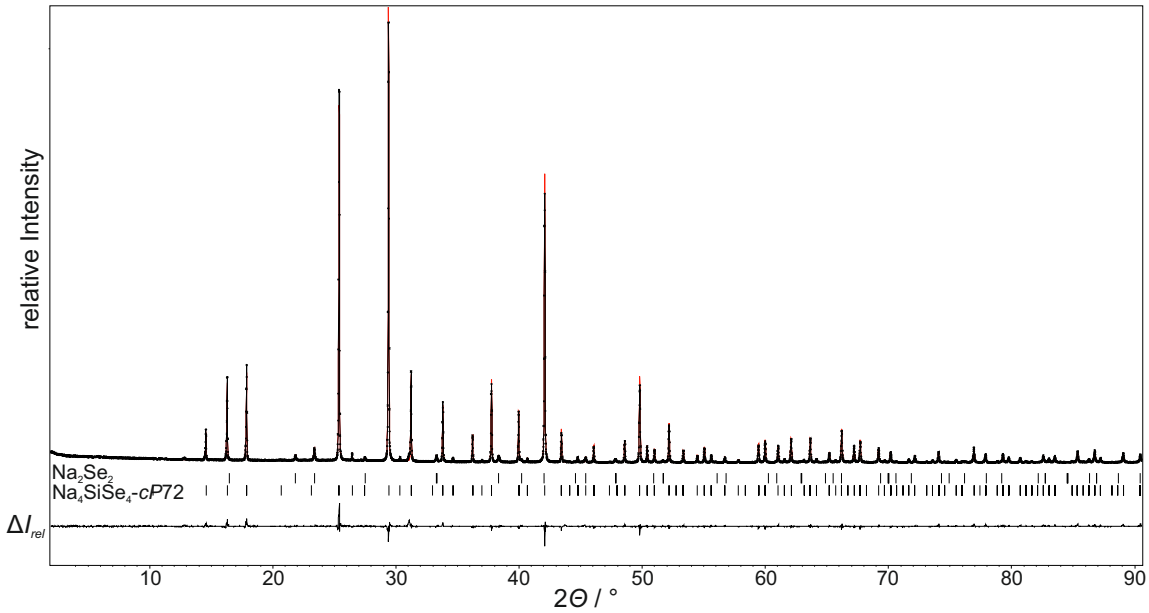

Figure 3.1 X-ray powder diffraction pattern of Na_4SiSe_4-*cP*72 with difference plot from Rietveld refinement. The side phase was determined to be Na_2Se_2[58] (3.8 %).

The main structural features are the isolated $SiSe_4$ tetrahedra, which are also found in the second modification Na_4SiSe_4-*oP*36.[18] The unit cell with all isolated $SiSe_4$ tetrahedra is shown in Figure 3.2. Na_4SiSe_4-*cP*72 adopts the Ba_4SiAs_4 structure type[19] which is described in detail by *Eisenmann* et *al.* The crystal structure can be derived from the NaCl structure type with Se^{2-} forming a distorted face-centered cubic lattice where Na^+ occupies all octahedral voids. Additionally, Si^{4+} occupies $\frac{1}{8}$ of all tetrahedral voids in an ordered manner.

There are two crystallographically different $SiSe_4$ tetrahedra with distances d(Si-Se) of 2.248(2) Å for Si1 and 2.2543(9) Å for Si2. Angles deviate only slightly from ideal tetrahe-

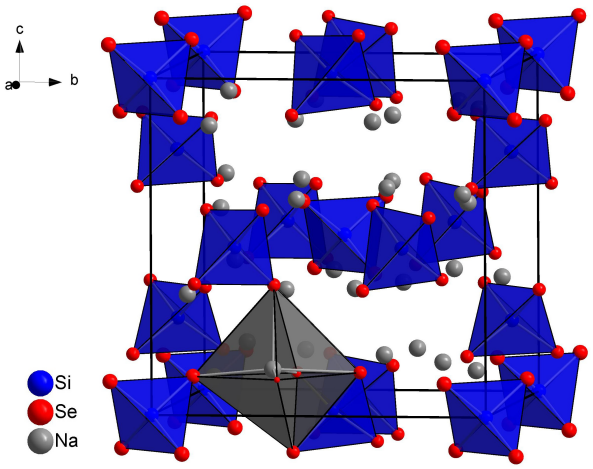

Figure 3.2 Unit cell of Na_4SiSe_4-$cP72$ with Na and Si coordination polyhedra.

dra angles (109.47(6)° for Si1; 107.27(4)° and 113.97(3)° for Si2). Na1 and Na2 are both coordinated octahedrally with distances d(Na-Se) varying from 2.933(4) Å to 3.245(4) Å. All interatomic distances are in the expected range. A comparison of distances and angles in both modifications of Na_4SiSe_4 is given in Table S3. Crystal structures of both modifications can be derived from space group $Fm\bar{3}m$ (no. 225) but there is no direct group-subgroup relation.

3.4.2 Crystal Structure of Na_4SnSe_4-*tI*216

The new modification Na_4SnSe_4-*tI*216 crystallizes in the tetragonal space group $I4_1/acd$ (no. 142) with lattice parameters $a = 14.4098(4)$ Å, $c = 28.5851(8)$ Å and $V = 5935.5(3)$ Å^3 with Z=24. Further crystallographic data and structure determination details can be found in Table 3.2 and Tables A.6 and A.7.

The structure type is already known from Na_4SnTe_4-*tI*216.[59] As a detailed structure discussion for Na_4SnS_4, which crystallizes in the same structure type, is already given by *Hartmann* et *al.*,[33] only the primary features will be mentioned in the following. The main structural motifs are isolated $SnSe_4$ tetrahedra (Figure 3.3). There are two distinct Sn positions with a tetrahedral coordination with distances d(Sn-Se) from 2.5106(2) Å to 2.5286(2) Å. Na1, Na2 and Na3 are coordinated octahedrally with distances d(Na-Se) varying from 2.8319(2) Å to 3.3821(8) Å. Na4 is surrounded tetrahedrally with distances d(Na4-Se) of 2.9449(7) Å and 2.990(1) Å. Na5 has a distorted trigonal bipyramidal coordination with distances d(Na5-Se) varying from 2.9625(9) Å to 3.358(1) Å. A further Se at a distance d(Na5-Se) of 3.9255(9) Å completes the coordination environment to a strongly distorted octahedron. Na-Se polyhedra form a 3D network with nearly linear and zigzag chains in the *c*-direction and in the *ab*-plane. All interatomic distances are in the expected range. A comparison of distances and angles in both modifications of Na_4SnSe_4 is given in Table S8.

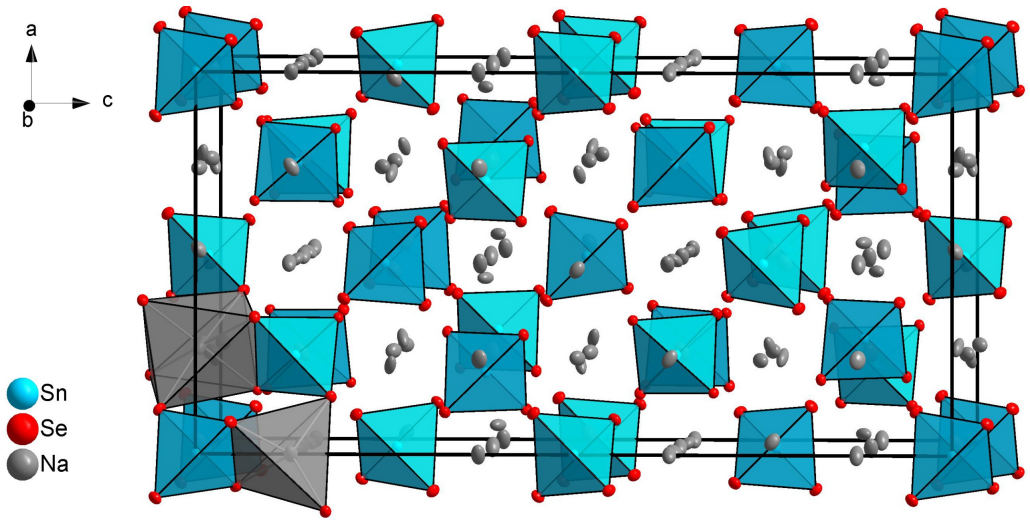

Figure 3.3 Unit cell of Na_4SnSe_4-*tI*216 with isolated $SnSe_4$ tetrahedra and Na coordination polyhedra.

Table 3.2 Crystallographic data and structure determination details for Na_4TtSe_4 with Tt = Si, Sn. Note that Na_4SiSe_4-$cP72$ was determined from powder data, and Na_4SnSe_4-$tI216$ from a single crystal.

compound	Na_4SiSe_4-$cP72$	Na_4SnSe_4-$tI216$
space group	$P\bar{4}3n$ (no. 218)	$I4_1/acd$ (no. 142)
formula weight / g mol^{-1}	435.9	526.5
shape, color	powder, brown	block, yellow
T / K	296	296
a / Å	12.1295(1)	14.4053(4)
c / Å		28.5751(8)
V / Å^3	1784.543(5)	5929.7(3)
Z	8	24
radiation	CuKα_1 (λ = 1.5406 Å)	MoKα (λ = 0.710 73 Å)
R_{int}		0.0295
profile R indexes	R_P = 0.0490, R_{wp} = 0.0681, R_{exp} = 0.0430	
goodness of fit	1.58	1.22
final R indexes [I>=3σ(I)]	R_1 = 0.0376, wR_1 = 0.0452	R_1 = 0.0187, wR_1 = 0.0422
final R indexes [all data]	R_2 = 0.0398, wR_2 = 0.0456	R_2 = 0.0274, wR_2 = 0.0451
$\Delta\rho_{\min}$, $\Delta\rho_{\max}$ / eÅ^{-3}	-0.79, 0.85	-1.29, 0.75

3.4.3 Formation, Stability and Electronic Structures of Na_4TtSe_4

Na_4SiSe_4 To further study the polymorphism, high temperature X-ray powder diffraction was performed starting from the ball milled reaction mixture. Thereby, the formation process of both modifications from binary Na_2Se_2 and Si can be followed by slowly heating the sample (Figure 3.4). Below 200 °C, only Na_2Se_2 (101, 2Θ = 23.4°) and Si (111, 2Θ = 28.5°) are present. With increasing temperature, at 250 °C, new reflections occur which can be assigned to Na_4SiSe_4-$oP36$ (102, 2Θ = 25.8°). At 350 °C, the formation of Na_4SiSe_4-$cP72$ (222, 2Θ = 25.2°; 004, 2Θ = 29.1°) can be observed. The cubic modification is stable only in a small temperature range (350 °C to 400 °C). At higher temperature, only Na_4SiSe_4-$oP36$ is observed. Even by cooling down to room temperature, the transformation to Na_4SiSe_4-$cP72$ cannot be detected again. Because of the reaction of Na with the quartz capillary, X-ray powder diffraction measurements at temperatures higher than 500 °C were not possible. A comparison of the total electronic energy shows that Na_4SiSe_4-$cP72$ is more stable by 8.5 kJ mol^{-1} (Figure 3.5) relative to Na_4SiSe_4-$oP36$. According to Ostwald's rule the metastable modification, Na_4SiSe_4-$oP36$, should crystallize before the

stable modification. This was confirmed by high temperature X-ray powder diffraction. It is remarkable that the cubic modification disappears at temperatures higher than 400 °C. Probably different thermodynamic and kinetic effects play a role here. Nevertheless, the high temperature X-ray powder diffraction experiment helps to determine the reaction conditions for the synthesis of new modifications even if they are only stable in a small temperature range. In accordance with the measurement, samples of Na_4SiSe_4-$cP72$ containing less than 5 % of Na_2Se_2 as a side phase can be obtained by heating up to 375 °C for 10 days.

To examine also higher temperatures, differential thermal analysis (DTA) of the ball milled reaction mixture was performed (heating/ cooling rate 5 °C min^{-1}) (Figure A.6). Formation peaks of Na_4SiSe_4-$cP72$ and Na_4SiSe_4-$oP36$, which are expected at approximately 300 °C and 400 °C are not visible. We assume that the formation reaction of the products is too slow in a relatively wide temperature range to be detectable via DTA. Peaks at 553 °C in the first cooling cycle and 548 °C in the second cooling cycle can be assigned to the crystallization temperature of Na_4SiSe_4-$oP36$. Samples of the ball milled reaction mixture as well as Na_4SiSe_4-$oP36$ were heated to 800 °C, subsequently cooled to 570 °C and 500 °C (5 °C min^{-1}) and quenched in water. All of these synthesis attempts only resulted in Na_4SiSe_4-$oP36$, so the DTA peaks probably stem from a recrystallization of Na_4SiSe_4-$oP36$. Quenching in water from 700 °C results in an amorphous product. DTA measurements of Na_4SiSe_4-$oP36$ and Na_4SiSe_4-$cP72$ are shown in the Supporting Information (Figures A.8 and A.7).

As mentioned before, equation of state calculations show Na_4SiSe_4-$cP72$ is more stable by 8.5 kJ mol^{-1} relative to Na_4SiSe_4-$oP36$ (Figure 3.5a). DFT modeling of Na_4SiSe_4 in different hypothetical structure types, which are known from Na_4GeSe_4 and Na_4SnSe_4, reveal only small energy differences. Hypothetical Na_4SiSe_4 in the Na_4SnS_4 structure type (Na_4SiSe_4-$tP18$, Figure 3.5d) is 1.9 kJ mol^{-1} lower in energy than Na_4SiSe_4-$cP72$. Hypothetical Na_4SiSe_4-$tI216$ (Na_4SnTe_4-$tI216$ structure type) and Na_4SiSe_4-$oP72$ (Na_4GeSe_4 structure type) are 3.0 kJ mol^{-1} and 8.1 kJ mol^{-1} higher in energy. Na_4SiSe_4-$oP36$, which was the first discovered modification, is 10.0 kJ mol^{-1} higher in energy relative to Na_4SiSe_4-$tP18$. As all considered structure types are relatively close in energy, the existence of further modifications of Na_4SiSe_4 seems plausible.

To check for stability of the most stable hypothetical modification of Na_4SiSe_4, the $tP18$ modification was additionally probed by calculation of phonon frequencies (Figure A.13). No physically relevant imaginary frequencies were obtained, thus indicating a dynamically

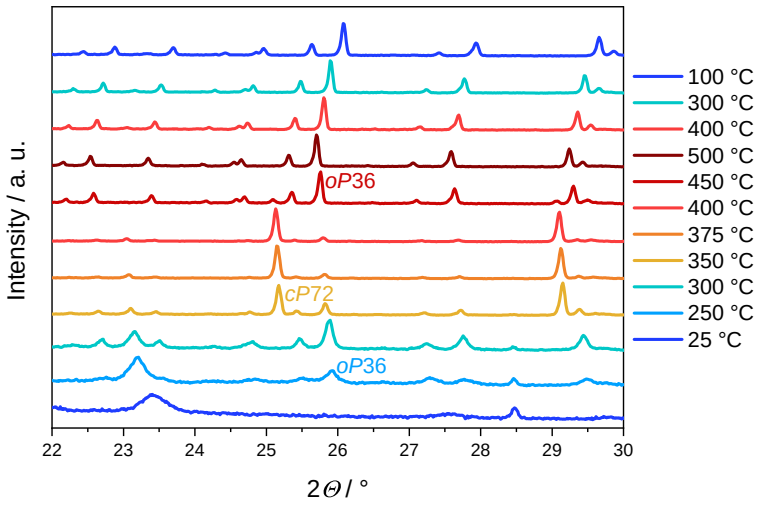

Figure 3.4 X-ray powder diffraction patterns of the ball milled reaction mixture of 'Na_4SiSe_4'. Up to 200 °C, Na_2Se_2 and Si are present. With further heating Na_4SiSe_4-$oP36$ forms. At 350 °C to 400 °C, Na_4SiSe_4-$cP72$ is present.

stable structure.

Na_4GeSe_4 Even though no further modification of Na_4GeSe_4 except the already known one Na_4GeSe_4-$oP72$ could be experimentally detected, DFT modeling of Na_4GeSe_4 in different possible structure types was performed. Calculated E-V-curves (Figure 3.5b) show that there are three possible modifications which are lower in energy than the experimentally observed one. Na_4GeSe_4-$tP18$ (Na_4SnS_4 structure type) and Na_4GeSe_4-$tI216$ (Na_4SnTe_4 structure type) are 12.2 kJ mol^{-1} and 11.2 kJ mol^{-1} lower in energy with respect to Na_4GeSe_4-$oP72$. Na_4GeSe_4-$cP72$ (Ba_4SiAs_4 structure type) is 0.03 kJ mol^{-1} lower in energy. Phonon frequencies were calculated for Na_4GeSe_4 in the Na_4SnS_4 structure type (Figure A.13). As no physically relevant imaginary frequencies were obtained, the existence of this modification seems plausible.

Na_4SnSe_4 DFT calculations reveal Na_4SnSe_4-$tI216$ to be metastable, as it is 2.5 kJ mol^{-1} higher in energy relative to Na_4SnSe_4-$tP18$.

In contrast to Na_4SiSe_4, for Na_4SnSe_4 both experimentally observed modifications are lower in energy than all other investigated structure types. Na_4SnSe_4-$tI216$ is 2.5 kJ mol^{-1} higher in energy relative to Na_4SnSe_4-$tP18$. Na_4SnSe_4 in the Na_4GeSe_4 structure type is 24.1 kJ mol^{-1} higher in energy. Na_4SnSe_4-$oP36$ (K_4SnSe_4 structure type) and Na_4SnSe_4-$cP72$ (Ba_4SiAs_4 structure type) are 29.6 kJ mol^{-1} and 37.7 kJ mol^{-1} higher in energy, respectively. The existence of further modifications of Na_4SnSe_4 in the other mentioned structure types seems rather unlike.

Band structures Electronic band structures of all title compounds were calculated within the DFT framework using the hybrid HSE06 and are shown in the Supporting Information (Figure A.11). Na_4SiSe_4-$oP36$ and Na_4SiSe_4-$cP72$ show direct band gaps of 4.01 eV and 4.28 eV, respectively. Na_4GeSe_4 exhibits an indirect band gap of 3.25 eV. Na_4SnSe_4-$tP18$ shows an direct band gap of 2.75 eV whereas Na_4SnSe_4-$tI216$ has a direct band gap of 2.50 eV. Experiments reveal two band gaps for Na_4SnSe_4-$tP18$ where the larger one corresponds to the calculated value (2.86 eV).[60] The band gap decreases going from Si to the higher homologues Ge and Sn. This is also in line with the observed colors of the synthesized powder samples and matches chemical expectation. Powder samples of both modifications of Na_4SiSe_4 are light brown to white, Na_4GeSe_4 appears light yellow and both modifications of Na_4SnSe_4 look yellow to orange.

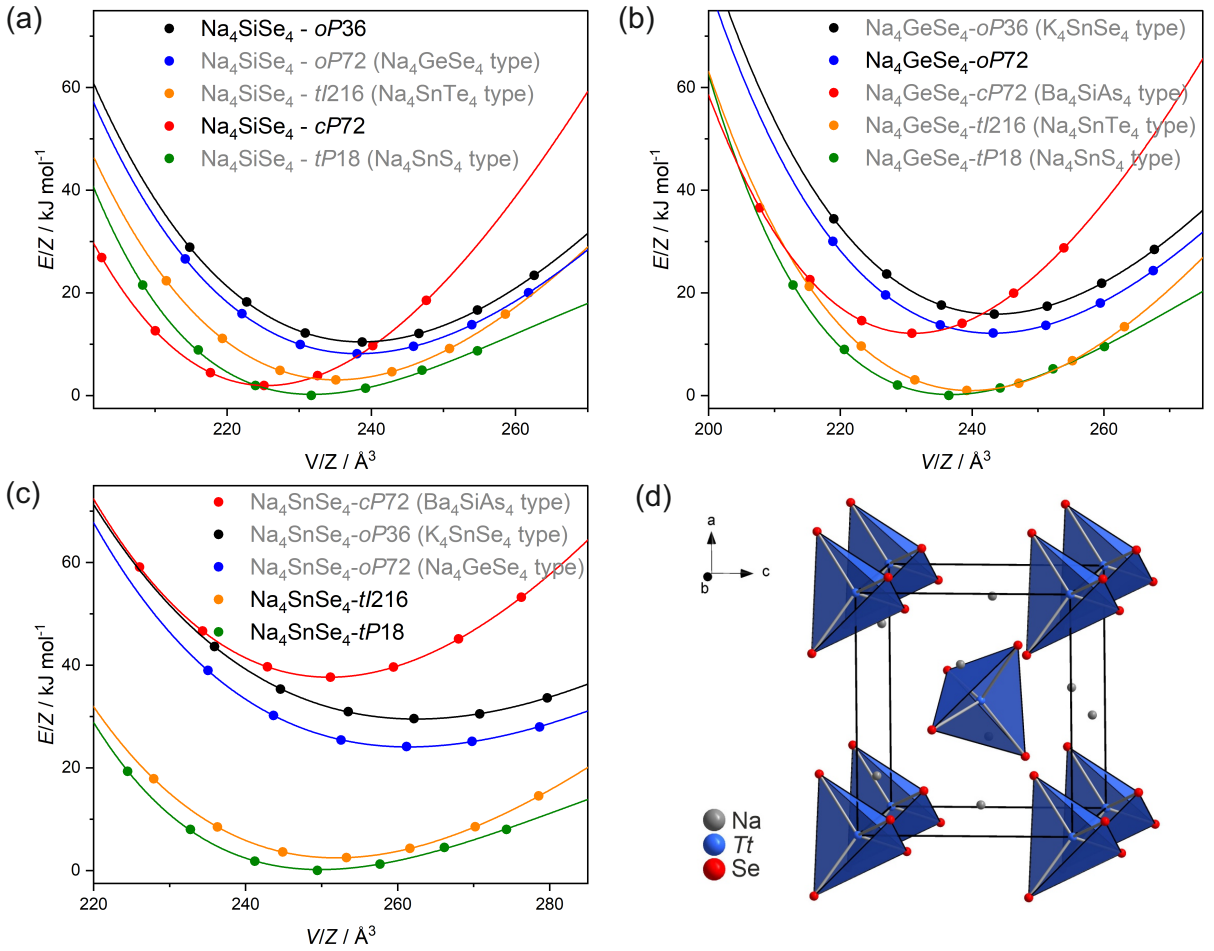

Figure 3.5 Calculated E vs. V curves for different (hypothetic) modifications of (a) Na_4SiSe_4 and (b) Na_4GeSe_4 and (c) Na_4SnSe_4. Hypothetical compounds are written in gray whereas the experimentally detected modifications are written in black. According to the E vs. V plots, no pressure dependent phase transition of the investigated compounds is expected. (d) Unit cell of the Na_4TtSe_4-*tP*18 structure with isolated $TtSe_4$-tetrahedra.

3.4.4 Impedance Spectroscopy

Samples of Na_4SiSe_4-*cP*72, Na_4SiSe_4-*oP*36, Na_4GeSe_4 and Na_4SnSe_4-*tI*216 were analyzed by impedance spectroscopy to check for Na ion conductivity. The size of the band gaps (DFT calculations and color of the samples) indicate that the measured conductivities are predominantly based on ion transport. This is also in line with the Nyquist plots and fitted impedance spectra (see Figure 3.6).

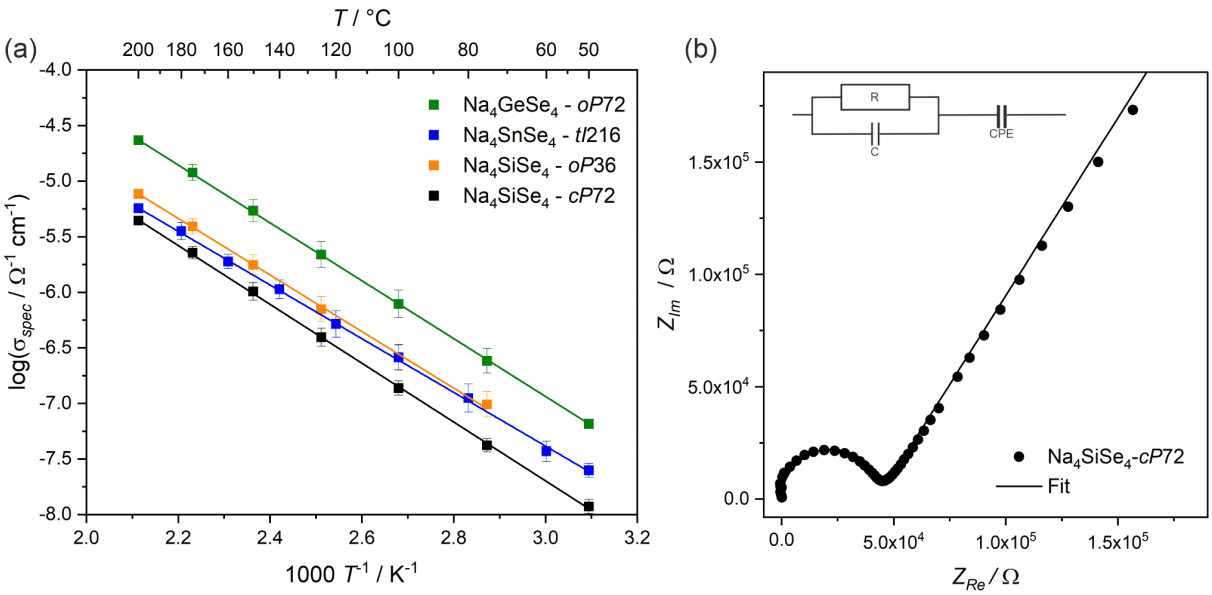

Figure 3.6 (a) Temperature dependent specific ionic conductivity of Na_4SiSe_4-*oP*36, Na_4SiSe_4-*cP*72 and Na_4SnSe_4-*tI*216 with linear fit (solid line). (b) Nyquist plot for Na_4SiSe_4-*cP*72 at 200 °C with fit.

Na_4GeSe_4-*oP*72 shows the highest conductivity with $\sigma_{spec} = 6.6 \times 10^{-8}\,\Omega^{-1}\,cm^{-1}$ at 50 °C and $\sigma_{spec} = 2.4 \times 10^{-5}\,\Omega^{-1}\,cm^{-1}$ at 200 °C. The activation energy of 0.52 eV was extracted from the Arrhenius plot of the fitted impedance data at different temperatures (Figure 3.6a). The other examined compounds showed slightly lower ionic conductivities. The temperature dependent specific ionic conductivities of all compounds are shown in Figure 3.6a. As there is no deviation from the linear behavior, phase transitions during the measurement can be excluded. In Figure 3.6b, a representative Nyquist plot of Na_4SiSe_4-*cP*72 is shown. Further Nyquist plots can be found in the Supporting Information (Figure A.14). Selected ionic conductivities and activation energies of all compounds are listed in Table 3.3. It has to be taken into account, that conductivity measurements differing by less than one order of magnitude are not significantly different. Despite structural differences of the investigated materials, there is no obvious rule to explain the trend

Table 3.3 Selected ionic conductivites and activation energies for Na_4SiSe_4-$oP36$, Na_4SiSe_4-$cP72$, Na_4GeSe_4-$oP72$ and Na_4SnSe_4-$tI216$ determined by impedance spectroscopy.

compound	$\sigma_{spec}(50\,°C)$/ $\Omega^{-1}\,cm^{-1}$	$\sigma_{spec}(200\,°C)$ / $\Omega^{-1}\,cm^{-1}$	E_a / eV
Na_4SiSe_4-$oP36$	1.0×10^{-7} [a]	7.7×10^{-6}	0.41
Na_4SiSe_4-$cP72$	1.1×10^{-8}	4.4×10^{-6}	0.53
Na_4GeSe_4-$oP72$	6.6×10^{-8}	2.4×10^{-5}	0.52
Na_4SnSe_4-$tI216$	2.5×10^{-8}	5.7×10^{-6}	0.47

[a] at 75 °C

in ionic conductivities of Na_4TtSe_4. A clear influence of the Na coordination on the ion conductivity is not visible. Generally speaking, a higher versatility in the Na coordination environment and the resulting flatter energy surface should enhance Na ion migration.[30] In comparison to the other investigated materials, the Na coordination environment in Na_4SiSe_4-$cP72$ is the least distorted. This corresponds to the lowest ion conductivity.
Other selenotetrelates like Na_4SnSe_4-$tP18$ and $Na_4Si_2Se_6$-$oP48$ show similar ionic conductivities ($\sigma_{spec} = 1.13 \times 10^{-8}\,\Omega^{-1}\,cm^{-1}$ at 20 °C[32] and $\sigma_{spec} = 1.4 \times 10^{-8}\,\Omega^{-1}\,cm^{-1}$ at 50 °C[29]).

3.5 Conclusions

Sodium selenotetrelate compounds Na_4TtSe_4 (Tt = Si, Ge, Sn) were synthesized by two step solid state reactions. The preparation of two new compounds was possible via a two-step synthesis procedure consisting of mechanochemical homogenization of the elements followed by annealing of the reaction mixture. The new modification of Na_4SiSe_4, Na_4SiSe_4-$cP72$, crystallizes in the cubic space group $P\bar{4}3n$ (no. 218) in the Ba_4SiAs_4 structure type and has a calculated band gap of 4.28 eV. The formation of both modifications from the ball milled reaction mixture was investigated by in-situ high-temperature X-ray powder diffraction. According to Ostwald's rule, at first a metastable modification, Na_4SiSe_4-$oP36$, is formed. By heating further Na_4SiSe_4-$cP72$ is observed which is stable up to 400 °C. At even higher temperatures, the cubic modification retransforms to Na_4SiSe_4-$oP36$. DFT calculations confirm Na_4SiSe_4-$cP72$ to be the more stable modification ($\Delta E = 8.6\,kJ\,mol^{-1}$). DFT modeling of further hypothetical structure types for the 4:1:4 composition revealed only small energy differences. Hypothetical Na_4SiSe_4-$tP18$

(Na_4SnS_4 structure type) is 1.9 kJ mol^{-1} lower in energy than Na_4SiSe_4-$cP72$, which was experimentally observed. Phonon dispersion calculations for Na_4SiSe_4-$tP18$ showed no imaginary frequencies. Therefore, the existence of this compound seems conceivable.
Also for Na_4SnSe_4 a new modification had been synthesized. The crystal structure was determined by single crystal X-ray diffraction. Na_4SnSe_4-$tI216$ crystallizes in the tetragonal space group $I4_1/acd$ (no. 142) in the Na_4SnTe_4-$tI216$ structure type with a calculated band gap of 2.50 eV. DFT calculations reveal Na_4SnSe_4-$tI216$ to be metastable. The already known modification, Na_4SnSe_4-$tP18$, is more stable by 2.5 kJ mol^{-1}. The phase transition was not examined in detail.
Calculations of E-V-curves for Na_4GeSe_4 in different hypothetic structure types show that there are three different structure types that are lower in energy with respect to the experimentally observed Na_4GeSe_4-$oP72$. The existence of further modifications of Na_4GeSe_4 seems plausible. Phonon dispersion calculations for Na_4GeSe_4 in the Na_4SnS_4 structure type show no imaginary frequencies and therefore indicate dynamic stability.
Impedance spectroscopy measurements were performed for all of the title compounds. All materials showed moderate sodium ion conductivity. The best ion conductivity was determined for Na_4GeSe_4 ($\sigma_{spec} = 6.6 \times 10^{-8}$ S cm^{-1} at 50 °C).

References

[1] Janek, J.; Zeier, W. G. *Nat. Energy* **2016**, *1*, 16141.

[2] Zhang, Z.; Shao, Y.; Lotsch, B.; Hu, Y.-S.; Li, H.; Janek, J.; Nazar, L. F.; Nan, C.-W.; Maier, J.; Armand, M.; Chen, L. *Energy Environ. Sci.* **2018**, *11*, 1945–1976.

[3] Yabuuchi, N.; Kubota, K.; Dahbi, M.; Komaba, S. *Chem. Rev.* **2014**, *114*, 11636–11682.

[4] Kundu, D.; Talaie, E.; Duffort, V.; Nazar, L. F. *Angew. Chem. - Int. Ed.* **2015**, *54*, 3431–3448.

[5] Delmas, C. *Adv. Energy Mater.* **2018**, *8*, 1703137.

[6] Jansen, M.; Henseler, U. *J. Solid State Chem.* **1992**, *99*, 110–119.

[7] Hayashi, A.; Noi, K.; Tanibata, N.; Nagao, M.; Tatsumisago, M. *J. Power Sources* **2014**, *258*, 420–423.

[8] Zhang, L.; Yang, K.; Mi, J.; Lu, L.; Zhao, L.; Wang, L.; Li, Y.; Zeng, H. *Adv. Energy Mater.* **2015**, *5*, 1501294.

[9] Krauskopf, T.; Pompe, C.; Kraft, M. A.; Zeier, W. G. *Chem. Mater.* **2017**, *29*, 8859–8869.

[10] Krauskopf, T.; Muy, S.; Culver, S. P.; Ohno, S.; Delaire, O.; Shao-Horn, Y.; Zeier, W. G. *J. Am. Chem. Soc.* **2018**, *140*, 14464–14473.

[11] Richards, W. D.; Tsujimura, T.; Miara, L. J.; Wang, Y.; Kim, J. C.; Ong, S. P.; Uechi, I.; Suzuki, N.; Ceder, G. *Nat. Commun.* **2016**, *7*, 11009.

[12] Duchardt, M.; Ruschewitz, U.; Adams, S.; Dehnen, S.; Roling, B. *Angew. Chem. - Int. Ed.* **2018**, *57*, 1351–1355.

[13] Tanibata, N.; Noi, K.; Hayashi, A.; Tatsumisago, M. *RSC Adv.* **2014**, *4*, 17120–17123.

[14] Kaib, T.; Bron, P.; Haddadpour, S.; Mayrhofer, L.; Pastewka, L.; Järvi, T. T.; Moseler, M.; Roling, B.; Dehnen, S. *Chem. Mater.* **2013**, *25*, 2961–2969.

[15] Minafra, N.; Hogrefe, K.; Barbon, F.; Helm, B.; Li, C.; Wilkening, H. M. R.; Zeier, W. G. *Chem. Mater.* **2021**, *33*, 727–740.

[16] Klepp, K. O. *Z. Naturforsch. B* **1985**, *40*, 878–882.

[17] Klepp, K. O. *Z. Naturforsch. B* **1992**, *47*, 411–417.

[18] Preishuber-Pflügl, H.; Klepp, K. O. *Z. Kristallogr. - New Cryst. Struct.* **2003**, *218*, 383–384.

[19] Eisenmann, B.; Jordan, H.; Schäfer, H. *Z. Anorg. Allg. Chem.* **1981**, *475*, 74–80.

[20] Schlirf, J.; Deiseroth, H. J.; Nilges, T. *Z. Kristallogr. - New Cryst. Struct.* **2000**, *215*, 343–344.

[21] Eisenmann, B.; Hansa, J. *Z. Kristallogr. - Cryst. Mater.* **1993**, *203*, 295–296.

[22] Eisenmann, B.; Hansa, J.; Schäfer, H. *Z. Naturforsch. B* **1985**, *40*, 450–457.

[23] Eisenmann, B.; Hansa, J.; Schäfer, H. *Rev. Chim. Minér.* **1984**, *21*, 817–823.

[24] Eisenmann, B.; Hansa, J.; Schäfer, H. *Z. Anorg. Allg. Chem.* **1985**, *526*, 55–59.

[25] Eisenmann, B.; Hansa, J. *Z. Kristallogr. - Cryst. Mater.* **1993**, *205*, 325–326.

[26] Eisenmann, B.; Hansa, J.; Schäfer, H. *Mater. Res. Bull.* **1985**, *20*, 1339–1346.

[27] Eisenmann, B.; Kieselbach, E.; Schäfer, H.; Schrod, H. *Z. Anorg. Allg. Chem.* **1984**, *516*, 49–54.

[28] Eisenmann, B.; Schwerer, H.; Schäfer, H. *Z. Naturforsch. B* **1981**, *36*, 1538–1541.

[29] Kamm, F.; Pielnhofer, F.; Schlosser, M.; Pfitzner, A. *Inorg. Chem.* **2023**, *62*, 11064–11072.

[30] Harm, S.; Hatz, A.-K.; Schneider, C.; Hoefer, C.; Hoch, C.; Lotsch, B. V. *Front. Chem.* **2020**, *8*, 90.

[31] Ben Yahia, H.; Motohashi, K.; Mori, S.; Sakuda, A.; Hayashi, A. *J. Alloys* **2023**, *960*, 170600.

[32] Gao, L.; Bian, G.; Yang, Y.; Zhang, B.; Wu, X.; Wu, K. *New J. Chem.* **2021**, *45*, 12362–12366.

[33] Hartmann, F.; Benkada, A.; Indris, S.; Poschmann, M.; Lühmann, H.; Duchstein, P.; Zahn, D.; Bensch, W. *Angew. Chem. - Int. Ed.* **2022**, *61*, e202202182.

[34] Matsushita, Y.; Kanatzidis, M. G. *Z. Naturforsch. B* **1998**, *53*, 23–30.

[35] Jumas, J.-C.; Philippot, E.; Vermot-Gaud-Daniel, F.; Ribes, M.; Maurin, M. *J. Solid State Chem.* **1975**, *14*, 319–327.

[36] Melullis, M.; Dehnen, S. *Z. Anorg. Allg. Chem.* **2007**, *633*, 2159–2167.

[37] WinXPow, Version 3.10; STOE & Cie GmbH, STOE & Cie GmbH: Darmstadt, 2016.

[38] Petříček, V.; Dušek, M.; Palatinus, L. *Z. Kristallogr. - Cryst. Mater.* **2014**, *229*, 345–352.

[39] Palatinus, L.; Chapuis, G. *J. Appl. Crystallogr.* **2007**, *40*, 786–790.

[40] CrysAlisPro (V42); Rigaku Oxford Diffraction Ltd, 2019.

[41] Zahner-Elektrik Zahner Analysis, Version 3.2.4; I. Zahner-Schiller GmbH & Co. KG, Kronach, 2023.

[42] Dovesi, R.; Erba, A.; Orlando, R.; Zicovich-Wilson, C. M.; Civalleri, B.; Maschio, L.; Rérat, M.; Casassa, S.; Baima, J.; Salustro, S.; Kirtman, B. *WIREs Comput. Mol. Sci.* **2018**, *8*, e1360.

[43] Dovesi, R. et al. CRYSTAL17 User's Manual; University of Torino, 2017.

[44] Sophia, G.; Baranek, P.; Sarrazin, C.; Rerat, M.; Dovesi, R., `https://www.crystal.unito.it/Basis_Sets/sodium.html`, Accessed: 2023-03-06, 2014.

[45] Porter, A. R.; Towler, M. D.; Needs, R. J. *Phys. Rev. B* **1999**, *60*, 13534–13546.

[46] Heyd, J.; Peralta, J. E.; Scuseria, G. E.; Martin, R. L. *J. Chem. Phys.* **2005**, *123*, 174101.

[47] Causà, M.; Dovesi, R.; Roetti, C. *Phys. Rev. B* **1991**, *43*, 11937–11943.

[48] Towler, M. D.; Zicovich-Wilson, C., `https://vallico.net/mike_towler/crystal.html`, Accessed: 2023-03-06, 1995.

[49] Becke, A. D. *Phys. Rev. A* **1988**, *38*, 3098–3100.

[50] Heyd, J.; Scuseria, G. E.; Ernzerhof, M. *J. Chem. Phys.* **2003**, *118*, 8207–8215.

[51] Perdew, J. P.; Burke, K.; Ernzerhof, M. *Phys. Rev. Lett.* **1996**, *77*, 3865–3868.

[52] Murnaghan, F. D. *Amer. J. Math.* **1937**, *59*, 235–260.

[53] Murnaghan, F. D. *Proc. Natl. Acad. Sci.* **1944**, *30*, 244–247.

[54] Birch, F. *Phys. Rev.* **1947**, *71*, 809–824.

[55] Hinuma, Y.; Pizzi, G.; Kumagai, Y.; Oba, F.; Tanaka, I. *Comput. Mater. Sci.* **2017**, *128*, 140–184.

[56] Pascale, F.; Zicovich-Wilson, C. M.; López Gejo, F.; Civalleri, B.; Orlando, R.; Dovesi, R. *J. Comput. Chem.* **2004**, *25*, 888–897.

[57] Zicovich-Wilson, C. M.; Pascale, F.; Roetti, C.; Saunders, V. R.; Orlando, R.; Dovesi, R. *J. Comput. Chem.* **2004**, *25*, 1873–1881.

[58] Föppl, H.; Busmann, E.; Frorath, F.-K. *Z. Anorg. Allg. Chem.* **1962**, *314*, 12–20.

[59] Zagler, R. Darstellung und Strukturchemie von Chalkogenido-Polyanionen und Chalkogenidoindaten, -germanaten, -stannaten, -arsenaten, -antimonaten bzw. -telluraten mit komplexierten und nicht komplexierten Kationen, Ph.D. Thesis, Universität Darmstadt, 1988.

[60] Palchik, O.; Gedanken, A.; Palchik, V.; Slifkin, M.; Weiss, A. *J. Solid State Chem.* **2002**, *165*, 125–130.

4 Synthesis and Characterization of $Na_4Si_2Se_6$-*tP*24 and $Na_4Si_2Se_6$-*oP*48, Two Polymorphs with Different Anionic Structures

4.1 Preface and Abstract

This chapter is reprinted and adapted with permission from *Inorganic Chemistry* **2023**, *62*, 11064-11072.

Several people contributed to this work:

- Franziska Kamm performed the experimental work and the DFT calculations and wrote and improved the manuscript.
- Dr. Florian Pielnhofer supervised the DFT calculations, contributed with discussions and improved the manuscript.
- Dr. Marc Schlosser performed the MAPLE calculations, contributed with discussions and improved the manuscript.
- Prof. Dr. Arno Pfitzner contributed with discussions, supervised the experimental work and improved and corrected the manuscript.

Abstract

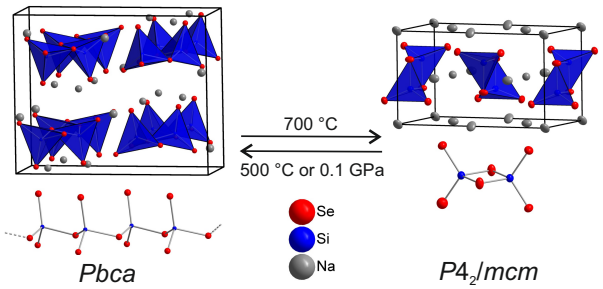

Two different polymorphs of the new selenosilicate $Na_4Si_2Se_6$ were synthesized by solid state reactions. The high temperature polymorph $Na_4Si_2Se_6$–*tP*24 crystallizes in the tetragonal space group $P4_2/mcm$ (No. 132) with lattice parameters a = 7.2793(2) Å, c = 12.4960(4) Å and V = 662.14(3) Å^3. Main structural motifs are isolated Si_2Se_6-units of two edge-sharing $SiSe_4$–tetrahedra. The high pressure/ low temperature polymorph $Na_4Si_2Se_6$–*oP*48 crystallizes in the orthorhombic space group *Pbca* (No. 61) with lattice parameters a = 12.9276(1) Å, b = 15.9324(1) Å, c = 6.0349(1) Å

and $V = 1243.00(2)\,\text{Å}^3$ showing *zweier* single chains $^1_\infty[Si_2Se_6]^{4-}$. Lattice parameters of $Na_4Si_2Se_6$-*tP*24 were determined by single crystal X-ray diffraction, whereas those of $Na_4Si_2Se_6$-*oP*48 were investigated by powder X-ray diffraction. Both modifications crystallize in new structure types. An energetic comparison of the two polymorphs and further hypothetical structure types was carried out by DFT modeling. Calculations reveal that the polymorphs are very close in energy ($\Delta E = 3.4\,\text{kJ mol}^{-1}$). Impedance spectroscopic measurements show ionic conductivity ($\sigma_{spec} = 1.4 \times 10^{-8}\,\text{S cm}^{-1}$ at 50 °C and $6.8 \times 10^{-6}\,\text{S cm}^{-1}$ at 200 °C) with an activation energy of $E_A = 0.54(2)\,\text{eV}$ for $Na_4Si_2Se_6$-*oP*48.

4.2 Introduction

Only four compounds in the ternary system Na-Si-Se are known to date. There are a variety of different anionic units found in these compounds. All consist of tetrahedral $SiSe_4$ moieties which are linked in different ways. In Na_4SiSe_4,[1] isolated $SiSe_4$-tetrahedra were observed. Anionic units consisting of two vertex-sharing $SiSe_4$-tetrahedra are found in the selenodisilcate $Na_6Si_2Se_7$.[2] In the perselenodisilicate $Na_6Si_2Se_8$,[3] two $SiSe_4$-tetrahedra are connected by a Se-Se covalent bond. In $Na_4Si_4Se_{10}$,[4] four $SiSe_4$-tetrahedra are connected via common corners forming isolated adamantane-like units. No edge sharing $SiSe_4$-tetrahedra are yet observed in the Na-Si-Se system. Besides the crystal structure, no additional information about chemical or physical properties of these compounds are available in the literature.

Dimeric edge-sharing T_2Q_6-tetrahedra dimers exist in the $Rb_4Sn_2Se_6$,[5] $Cs_4Sn_2Se_6$,[6] $K_4Sn_2Te_6$[7] and $K_4Sn_2Se_6$[8] type structures for ternary compounds containing an alkali metal, a tetrel (T = Si, Ge, Sn) and a chalcogenide (Q = S, Se, Te). All known representatives containing such anionic units are listed in Table 4.1.

Table 4.1 Compounds containing a $T_2Q_6{}^{4-}$-unit

compounds	structure type	space group
$K_4Sn_2S_6$,[9] $K_4Ge_2Se_6$[10]	$K_4Sn_2Se_6$[8]	$P\bar{1}$ (No. 2)
$K_4Sn_2Te_6$[7]	own structure type	*Cmce* (No. 64)
$Rb_4Sn_2Se_6$[5]	own structure type	$P\bar{1}$ (No. 2)
$Rb_4Si_2S_6$,[11] $Rb_4Ge_2S_6$,[12] $Rb_4Ge_2Se_6$,[13] $Cs_4Si_2S_6$,[14] $Cs_4Ge_2Se_6$[15]	$Cs_4Sn_2Se_6$[6]	$C2/m$ (No. 12)

For the 2 : 1 : 3 (4 : 2 : 6) molar ratio also compounds with other structural motifs of the complex anion are known. Besides cyclosilicates[16] and compounds with five-fold[17] and a six-fold[18] coordination of Sn, infinite chains of corner sharing TQ_4-tetrahedra exist in the $Na_4Ge_2S_6$,[4] $Na_4Sn_2S_6$,[19] $Na_{12}Sn_6Se_{18}$,[20] $Li_4Sn_2Se_6$,[21] $Li_4Si_2O_6$[22] and $K_4Ge_2O_6$[23] structure types. All known representatives of the 2-1-3 chain like tetrelates are listed in Table 4.2. The number of T atoms in one repetitive unit of the chain is represented by the chemical formulas. According to the nomenclature of Liebau,[24] compounds with the sum formula $M_4T_2Q_6$ (M = alkali metal) posses a *zweier* single chain ($^1_\infty[T_2Q_6{}^{4-}]$) whereas in $Na_{12}Sn_6Se_{18}$ a *sechser* single chain ($^1_\infty[Sn_6Se_{18}{}^{12-}]$) is present. The chains are named *zweier* or *sechser* single chains according to the number of TQ_4 tetrahedra in the repetition unit of the chains.

Table 4.2 Alkali chalcogenotetrelates containing infinite chains of edge-sharing TQ_4-tetrahedra

compounds	structure type	space group
$Na_4Ge_2S_6$,[4] $Na_4Ge_2Se_6$,[4] $Na_4Sn_2Se_6$[3]	$Na_4Ge_2S_6$	$P2_1/c$ (No. 14)
$Na_4Sn_2S_6$[19]	own structure type	$Ama2$ (No. 40)
$Na_{12}Sn_6Se_{18}$[20]	own structure type	$Pnma$ (No. 62)
$Li_4Sn_2Se_6$[21]	own structure type	Cc (No. 9)
$Li_4Si_2O_6$,[22] $Li_4Ge_2O_6$,[25] $Li_4Si_2S_6$,[26] $Na_4Si_2O_6$,[27] $Na_4Ge_2O_6$[28]	$Li_4Si_2O_6$	$Cmc2_1$ (No. 36)
$K_4Ge_2O_6$[23]	own structure type	$Pbca$ (No. 61)

The size of the alkali metal cations seems to influence the type of the anionic unit, edge-linked dimer or corner-linked chain, in the adopted crystal structure. In compounds with the lighter alkali metals Li and Na only the anionic tetrahedral chain occur, while edge linked T_2Q_6-dimers are present in the Rb and Cs compounds. In the intermediate K compounds, the anion forms either a chain or a dimer.

Even if polymorphism is observed in the discussed class of compounds, the tetrahedra linking in the anion is always of the same type i. e., a chain remains a chain and a dimer remains a dimer during the phase transition. Here we report about the first example of chalcogenotetrelates forming two polymorphs with completely different anionic structures.

A knowledge of the physical properties of sodium chalcogenotetrelates is very scarce in literature. Ionic conductivities have only been reported for a few chalcogenotetrelates, e.g. for Na_4SiS_4 which shows moderate sodium ion conductivity ($1.64\times10^{-7}\,S\,cm^{-1}$ at 25 °C).[29] The tin compounds Na_4SnS_4 and Na_4SnSe_4 show ionic conductivities in the same order

of magnitude ($2.18 \times 10^{-8}\,\mathrm{S\,cm^{-1}}$ and $2.19 \times 10^{-8}\,\mathrm{S\,cm^{-1}}$ at 30 °C).[30] Therefore, sodium ion conductivity is also expected for other materials in the Na - Si - Se system, which is proven for the title compound $Na_4Si_2Se_6$-*oP*48 by impedance spectroscopy. Herein we report on the synthesis and characterization of two polymorphs of $Na_4Si_2Se_6$. One of these modifications can be regarded as high pressure/ low temperature modification. Both polymorphs were furthermore characterized by calculating the electrostatic contributions to the respective lattice energy[31] (MAPLE) and DFT modeling of stability and band structures.

4.3 Experimental Methods

4.3.1 Synthesis

High temperature synthesis Microcrystalline bulk material of both title compounds can be synthesized via ball-milling of the elements sodium (Sigma-Aldrich, 99.8 %), silicon (silicon wafer, siltronic) and selenium (ChemPur, 99.99 %) in the molar ratio 2 : 1 : 3. For the synthesis, a FRITSCH pulverisette 7 premium line ball mill with 25 mL zirconia grinding bowls and 10 grinding balls ($\varnothing = 10\,\mathrm{mm}$) of the same material were used. For a good homogenization, 5 slower milling cycles (300 rpm for 3 min) followed by 10 milling cycles with a top speed of 500 rpm for 5 min, were performed. In each case, 0.3 g of the reaction mixture were transferred to graphitized silica ampoules, which were subsequently evacuated, flame sealed and then heated in tube furnaces. Single crystals of $Na_4Si_2Se_6$-*tP*24 are obtained from direct reaction of the elements. *High pressure synthesis* High pressure experiments were conducted in BN crucibles in a Belt apparatus according to *Range* and *Leeb*.[32]
A detailed description of the reaction conditions is given in the *Results and Discussion*. The prepared compounds are sensitive to moisture and air, and therefore all manipulations were carried out under inert gas conditions (GloveBox M Braun) with oxygen and H_2O levels below 0.5 ppm. The compounds decompose forming the toxic gas H_2Se in contact with air.

4.3.2 Single crystal X-ray diffraction (sc-XRD)

All crystal manipulations were done under fomblin® oil. The diffraction experiment was performed at 300 K on a Rigaku XtaLAB Synergy R DW System with a HyPix-Arc 150 detector using Cu Kα radiation ($\lambda = 1.541\,84$ Å). The cell determination, data reduction,

and absorption correction were done with the *CrysAlis Pro* software.[33] The structure was solved by using the *Superflip*[34] algorithm implemented in *Jana2006*[35] which was also used for structure refinement. The crystallographic data for $Na_4Si_2Se_6$-*tP*24 have been deposited at CCDC/FIZ Karlsruhe as CSD 2254481.

4.3.3 Powder diffraction (PXRD)

Finely ground samples were filled in quartz capillaries ($\varnothing$ = 0.3 mm) that were subsequently sealed. The capillaries were mounted on a STOE STADI P diffractometer (Stoe & Cie) equipped with a Mythen 1K detector and measured using Cu Kα_1 radiation (λ = 1.5406 Å). For raw data handling, the *WinXPow*[36] software package (Stoe & Cie) was used. Structure solution and Rietveld refinements were performed using *Jana2006*[35] and the implemented *Superflip*[34] algorithm. The crystallographic data for $Na_4Si_2Se_6$-*oP*48 have been deposited at CCDC/FIZ Karlsruhe as CSD 2254482.

4.3.4 Impedance spectroscopy

For impedance experiments a *Zahner Zennium* impedance analyzer coupled with an homemade furnace was used. The whole set up was installed in a glovebox to prevent reactions with air or moisture during the measurement. No measurements at temperatures below 50 °C were possible due to this set-up. A powder sample of $Na_4Si_2Se_6$-*oP*48 was cold-pressed ($\varnothing$ = 8 mm) and placed in contact with gold electrodes. Two measurement cycles from 50 to 200 °C in steps of 10 °C in the frequency range from 1 MHz to 100 mHz showed ionic conductivity. An excitation voltage of 50 mV was used. *Zahner Analysis*[37] software was used for data processing and fitting. Nyquist plots were fitted by an equivalent circuit consisting of a resistor and capacitor in parallel combined with a CPE in parallel with a second capacitor (see Figure B.14). R was used to determine the overall resistance of the sample. R and the resulting σ_{spec} were corrected by including the density of the pellet.

4.3.5 DFT modeling

All quantum chemical calculations were performed using the CRYSTAL17 code.[38,39] Basis sets[40–42] were taken from the literature, and the outer shells of all basis sets were additionally adjusted so that the calculated energy is minimized. Basis sets for Ge[43] and Sn[40] were used without further adjustment. Full structure optimizations were performed starting from the experimentally determined structure models. All calculations

were performed using a k-mesh sampling of 6 × 6 × 6. For geometry optimizations, the local density approximation (LDA)[44] functional, the generalized gradient approximation (GGA) functionals PBE,[45] PBE with D3 correction[46,47] and PBEsol[48] and the hybrid functionals PBE0[49] and HSE06[50,51] were used. For the calculations of E-V-curves and the transition pressure the HSE06 functional was chosen. The convergence criterion was set to 1×10^{-8} atomicunits (a.u.). The E–V curves were calculated using constant volume optimizations starting from preoptimized geometries. Starting models for hypothetical compounds $Na_4Si_2Se_6$ in different possible structure types were taken from literature and preoptimized with atom types replaced according to the desired composition. The calculated values were then fitted to the Birch – Murnaghan equation of state[52–54] (EOS) to determine the transition pressure of the two polymorphs. Band structures and density of states (DOS) were calculated for both polymorphs using k paths proposed by Setyawan and Curtarolo.[55]

4.4 Results and Discussion

4.4.1 Synthesis

Microcrystalline bulk materials of $Na_4Si_2Se_6$-*tP*24 and $Na_4Si_2Se_6$-*oP*48 can be synthesized by ball-milling of a stochiometric mixture of the elements followed by annealing. This first step of the synthesis results in a homogeneous mixture of Na_2Se_4 and Si (Figure B.1). Due to the small particle size after ball milling, the reflections are rather broad, but there is no hint that a ternary compound is already formed after this step. To synthesize the ternary compounds, the reaction mixture was annealed at 500 °C for 7 d and at 650 °C for 7 d in the case of $Na_4Si_2Se_6$-*oP*48 (high pressure/ low temperature polymorph) and $Na_4Si_2Se_6$-*tP*24 (high temperature polymorph), respectively. Both powders are light grey. Yellow single crystals of $Na_4Si_2Se_6$-*tP*24 were obtained by the direct reaction of Na, Si, and Se in a stoichiometric ratio at 600 °C for 3 days. The synthesis of single crystals of $Na_4Si_2Se_6$-*oP*48 was not successful probably due to the low phase transition temperature. The low temperature polymorph $Na_4Si_2Se_6$-*oP*48 was obtained from $Na_4Si_2Se_6$-*tP*24 both by annealing at lower temperatures (500 °C) and by applying pressure, as expected for a low-temperature or high-pressure modification, respectively. In two different experiments, pressures of 0.1 GPa and 3 GPa were applied to $Na_4Si_2Se_6$-*tP*24 for 1 h and 24 h, respectively. The pressure was chosen according to the calculated transition pressure of 0.3 GPa (see the *DFT modeling* section). Afterwards, the pellets were ground to fine powders,

which were than analyzed by X-ray powder diffraction. In both samples a mixture of both polymorphs was present. The PXRD patterns are shown in Figures B.12 and B.13. Differential thermal analysis (DTA) was performed to determine the phase transition temperature. When a sample of the low-temperature/ high-pressure polymorph $Na_4Si_2Se_6$-*oP*48 is heated, multiple effects are visible, but none of them can be clearly assigned to the occurring phase transition (Figure B.16). Two explanations are possible: either the phase transition is too slow to give a strong signal or the signal is very weak due to energetic similarity of the two polymorphs, vide infra. Experimentally, the high-temperature polymorph can be obtained from the low-temperature polymorph by annealing the latter at 700 °C for 6 days. In the opposite case, the high temperature modification $Na_4Si_2Se_6$-*tP*24 can be transformed to the high pressure/ low temperature polymorph $Na_4Si_2Se_6$-*oP*48 at temperatures below 650 °C for 4 days without the application of pressure.

4.4.2 Crystal Structure of $Na_4Si_2Se_6$-*tP*24

The crystal structure of $Na_4Si_2Se_6$-*tP*24 was determined by PXRD at room temperature and sc-XRD at 300.0(1) K. The following data refer to the single crystal measurement. The refined PXRD pattern and difference plot are shown in Figure B.2. Refinement results are listed in Table B.2.

The title compound $Na_4Si_2Se_6$-*tP*24 (high-temperature modification) crystallizes in the tetragonal space group $P4_2/mcm$ (No. 132) with lattice parameters a = 7.2793(2) Å, c = 12.4960(4) Å and V = 662.14(3) Å^3. Edge-sharing $[Si_2Se_6]^{4-}$ tetrahedra dimers are the main structural motif (see Figure 4.1). Crystallographic details are listed in Table 4.3. For more detailed information, see Table B.1.

The Si atoms are coordinated tetrahedrally by Se1 and Se2. Two of these tetrahedra are connected via a common edge to form $Si_2Se_6^{4-}$ units. The Si-Se distances are 2.219(1) Å for terminal Se1 and 2.325(1) Å for bridging Se2. Such a difference in bond lengths for terminal and bridging Q atoms is also known for oxosilicates and thiosilicates and thus meets the expectation for selenosilicates. In $Na_6Si_2Se_7$, which shows dimers of $SiSe_4$ tetrahedra sharing common corners, Si-Se distances are comparable (d(Si-Se_{term} = 2.230 Å - 2.273 Å, d(Si-Se_{br}) = 2.3336 Å).[2] Se-Si-Se bond angles are between 95.14(1)° (Se_{br}-Si-Se_{br}) and 113.33(1)° (Se_{term}-Si-Se_{term}).

There are three independent sodium positions. Na1 and Na2 are coordinated tetrahedrally by four Se atoms (d(Na1-Se1) = 3.063(1) Å, d(Na2-Se1) = 2.878(1) Å). Na1 is coordinated by four further Se in a second coordination sphere (d(Na1-Se2) = 3.564(1) Å). Na3

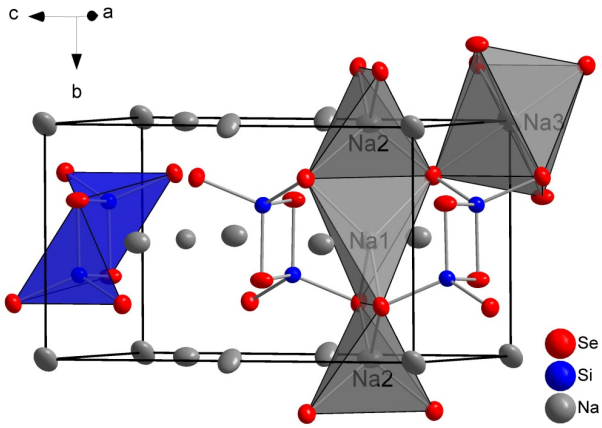

Figure 4.1 Unit cell of $Na_4Si_2Se_6$-*tP*24 with coordination polyhedra around Na and Si.

is coordinated octahedrally (d(Na3-Se1) = 3.001(1) Å, d(Na3-Se2) = 3.431(1) Å). Coordination polyhedra of Si and Na with all interatomic distances are shown in Figures 4.1 and 4.2.

Na-Se distances in other sodium selenosilicates, e.g. in $Na_6Si_2Se_7$, are similar (d(Na-Se) = 2.821 Å - 3.554 Å).[2] Na-Se distances of tetrahedrally coordinated Na differ only slightly from the Na-Se distances in Na_2Se (2.955 Å).[56]

Coordination polyhedra of Na1 and Na2 are connected via common edges and are thus forming chains in a and b direction. In between these chains lie the Na3 coordination polyhedra, sharing common corners with Na1 and Na2 coordination polyhedra. A excerpt of the resulting 3D network is shown in Figure 4.1.

$Na_4Si_2Se_6$-*tP*24 represents the first alkali metal selenosilicate with dimeric Si_2Se_6-anions. $Si_2Se_6^{4-}$-dimers are only found in $Tl_4Si_2Se_6$[57] which contains an about 50 % larger cation (ionic radius of 1.5 Å for Tl^+ vs. 1.02 Å for Na^+ in six-fold coordination).[58] $Na_4Si_2Se_6$-*tP*24 crystallizes in a new structure type with a different packing of the anions.

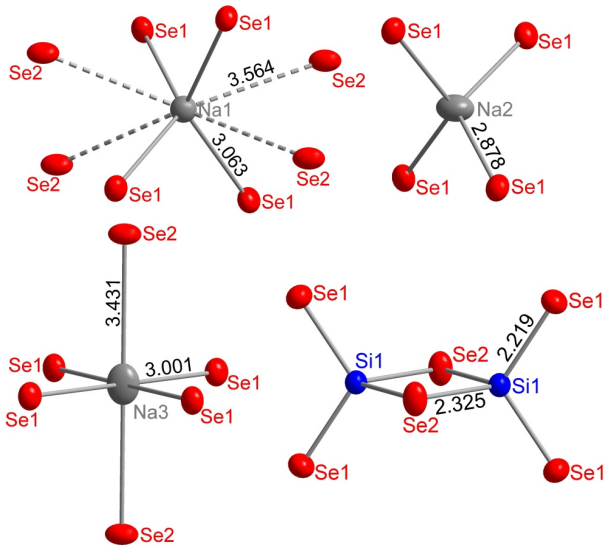

Figure 4.2 Coordination polyhedra of all Na positions and Si with distances in Å in $Na_4Si_2Se_6$-$tP24$.

Table 4.3 Crystallographic details for $Na_4Si_2Se_6$-$tP24$ and $Na_6Si_2Se_6$-$oP48$

chemical formula	$Na_4Si_2Se_6$-$tP24$	$Na_4Si_2Se_6$-$oP48$
fw / g mol^{-1}	621.9	
shape, color	block, yellow	powder, grey
T / K	300.0(1)	296
crystal system	tetragonal	orthorhombic
space group	$P4_2/mcm$ (No.132)	$Pbca$ (No. 61)
a / Å	7.2793(2)	12.9276(1)
b / Å		15.9324(1)
c / Å	12.4960(4)	6.0349(1)
V / Å^3	662.14(3)	1243.00(2)
Z	2	4
radiation	CuKα	CuKα_1
R_{int}	0.0364	
profile R indexes		$R_p = 0.0490$, $R_{wp} = 0.0617$, $R_{\text{exp}} = 0.0421$
goodness of fit	1.73	1.47
final R indexes [$I >= 3\sigma(I)$]	$R_1 = 0.0162$, $wR_2 = 0.0212$	$R_1 = 0.0281$, $wR_2 = 0.0352$
final R indexes [all data]	$R_1 = 0.0173$, $wR_2 = 0.0216$	$R_1 = 0.0282$, $wR_2 = 0.0352$
$\Delta\rho_{min}$, $\Delta\rho_{max}$ / e/Å^3	-0.49, 0.26	-0.60 0.67

4.4.3 Crystal structure of $Na_4Si_2Se_6$-*oP*48

The crystal structure of $Na_4Si_2Se_6$-*oP*48 was determined by structure solution with *Superflip* followed by Rietveld refinement of PXRD pattern (see Figure 4.3).

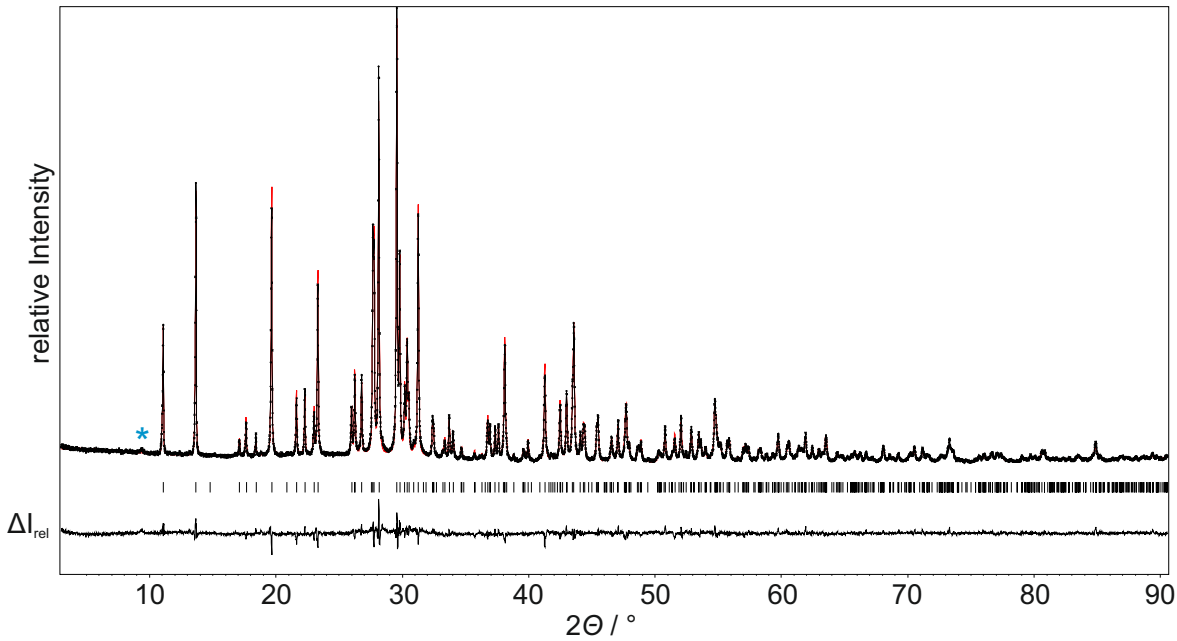

Figure 4.3 Refined PXRD pattern of $Na_4Si_2Se_6$-*oP*48 with difference plot, measured with Cu Kα_1 radiation at room temperature. The unindexed reflection is marked with a blue star.

$Na_4Si_2Se_6$-*oP*48 crystallizes in the orthorhombic space group *Pbca* (No. 61) with the lattice parameters $a = 12.9276(1)$ Å, $b = 15.9324(1)$ Å, $c = 6.0349(5)$ Å and $V = 1243.00(2)$ Å^3. All atoms are in the general Wyckoff position 8*c*. Crystallographic details are listed in Table 4.3. For more details, see B.5. In contrast to the previously described crystal structure, the main structural feature now are chains of corner-sharing $SiSe_4$ tetrahedra (Figure 4.5a) forming *zweier* single chains $^1_\infty[Si_2Se_6{}^{4-}]$. In the $SiSe_4$ tetrahedra, Si – Se distances are 2.210(4) Å and 2.235(5) Å for terminal Se atoms and 2.357(5) Å and 2.300(4) Å for bridging Se atoms. All chains are aligned parallel to the crystallographic *c* direction. There are two crystallographically independent Na positions. Na1 is coordinated trigonal bipyramidally by Se with distances from 2.968(6) Å to 3.099(7) Å. Na2 is coordinated octahedrally with Na – Se distances from 2.896(6) Å to 3.373(7) Å. Therefore, the coordination number of Na in the high pressure polymorph $Na_4Si_2Se_6$-*oP*48 (mean value 5.5) is higher than in the high temperature polymorph $Na_4Si_2Se_6$-*tP*24 (mean value 5), as ex-

pected for high pressure modifications. All coordination polyhedra and atomic distances are shown in Figure 4.5a. Na-Se coordination polyhedra are connected to a 3D network by common corners and edges (see Figure 4.4).

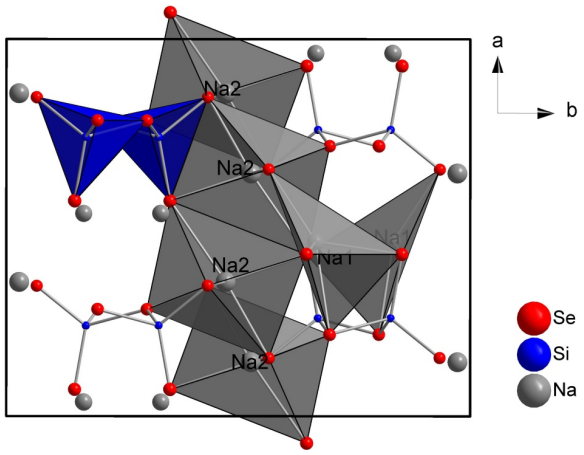

Figure 4.4 Unit cell of $Na_4Si_2Se_6$-$oP48$ containing four tetrahedral chains running parallel to *c*. Coordination polyhedra of Na1 and Na2 share common corners and edges, forming a 3D network.

As mentioned in the Introduction there are various other ternary alkali chalcogenotetrelates with chains of edge-sharing TQ_4–tetrahedra. $Na_4Ge_2Se_6$[4] is structurally very similar to the here reported $Na_4Si_2Se_6$-$oP48$. The tetrahedra chains in both compounds can be defined as *zweier* single chains in the nomenclature of Liebau.[24] Also, the Na coordination is very similar in these materials. The main difference is the arrangement of the chains. There is only one crystallographically independent T position in both compounds and therefore all tetrahedra chains are crystallographically equivalent. In both compounds, T is not exactly in the center of the Q tetrahedra but slightly shifted toward the terminal Q atoms (Figure 4.5a). This is also known for other compounds, e.g. polysulfates.[59] Coloring of the longest Si-Se bond emphasizes that the chains present in the unit cell of $Na_4Si_2Se_6$-$oP48$ differ in their orientation but are crystallographically equivalent (Figure 4.5b). In $Na_4Si_2Se_6$ there are two chains of each type per unit cell adding up to four, i. e., two + two, chains per unit cell.

In Figures 4.6a and b the different chains in $Na_4Si_2Se_6$-$oP48$ and in $Na_4Ge_2Se_6$ are shown in different colors from different viewing directions. The chains differ in their arrangement relative to each other which is obvious as the two structures crystallize in different space groups. The glide plane *a* in *Pbca* leads to 2+2 tetrahedra chains per unit cell for $Na_4Si_2Se_6$-$oP48$ resulting in a doubling of the unit cell in *a* direction compared to the

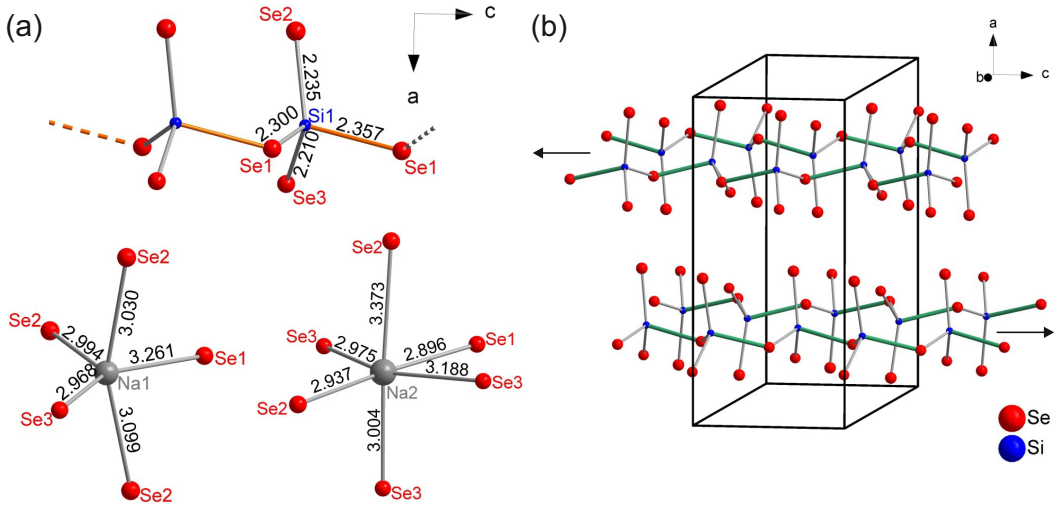

Figure 4.5 (a) Coordination polyhedra of Si1, Na1 und Na2 with distances in Å. (b) Unit cell of $Na_4Si_2Se_6$-*oP*48 containing four (two + two) chains of corner-sharing $SiSe_4$-tetrahedra parallel to *c*. All chains are crystallographically equivalent. To make the different orientations of the chains visible, the longest Si-Se distance in the tetrahedra is shown in green. The different orientations are additionally clarified by arrows. Two chains are oriented in the *c* direction and two chains in the -*c* direction. Na atoms are omitted for clarity.

$Na_4Ge_2S_6$ type structure. Both structure types are closely related as $P2_1/c$ ($Na_4Ge_2Se_6$) is a subgroup of *Pbca* ($Na_4Si_2Se_6$-*oP*48).

Comparing the polymeric anion in the higher homologous chalcogenotetrelates to the corresponding oxosilicates also reveals some similarities. *Zweier* single chains which where found in $Na_4Si_2Se_6$-*oP*48 are also present in $Na_4Si_2O_6$[27] (crystallizing in the $Li_4Si_2O_6$-structure type,[22] Figure 4.6c). In contrast to the compounds discussed previously, $Na_4Si_2O_6$ crystallizes in the space group $Cmc2_1$, which contains also mirror planes *m* in addition to glide planes. Therefore, all tetrahedra chains are oriented in the same direction. The SiO_4-tetrahedra are not tilted against each other (see Figure 4.6c, viewing in the crystallographic *c* direction).

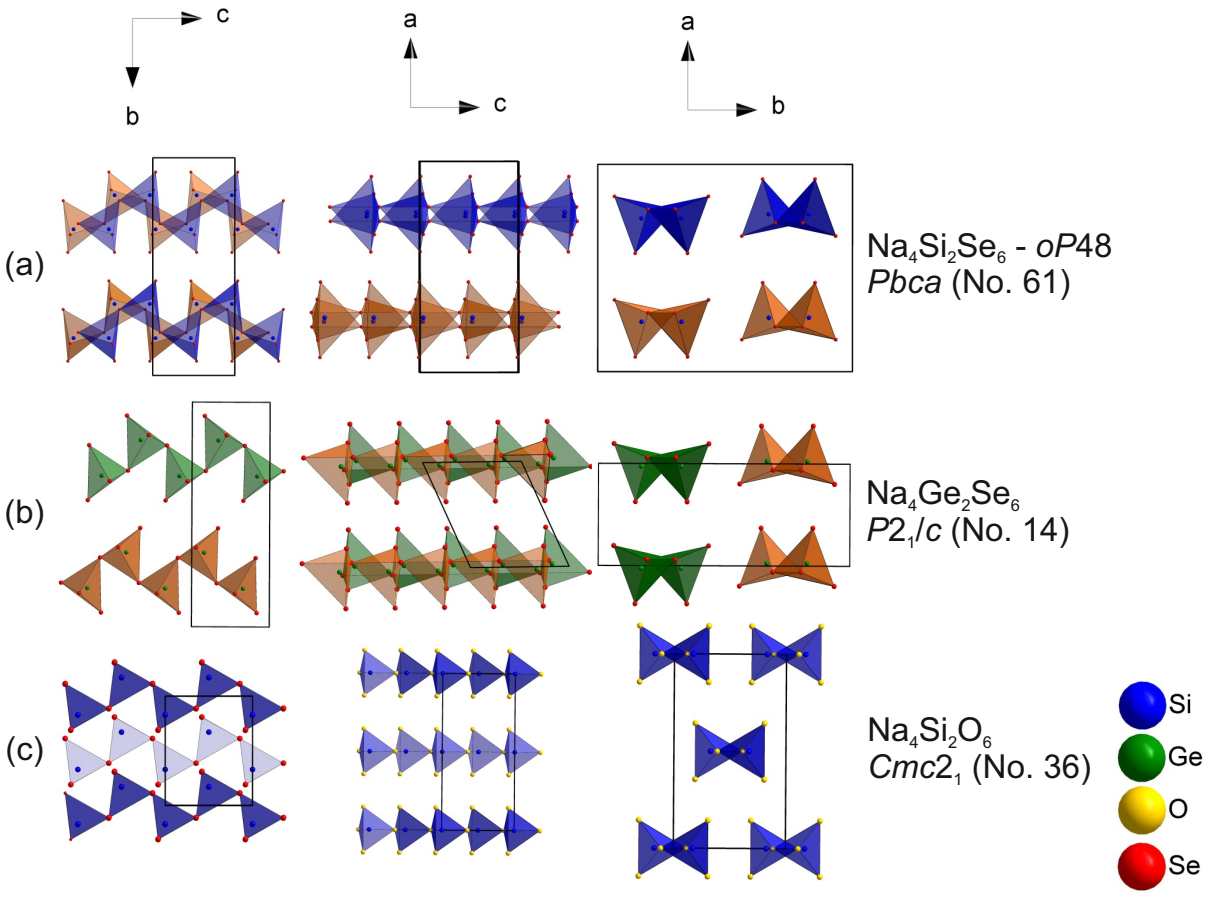

Figure 4.6 Unit cells of **(a)** $Na_4Si_2Se_6$-*oP*48, **(b)** $Na_4Ge_2Se_6$[4] and **(c)** $Na_4Si_2O_6$[27] from different viewing directions. The viewing direction is given with coordinate systems at the top of each column. All chains are crystallographically equivalent. Orange tetrahedra chains in **(a)** and **(b)** represent a different orientation of the chain compared to the blue/ green ones. The orientation is specified by the orientation of the longest *Tt*-Se distances in the *Tt*Se_4-tetrahedra. Na atoms are omitted for clarity.

4.4.4 Impedance Spectroscopy

Impedance spectroscopy was performed to check for ion mobility in $Na_4Si_2Se_6$-*oP*48. Impedance measurements of the other polymorph, $Na_4Si_2Se_6$-*tP*24, were not possible because the phase transition had already started during fabrication of the pellets. Therefore, only the high pressure modification was investigated for ionic conductivity. $Na_4Si_2Se_6$-*oP*48 shows ionic conductivity in the entire investigated temperature range from 50 °C to 200 °C (Figure 4.7). The specific conductivity is $\sigma_{spec} = 1.4 \times 10^{-8}\,\mathrm{S\,cm^{-1}}$ at 50 °C and $\sigma_{spec} = 6.8 \times 10^{-6}\,\mathrm{S\,cm^{-1}}$ at 200 °C. The activation energy of $E_A = 0.54(2)\,\mathrm{eV}$ was determined from the slope of the Arrhenius plot. $Na_4Si_2Se_6$-*oP*48 shows a moderate ion conductivity which is slightly lower than the ionic conductivity determined for Na_4SiS_4 ($1.64 \times 10^{-7}\,\mathrm{S\,cm^{-1}}$ at 25 °C).[29] The activation energy is higher than that for Na_4SiS_4 (0.36 eV).

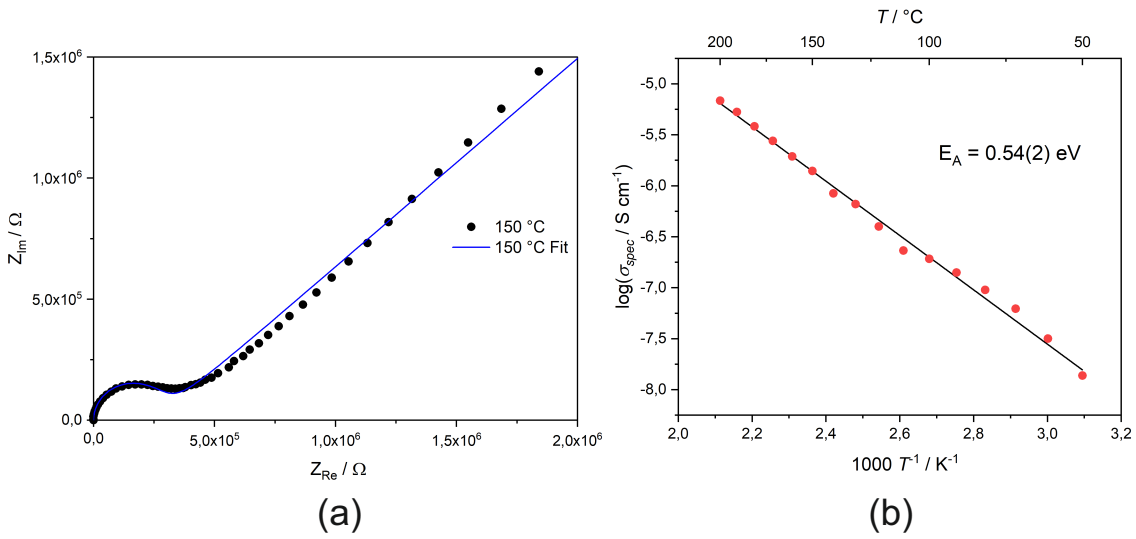

Figure 4.7 (a) measured frequency-dependent impedance (•) and fitted data and (b) temperature dependent total specific conductivity (•) and fitted data of $Na_4Si_2Se_6$-*oP*48 at 150 °C.

4.4.5 DFT modeling

DFT calculations were performed to compare the two polymorphs in terms of energy. Our functional of choice is the hybrid HSE06 since it usually reproduces experimental lattice parameters and electronic band gaps very well. We further tested five more functionals for both polymorphs in order to check for plausibility of the result since the calculated energetical difference of $Na_4Si_2Se_6$-$tP24$ and $Na_4Si_2Se_6$-$oP48$ is extremely small ($\Delta E = 3.4\,\mathrm{kJ\,mol^{-1}}$). Indeed, three of the applied functionals reveal a different order in energy (Table B.11). Calculations with PBE, PBE0 and HSE06 functionals result in $Na_4Si_2Se_6$-$tP24$ as more stable modification at 0 K, whereas calculations with PBEsol, PBE-D3 and LDA describe $Na_4Si_2Se_6$-$oP48$ to be energetically prefered. The rather small energy difference is predicted by each of the chosen functionals, which makes a clear statement of the energetic situation difficult. This is also confirmed by calculation of the electrostatic contributions to the lattice energies using MAPLE.[31] The two polymorphs do not differ in their lattice energy ($\Delta E = 5 \times 10^{-3}\,\mathrm{J\,mol^{-1}}$).
The smallest deviation of experimental and calculated lattice parameters is achieved by HSE06 and PBE0. This makes HSE06 a plausible choice for the calculation of the mechanical properties (bulk moduli) and transition pressure.
The calculated E-V-diagrams were fitted to the Birch-Murnaghan EOS in order to calculate the bulk moduli. The Birch-Murnaghan equation and the corresponding parameters were added to the Supporting Information. The corresponding H vs p diagrams reveal a positive value of the transformation pressure since $tP24$ is lower in energy. The calculated transition pressure is 0.3 GPa. The pressure applied in the hydraulic press during the production of the pellet for impedance spectroscopy was 0.1 GPa, which already led to the transformation of $tP24$ to $oP48$. This rather good qualitative description of the compressibility further justifies the choice of HSE06.

As mentioned before various structure types exist for this class of compounds. The anionic structure and coordination of Na is similar in $Na_4Ge_2S_6$ and $Na_4Si_2Se_6$-$oP48$ structure types. The only difference is the relative orientation of the chains. A similar bonding situation is found in form of *zweier* single chains ($Li_4Si_2O_6$, $Na_4Ge_2S_6$, $Li_4Sn_2Se_6$ and $Na_4Sn_2S_6$ structure types), *sechser* single chains ($Na_{12}Sn_6Se_{18}$ structure type) and *dreier* ring ($K_6Si_3O_9$ structure type). The different types and arrangements of corner-sharing tetrahedra can be compared energetically by DFT modeling of the structure types as listed in Table 4.4. Unit cells of all mentioned structure types can be found in Figures B.6 - B.11. The calculated E-V-curves are shown in Figure 4.9. $Na_4Si_2Se_6$ in the tetrag-

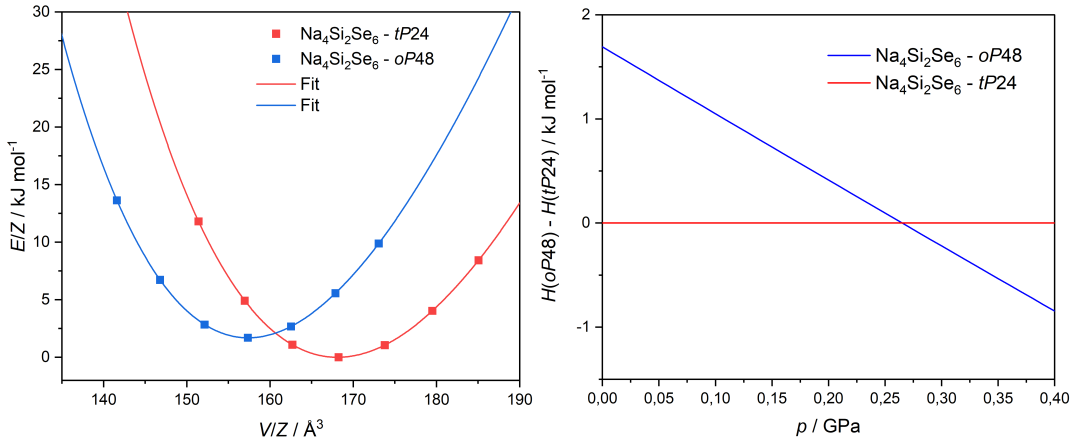

Figure 4.8 calculated E-V-curves with fit and ΔH-p-curves for both polymorphs of $Na_4Si_2Se_6$

onal modification (high temperature modification) is the most stable one. $Na_4Si_2Se_6$ in the $Na_4Si_2Se_6$-*oP*48 and $Na_4Ge_2S_6$ structure types are nearly identical in energy (ΔE = 0.3 kJ mol^{-1}). This is in line with the expectation because the structures differ only in the arrangement of the tetrahedra chains and the Na coordination is similar. The $Li_4Si_2O_6$, $Na_{12}Sn_6Se_{18}$ and $Li_4Sn_2Se_6$[21] structure types, all with *zweier* single chains, are 33.7 kJ mol^{-1}, 40.0 kJ mol^{-1} and 57.0 kJ mol^{-1} higher in energy. The rather large energetic difference of those structure types makes them an unlikely scenario for $Na_4Si_2Se_6$. $Na_4Si_2Se_6$ in the $K_6Si_3O_9$-structure type[16] (tricyclosilicate) is disfavored by 23.2 kJ mol^{-1} in energy. Concluding from DFT calculations, the existence of a metastable cyclotriselenidosilicate similar to $K_6Si_3O_9$ seems possible.

It is conceivable that polymorphism similar to $Na_4Si_2Se_6$ is also possible for compounds containing heavier tetrels (T = Ge, Sn). To substantiate this assumption DFT calculations for compounds with compositions $Na_4Ge_2Se_6$ and $Na_4Sn_2Se_6$ were performed. Both were calculated assuming different structure types: $Na_4Ge_2S_6$,[4] which is experimentally obtained for $Na_4Ge_2Se_6$ and $Na_4Sn_2Se_6$, $Na_{12}Sn_6Se_{18}$[20] which is only known for the tin compound, and the two new structure types $Na_4Si_2Se_6$-*tP*24 and $Na_4Si_2Se_6$-*oP*48. The results are listed in Table 4.5. Energies are given relative to the $Na_4Ge_2S_6$ structure type. In both cases the structure types containing *zweier* single chains are relatively close in energy. This is in line with the expectations, as the crystal structures are similar. Thus, we predict the *tP*24 structure type for $Na_4Ge_2Se_6$ (ΔE_{rel} = 8.6 kJ mol^{-1}), $Na_4Ge_2Se_6$-*oP*48 and$Na_4Sn_2Se_6$-*oP*48. In the case of $Na_4Sn_2Se_6$ the *oP*48 structure type could be realized by high pressure, starting from $Na_{12}Sn_6Se_{18}$. Edge-sharing $T_2Se_6^{4-}$-dimers which

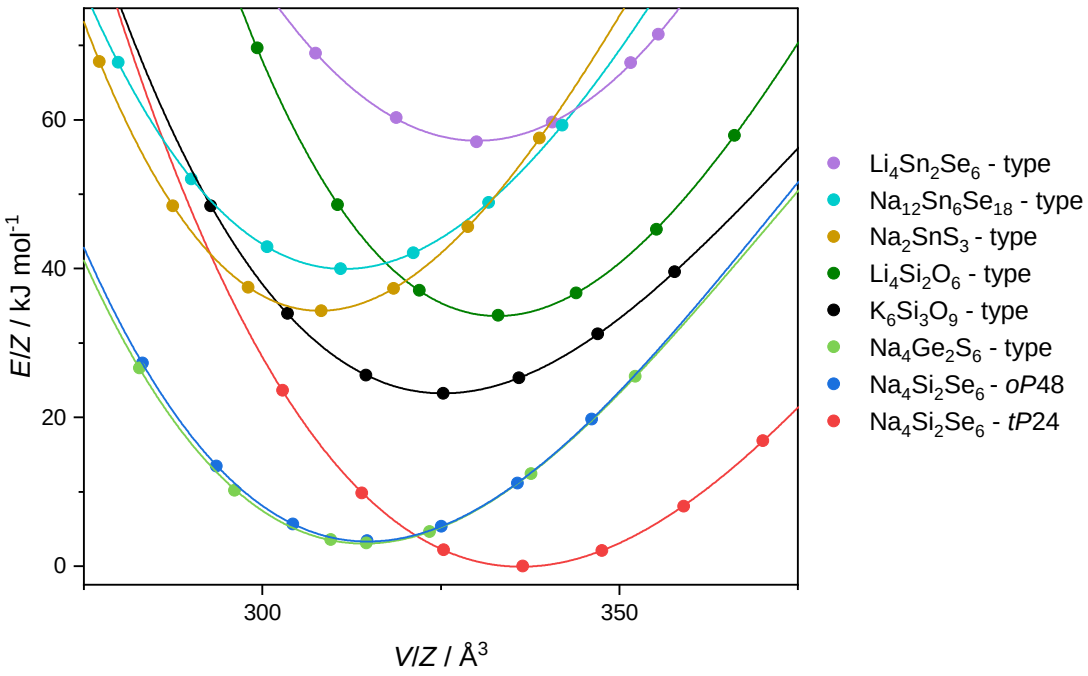

Figure 4.9 calculated E-V-curves for $Na_4Si_2Se_6$ in experimental and hypothetical structure types.

are realized for $Na_4Si_2Se_6$ become less stable in the Na compounds with increasing atomic number of the tetrel.

Table 4.4 experimental and optimized lattice parameters and energies ΔE calculated for hypothetic $Na_4Si_2Se_6$ assuming different structure types. ΔE is given relative to $Na_4Si_2Se_6$-*tP*24.

structure type	source	a / Å	b / Å	c / Å	β / °	V/Z / Å^3	$\Delta E/Z$ / kJ mol^{-1}
*tP*24	exp	7.2793(2)		12.4960(4)		165.54(3)	
	calc	7.324		12.547		336.49	0
*oP*48	exp	12.9276(1)	15.9323(1)	6.0349(1)		155.38(2)	
	calc	13.060	16.011	6.020		314.70	3.4
$Na_4Ge_2S_6$	calc	7.116	15.995	6.028	113.5	314.56	3.1
$K_{12}Si_3O_{18}$	calc	7.317	15.325	18.443	109.3	325.37	23.2
$Li_4Si_2O_6$	calc	13.580	8.044	6.097		333.01	33.7
Na_2SnS_3	calc	7.694	11.555	6.934		308.24	34.3
$Na_{12}Sn_6Se_{18}$	calc	13.708	22.450	12.128		310.95	40.0
$Li_4Sn_2Se_6$	calc	13.494	7.565	7.471	120.1	330.03	57.0

Band structure calculation

Band structures and DOS were calculated for both polymorphs of $Na_4Si_2Se_6$ (Figures 4.10 and B.3). $Na_4Si_2Se_6$-*tP*24 exhibits an indirect band gap of 3.8 eV, whereas direct transitions ($E_G = 3.8$ eV) are possible in the band structure of $Na_4Si_2Se_6$-*oP*48. A similar size of the band gap is expected due to a similar stability, as revealed by DFT modeling of both polymorphs. Standard DFT functionals (LDA and GGA) tend to underestimate band gaps. This problem can be overcome by applying a Fock exchange containing hybrid functional like HSE06, which usually reproduces experimentally determined optical band gaps very well.[43] Because of similar band gaps, $Na_4Si_2Se_6$-*tP*24 and $Na_4Si_2Se_6$-*oP*48 are expected to have the same color. Single crystals of $Na_4Si_2Se_6$-*tP*24 are yellow, whereas the powder of $Na_4Si_2Se_6$-*oP*48 is light grey. This might be due to particle size effects or a slight contamination by the graphite coating of the silica ampoules.

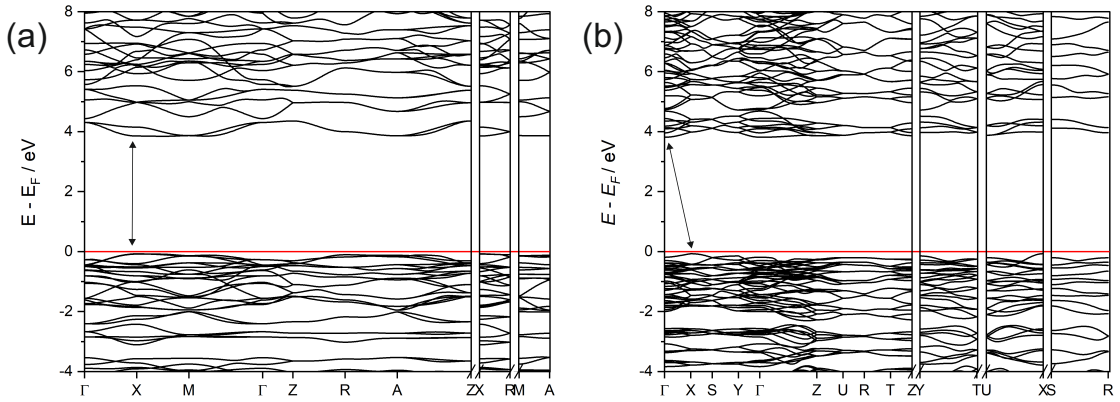

Figure 4.10 (a) calculated band structures of $Na_4Si_2Se_6$-*tP*24 and (b) $Na_4Si_2Se_6$-*oP*48. Black arrows are drawn to highlight the different types of band gaps.

Table 4.5 calculated energies of experimentally observed (written in bold) and hypothetical compounds with the compositions $Na_4Ge_2Se_6$ and $Na_4Sn_2Se_6$. Energies are given relative to the compound adopting the $Na_4Ge_2S_6$ structure type.

	$Na_4Ge_2Se_6$		$Na_4Sn_2Se_6$	
structure type	$\Delta E_{rel}/Z$ / kJ mol^{-1}	V/Z /Å^3	$\Delta E_{rel}/Z$ / kJ mol^{-1}	V/Z / Å^3
$Na_4Ge_2S_6$[4]	**0**	322.95	**0**	331.24
$Na_4Si_2Se_6$-*oP*48	0.2	323.41	3.9	333.20
$Na_{12}Sn_6Se_{18}$[20]	17.8	323.27	**-11.8**	347.49
$Na_4Si_2Se_6$-*tP*24	8.6	346.50	55.4	366.79

4.5 Conclusion

We report on the synthesis and characterization of two polymorphs of the new compound $Na_4Si_2Se_6$. The high temperature polymorph $Na_4Si_2Se_6$–*tP*24 crystallizes in a new structure type and can be synthesized via ball-milling and also directly from the elements. It represents a new structure type with edge-sharing $Si_2Se_6^{4-}$ tetrahedra dimers. The high pressure polymorph $Na_4Si_2Se_6$–*oP*48 also crystallizes as a new structure type. It consists of the same *zweier* single chains $^1_\infty[Si_2Se_6]^{4-}$ as present in the Ge compound $Na_4Ge_2Se_6$ but arranged in an antiparallel manner. A two step synthesis process includes ball-milling followed by annealing of the resulting reaction mixture. During ball-milling Na_2Se_4 is formed which is crucial for the formation of this polymorphic modification. The high and the low temperature modification form at different annealing temperatures. Impedance spectroscopy reveals moderate ionic conductivity for $Na_4Si_2Se_6$-*oP*48 (σ_{spec} =

$1.4 \times 10^{-8}\,\mathrm{S\,cm^{-1}}$ at 50 °C). DFT calculations reveal that both polymorphs are very close in energy, probed by different DFT functionals. A high-pressure phase transition from $Na_4Si_2Se_6$-*tP*24 to $Na_4Si_2Se_6$-*oP*48 is predicted at 0.3 GPa. This transition is observed in an hydraulic press at 0.1 GPa. Based on DFT modeling the existence of new modifications like a cyclosilicate seems plausible. Further, edge-sharing $T_2Se_6^{4-}$ dimers which are realized for $Na_4Si_2Se_6$ become less stable in the Na compounds with increasing atomic number of the tetrel. Synthesis and characterization of further sodium selenidosilicates are scheduled.

References

[1] Preishuber-Pflügl, H.; Klepp, K. O. *Z. Kristallogr. - New Cryst. Struct.* **2003**, *218*, 383–384.

[2] Eisenmann, B.; Hansa, J. *Z. Kristallogr. - Cryst. Mater.* **1993**, *203*, 295–296.

[3] Eisenmann, B.; Hansa, J.; Schäfer, H. *Z. Anorg. Allg. Chem.* **1985**, *526*, 55–59.

[4] Eisenmann, B.; Hansa, J.; Schäfer, H. *Z. Naturforsch. B* **1985**, *40*, 450–457.

[5] Sheldrick, W. S.; Schaaf, B. *Z. Anorg. Allg. Chem.* **1994**, *620*, 1041–1045.

[6] Sheldrick, W. S.; Braunbeck, H. G. *Z. Naturforsch. B* **1989**, *44*, 851–852.

[7] Evenson, C. R.; Dorhout, P. K. *Z. Kristallogr. - New Cryst. Struct.* **2000**, *215*, 318–318.

[8] Eisenmann, B.; Hansa, J. *Z. Kristallogr. - Cryst. Mater.* **1993**, *203*, 299–300.

[9] Shoemaker, D. P.; Hu, Y.-J.; Chung, D. Y.; Halder, G. J.; Chupas, P. J.; Soderholm, L.; Mitchell, J.; Kanatzidis, M. G. *Proc. Natl. Acad. Sci.* **2014**, *111*, 10922–10927.

[10] Eisenmann, B.; Hansa, J. *Z. Kristallogr. - Cryst. Mater.* **1993**, *203*, 301–302.

[11] Kolb, A.; Gollackner, M.; Klepp, K. O. *Z. Kristallogr. - New Cryst. Struct.* **2004**, *219*, 393–394.

[12] Preishuber-Pflügl, H.; Klepp, K. O. *Z. Kristallogr. - New Cryst. Struct.* **2003**, *218*, 387–388.

[13] Klepp, K. O.; Fabian, F. *Z. Kristallogr. - New Cryst. Struct.* **1997**, *212*, 302–302.

[14] Feldmann, C.; von Schnering, H. G.; Grin, Y. *Z. Kristallogr. - New Cryst. Struct.* **1998**, *213*, 482–482.

[15] Van Almsick, T.; Sheldrick, W. S. *Z. Anorg. Allg. Chem.* **2005**, *631*, 1746–1748.

[16] Werthmann, R. et al. *Rev. Chim. Minér.* **1981**, *18*, 593–607.

[17] Tournoux, M. *Annales de chimie* **1964**, *9*, 579–600.

[18] Lang, G. *Z. Anorg. Allg. Chem.* **1966**, *348*, 246–256.

[19] Benkada, A.; Hartmann, F.; Poschmann, M.; Indris, S.; Lühmann, H.; Bensch, W. *Eur. J. Inorg. Chem.* **2023**, *26*, e202200687.

[20] Eisenmann, B.; Hansa, J. *Z. Kristallogr. - Cryst. Mater.* **1993**, *203*, 291–292.

[21] Kaib, T.; Bron, P.; Haddadpour, S.; Mayrhofer, L.; Pastewka, L.; Järvi, T. T.; Moseler, M.; Roling, B.; Dehnen, S. *Chem. Mater.* **2013**, *25*, 2961–2969.

[22] Seemann, H. *Acta Crystallogr.* **1956**, *9*, 251–252.

[23] Halwax, E.; Völlenkle, H. *Z. Kristallogr. - Cryst. Mater.* **1984**, *169*, 63–72.

[24] Liebau, F., *Structural chemistry of silicates: structure, bonding and classification*; Springer: 1985.

[25] Hahn, H.; Theune, U. *Naturwissenschaften* **1957**, *44*, 33–33.

[26] Ahn, B. T.; Huggins, R. A. *Mater. Res. Bull.* **1989**, *24*, 889–897.

[27] Grund, A.; Pizy, M. *Acta Crystallogr.* **1952**, *5*, 837–840.

[28] Ginetti, Y. *Bull. Soc. Chim. Belg.* **1954**, *63*, 460–469.

[29] Harm, S.; Hatz, A.-K.; Schneider, C.; Hoefer, C.; Hoch, C.; Lotsch, B. V. *Front. Chem.* **2020**, *8*, 90.

[30] Gao, L.; Bian, G.; Yang, Y.; Zhang, B.; Wu, X.; Wu, K. *New J. Chem.* **2021**, *45*, 12362–12366.

[31] Hoppe, R. *Angew. Chem. - Int. Ed.* **1966**, *5*, 95–106.

[32] Range, K.-J.; Leeb, R. *Z. Naturforsch. B* **1975**, *30*, 889–895.

[33] CrysAlisPro (V42); Rigaku Oxford Diffraction Ltd, 2019.

[34] Palatinus, L.; Chapuis, G. *J. Appl. Crystallogr.* **2007**, *40*, 786–790.

[35] Petříček, V.; Dušek, M.; Palatinus, L. *Z. Kristallogr. - Cryst. Mater.* **2014**, *229*, 345–352.

[36] WinXPow, Version 3.10; STOE & Cie GmbH, STOE & Cie GmbH: Darmstadt, 2016.

[37] Zahner-Elektrik Zahner Analysis, Version 2.9.2 RC 1; I. Zahner-Schiller GmbH & Co. KG, Kronach, 2018.

[38] Dovesi, R.; Erba, A.; Orlando, R.; Zicovich-Wilson, C. M.; Civalleri, B.; Maschio, L.; Rérat, M.; Casassa, S.; Baima, J.; Salustro, S.; Kirtman, B. *WIREs Comput. Mol. Sci.* **2018**, *8*, e1360.

[39] Dovesi, R. et al. CRYSTAL17 User's Manual; University of Torino, 2017.

[40] Sophia, G.; Baranek, P.; Sarrazin, C.; Rerat, M.; Dovesi, R., `https://www.crystal.unito.it/Basis_Sets/sodium.html`, Accessed: 2023-03-06, 2014.

[41] Porter, A. R.; Towler, M. D.; Needs, R. J. *Phys. Rev. B* **1999**, *60*, 13534–13546.

[42] Towler, M. D.; Zicovich-Wilson, C., `https://vallico.net/mike_towler/crystal.html`, Accessed: 2023-03-06, 1995.

[43] Heyd, J.; Peralta, J. E.; Scuseria, G. E.; Martin, R. L. *J. Chem. Phys.* **2005**, *123*, 174101.

[44] Vosko, S. H.; Wilk, L.; Nusair, M. *Can. J. Phys.* **1980**, *58*, 1200–1211.

[45] Perdew, J. P.; Burke, K.; Ernzerhof, M. *Phys. Rev. Lett.* **1996**, *77*, 3865–3868.

[46] Grimme, S. *J. Comput. Chem.* **2006**, *27*, 1787–1799.

[47] Grimme, S.; Antony, J.; Ehrlich, S.; Krieg, H. *J. Chem. Phys.* **2010**, *132*, 154104.

[48] Perdew, J. P.; Ruzsinszky, A.; Csonka, G. I.; Vydrov, O. A.; Scuseria, G. E.; Constantin, L. A.; Zhou, X.; Burke, K. *Phys. Rev. Lett.* **2008**, *100*, 136406.

[49] Adamo, C.; Barone, V. *J. Chem. Phys.* **1999**, *110*, 6158–6170.

[50] Becke, A. D. *Phys. Rev. A* **1988**, *38*, 3098–3100.

[51] Heyd, J.; Scuseria, G. E.; Ernzerhof, M. *J. Chem. Phys.* **2003**, *118*, 8207–8215.

[52] Murnaghan, F. D. *Amer. J. Math.* **1937**, *59*, 235–260.

[53] Murnaghan, F. D. *Proc. Natl. Acad. Sci.* **1944**, *30*, 244–247.

[54] Birch, F. *Phys. Rev.* **1947**, *71*, 809–824.

[55] Setyawan, W.; Curtarolo, S. *Comput. Mater. Sci.* **2010**, *49*, 299–312.

[56] Zintl, E.; Harder, A.; Dauth, B. *Z. Elektrochem. Angew. Phys. Chem.* **1934**, *40*, 588–593.

[57] Eulenberger, G. *Monatsh. Chem.* **1982**, *113*, 859–867.

[58] Shannon, R. D. *Acta Crystallogr. A* **1976**, *32*, 751–767.

[59] Schindler, L. V.; Becker, A.; Wieckhusen, M.; Klüner, T.; Wickleder, M. S. *Angew. Chem. - Int. Ed.* **2016**, *55*, 16165–16167.

5 Enhanced sodium ion mobility in sodium tellurosilicates and crystal structures of Na_4SiTe_4 and $Na_{10}Si_2Te_9$ with isolated $[SiTe_4]^{4-}$ tetrahedra and isolated Te^{2-} anions

5.1 Preface and Abstract

This chapter is reprinted and adapted from *Dalton Transactions* **2024**, DOI: 10.1039/d4dt01717j. Several people contributed to this work:

- Franziska Kamm performed the experimental work and the DFT calculations and wrote and improved the manuscript.
- Dr. Florian Pielnhofer supervised the DFT calculations, contributed with discussions and improved the manuscript.
- Dr. Marc Schlosser performed the EDX measurement, contributed with discussions and improved the manuscript.
- Prof. Dr. Arno Pfitzner contributed with discussions, supervised the experimental work and corrected and improved the manuscript.

Abstract

The sodium tellurosilicates Na_4SiTe_4, $Na_{10}Si_2Te_9$, $Na_6Si_2Te_6$ and $Na_8Si_4Te_{10}$ were synthesized by ball milling and subsequent high temperature solid state reactions and analysed by electrochemical impedance spectroscopy. All compounds show moderate to remarkable sodium ion conductivity. The crystal structures of the novel materials Na_4SiTe_4 and $Na_{10}Si_2Te_9$ were determined by X-ray diffraction. Both compounds represent new structure types with isolated $SiTe_4$ tetrahedra. The crystal structure of $Na_{10}Si_2Te_9$ exhibits a single telluride anion besides two $SiTe_4$ tetrahedra. Na_4SiTe_4 crystallizes in the cubic space group $Pa\bar{3}$ (No. 205) with the lattice parameters $a = 13.0312(1)$

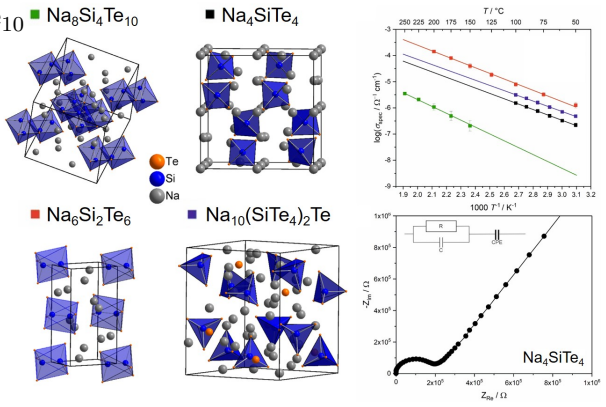

Å and $V = 2212.84(2)$ Å^3. $Na_{10}Si_2Te_9$ crystallizes in the orthorhombic space group $Pna2_1$ (No. 33) with lattice parameters $a = 12.8235(7)$ Å, $b = 14.8398(8)$ Å, $c = 12.9530(7)$ Å and $V = 2464.9(2)$ Å^3. The presence of two different anionic units makes this compound stand out from other alkali chalcogenotetrelates. The electronic structure of all compounds was investigated by density functional theory, revealing their semiconducting behaviour.

5.2 Introduction

The only two sodium tellurosilicates reported in literature were described by Schäfer et al. in the early 1980s. Both compounds are hexatellurohypodisilicates with ethane-like $[Si_2Te_6]^{2-}$ anions.[1,2] In $Na_6Si_2Te_6$, this anion is present as isolated $[Si_2Te_6]^{2-}$ anion whereas in $Na_8Si_4Te_{10}$ two of the octahedrally coordinated Si-dumbbells are condensed to form $[Si_4Te_{10}]^{8-}$ anions (Figure 5.1).

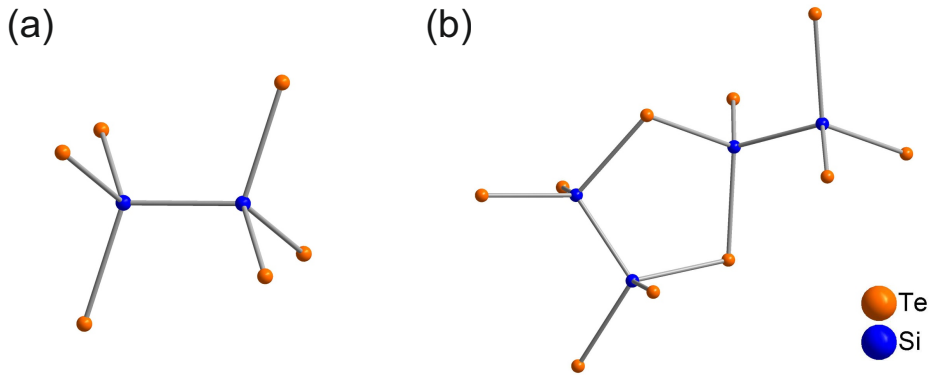

Figure 5.1 Anionic units in sodium tellurosilicates known from literature: (a) $[Si_2Te_6]^{2-}$ in $Na_6Si_2Te_6$[1] and (b) $[Si_4Te_{10}]^{8-}$ in $Na_8Si_4Te_{10}$.[2]

For the Na-Si-Se system, a larger variety of anionic structures are known. All known compounds contain $SiSe_4$ tetrahedra which are connected in different ways. Isolated tetrahedra were found in Na_4SiSe_4[3] and corner sharing tetrahedra were observed in $Na_6Si_2Se_7$[4] and $Na_4Si_2Se_6$.[5] $Na_6Si_2Se_7$ shows tetrahedra dimers $[Si_2Se_7]^{6-}$ whereas tetrahedra in $Na_4Si_2Se_6$ form infinite chains. Edge-sharing tetrahedra dimers were found in the second polymorph of $Na_4Si_2Se_6$. In $Na_6Si_2Se_8$, two tetrahedra are connected by a Se-Se bond.[6]

New and also well established sodium selenosilicates were accessible by using mechanochemical synthesis.[5] Comparing the chemical differences in sodium selenosilicate- and tellurosil-

icate compounds made us curious to check whether the oxidation power of Te is sufficient to oxidize Si to the state +IV. To date, only few alkali tellurosilicates with $SiTe_4$ tetrahedra building units are known.[7–9] Isolated tetrahedra were solely found in Cs_4SiTe_4.[8] Using mechanochemical synthesis, we obtained two new sodium tellurosilicates: Na_4SiTe_4, which contains isolated $[SiTe_4]^{4-}$ tetrahedra as main structural motif, and $Na_{10}Si_2Te_9$, containing isolated $[SiTe_4]^{4-}$ tetrahedra as well as isolated Te^{2-} anions. More precisely, it can be written as $Na_{10}(SiTe_4)_2Te$.

The growing interest in all-solid-state batteries (ASSBs) as future battery systems makes it obvious to examine compounds with a high sodium content regarding their ionic conductivity. Even if the application of rare elements like tellurium in battery systems is rather unlikely, it is important to expand the knowledge of compounds with mobile Na ions to develop suitable solid electrolytes for commercial ASSBs. High sodium ion conductivities were found in sodium thiophosphates, e.g. Na_3PS_4.[10,11] Substitution of S by the higher homologue Se in Na_3PSe_4 leads to a higher ionic conductivity.[12–14] A corresponding Te compound is yet unknown which is not surprising due to the strong tendency of P and Te to avoid covalent bonding.

This trend is not that obvious when the central atom of the complex anions is changed from P to Si. The sodium ion conductivity for Na_4SiS_4 ($\sigma_{spec} = 1.64 \times 10^{-7}\,\Omega^{-1}\,cm^{-1}$ at 25 °C)[15] and Na_4SiSe_4-*oP*36 ($\sigma_{spec} = 1.0 \times 10^{-7}\,\Omega^{-1}\,cm^{-1}$ at 75 °C)[16] are in the same order of magnitude. It should be noted that comparing literature data on ionic conductivities shows a variation of at least a factor of 10 for identical compounds.

Herein, we report on the sodium ion conductivities of two literature known compounds, $Na_6Si_2Te_6$[1] and $Na_8Si_4Te_{10}$,[2] and two hitherto unknown compounds. The crystal structures of Na_4SiTe_4 and $Na_{10}Si_2Te_9$ were investigated using powder X-ray diffraction and single crystal X-ray diffraction, respectively. The electronic structure of all title compounds was studied by density functional theory (DFT).

5.3 Experimental Section

5.3.1 Synthesis

All syntheses and sample manipulations were performed under Ar atmosphere.

Powder samples of all title compounds were synthesized in a two step procedure from the elements. At first, a homogeneous reaction mixture was prepared with sodium (Sigma-Aldrich, 99.8 %), silicon (Siltronic, silicon wafer) and tellurium (ChemPur, 99.999 %) in

the respective stoichiometric ratio using a Fritsch Pulverisette 7 premium line ball mill with 25 mL zirconia grinding bowls and 10 zirconia grinding balls with a diameter of 10 mm. In each case, 12 milling cycles with a top speed of 600 rpm for 3 min followed by a 5 min break were performed. In the second step, 0.3 g of this mixture were transferred to silica ampoules, which were evacuated, flame sealed and transferred to tube furnaces. To synthesize $\mathbf{Na_4SiTe_4}$, the reaction mixture was heated to 350 °C for 7 days. Heating and cooling rate were both set to 1 °C min^{-1}. For the synthesis of $\mathbf{Na_{10}Si_2Te_9}$, the corresponding reaction mixture was heated to 400 °C with a heating rate of 1 °C min^{-1}. After 7 days, the ampoule was quenched in air.
In contrast to the synthesis described in literature also $Na_8Si_4Te_{10}$ and $Na_6Si_2Te_6$ were prepared following the same mechanochemical synthesis procedure. The high temperature synthesis reported in the literature was optimized for the preparation of single crystals whereas our two-step synthesis procedure was optimized for powder samples. For $\mathbf{Na_8Si_4Te_{10}}$, the ball-milled reaction mixture was heated to 600 °C for 5 days. To prevent reactions with the glass, a silica ampoule with graphite coating from pyrolyzed acetone was used. Both heating and cooling rate were set to 1 °C min^{-1}. For $\mathbf{Na_6Si_2Te_6}$, the corresponding reaction mixture was annealed at 450 °C for 3 days. Both heating and cooling rate were set to 1 °C min^{-1}.
Crystals of $Na_{10}Si_2Te_9$ were obtained directly from the elements in a 10:2:9 ratio. Si and Te were homogenized in an agate mortar. The mixture was transferred to a silica ampoule with graphite coating from pyrolyzed acetone and covered with pieces of Na. The ampoule was then evacuated, flame sealed and transferred to a tube furnace. The mixture was heated to 350 °C for 5 days. As only very small crystals could be detected, the mixture was heated to 350 °C for further 14 days until the crystal size was appropriate for single crystal diffraction. Heating and cooling rates were set to 1 °C min^{-1}.

5.3.2 Temperature dependent Powder X-ray Diffraction (PXRD)

Finely ground samples were filled in quartz capillaries ($\varnothing$ = 0.3 mm) that were sealed subsequently. The capillaries were mounted on a STOE STADI P diffractometer (Stoe & Cie) equipped with a Mythen 1K detector and measured using MoKα_1 radiation (λ = 0.709 30 Å). The high temperature diffraction experiment was performed in a graphite furnace which was mounted on the diffractometer. For the investigation of low temperatures (−150 °C - 25 °C) the sample was cooled with a Oxford Cryosystems Cryostream 700.

For raw data handling the *WinXPow*[17] software package (Stoe & Cie) was used. Profile fitting, structure solution and Rietveld refinements were performed using *Jana2006*[18] and the implemented *Superflip*[19] algorithm.

5.3.3 Single crystal X-ray diffraction

Suitable crystals of $Na_{10}Si_2Te_9$ were selected in an Ar filled glovebox and transferred to mineral oil. The oil covered sample can be handled in air. Diffraction experiments were performed on a Rigaku XtaLAB Synergy R, DW System with a HyPix-Arc 150 detector. MoKα radiation (λ=0.710 73 Å) was used for all measurements. The cell determination, data reduction and absorption correction was done with the CrysAlis Pro software.[20] Structure solution and refinement were performed using *Jana2006*[18] and the implemented *Superflip*[19] algorithm.

5.3.4 Impedance Spectroscopy

For impedance measurements a *Zahner Zennium* impedance analyzer coupled with an home-made furnace was used. The whole set up is installed in an Ar filled glovebox to prevent reactions with air or moisture during the measurement. Measurements at temperatures below 50 °C are not possible due to this set-up. Powder samples of all compounds were cold-pressed ($\varnothing = 8$ mm) and contacted with gold electrodes. Pellets had a density of 91 % (Na_4SiTe_4 and $Na_{10}Si_2Te_9$), 94 % ($Na_6Si_2Te_6$) and 83 % ($Na_8Si_4Te_{10}$) with respect to the crystallographic density. For Na_4SiTe_4 and $Na_{10}Si_2Te_9$, two measurement cycles from 50 °C – 100 °C in steps of 10 °C in the frequency range from 1 MHz to 100 mHz were performed. The samples loose tellurium at higher temperatures. $Na_6Si_2Te_6$ was investigated in the temperature range of 50 °C to 200 °C in the same frequency range. $Na_8Si_4Te_{10}$ was investigated in the temperature range from 50 °C to 250 °C in a frequency range of 100 kHz to 100 mHz. As ionic conductivity can only be safely detected from 150 °C the temperature range of 150 °C to 250 °C was taken into account solely. An excitation voltage of 50 mV was used for all measurements. The *Zahner Analysis*[21] software was used for data processing and fitting. Nyquist plots were fitted by different equivalent circuits (see Figure C.11). The so determined R was used to calculate the overall resistance of the sample. R and the resulting σ_{spec} were corrected by a factor of $\frac{\rho_{calc}}{\rho_{meas}}$. Activation energies E_A were determined from the slope of the Arrhenius plots.

5.3.5 Energy Dispersive X-ray Spectroscopy

The composition of crystals of $Na_{10}Si_2Te_9$ was analyzed by a Zeiss EVO MA 15 scanning electron microscope (SEM, $LabB_6$ cathode) coupled with a Bruker Quantax 200 - Z30 (30 mm^2, Xflash 630) energy dispersive X-ray spectroscopy (EDX) unit. The microscope was controlled with the Zeiss SmartSEM software (version 6.02). For the EDX spectra the Bruker Quantax ESPRIT software (Version 2.1) was used. The crystals were transferred to a specimen holder in a Ar filled glovebox and moved to the SEM in a hermetically sealed box.

5.3.6 DFT modeling

All quantum chemical calculations were performed using the CRYSTAL23 code.[22,23] Basis sets for Na,[24] Si[25] and Te[26] were taken from the literature. The outer shells of all basis sets were additionally adjusted to minimize the calculated energy. Full structure optimizations were performed with the hybrid functional HSE06[27,28] using a k-mesh sampling of 6 × 6 × 6. The tolerances for coulomb and exchange sums were increased to 10^{-7} a.u., 10^{-9} a.u. and 10^{-30} a.u. The convergence criterion for the energy was set to 10^{-8} a.u. Geometries were optimized using experimentally determined structure data as starting point. The k paths for electronic structure calculations were determined using the SeeK-path online tool.[29]

5.4 Results and Discussion

5.4.1 Crystal Structure of Na_4SiTe_4

Na_4SiTe_4 crystallizes in the cubic space group $Pa\bar{3}$ (no. 205) with the lattice parameters $a = 13.0312(1)$ Å and $V = 2212.84(2)$ Å^3 and eight formula units per unit cell. The structure was solved from a X-ray powder diffraction pattern using *Superflip* followed by Rietveld refinement (Figure 5.2).

Crystallographic data and structure determination details are listed in Table 5.1 and in the SI. The unit cell with isolated $[SiTe_4]^{4-}$ tetrahedra is shown in Figure 5.3a. The crystal structure is related to the rock salt structure type. Te^{2-} forms a distorted face-centered cubic (fcc) lattice with Na^+ in all octahedral voids. Additionally, 1/8 of the tetrahedral voids are occupied by Si^{4+}. This becomes easily obvious from a section of 1/8 of the unit cell, as shown in Figure 5.3b.

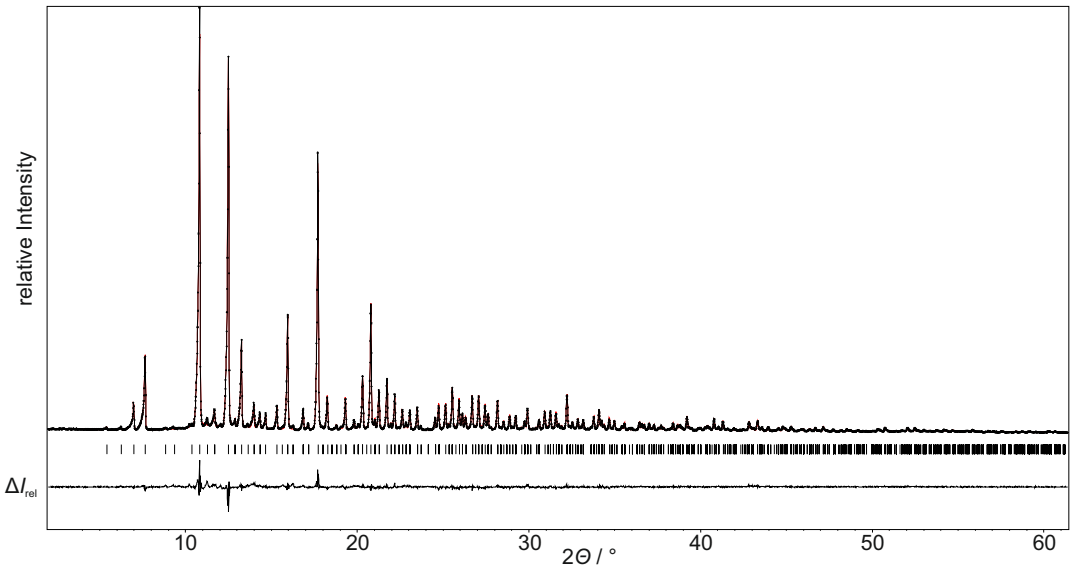

Figure 5.2 PXRD pattern of Na_4SiTe_4 with difference plot from Rietveld refinement, measured with MoKα1 radiation at room temperature.

Si occupies Wyckoff position 8*c* and is surrounded by 4 Te. A slightly distorted tetrahedron with Si-Te distances of 2.446(6) Å and 2.523(6) Å and angles of 109.2(2)° and 109.8(2)°. Sodium atoms occupy three different crystallographic positions (24*d*, 4*a*, 4*b*). Each Na is surrounded by 6 Te resulting in slightly distorted octahedral coordination. Bond lengths are within the typical range (d(Na1-Te) = 3.173(5) Å - 3.473(1) Å, d(Na2-Te) = 3.317(2) Å and d(Na3-Te) = 3.291(2) Å). The distances are within a narrower range compared to those found in $Na_6Si_2Te_6$ (d(Na-Te) = 3.085 Å - 3.526 Å).[1]

The crystal structure of Na_4SiTe_4 represents a new structure type. The lighter homologue Na_4SiSe_4 crystallizes in a similar way. It is also related to the NaCl structure type but differs in the arrangement of SiQ_4 tetrahedra. In Na_4SiSe_4 the Si atoms are arranged according to the homoatomic Cr_3Si structure type (A15 structure)[30] whereas Si atoms in Na_4SiTe_4 form a rhombohedron. These structural characteristics were also found in α-Li_8GeP_4 and β-Li_8GeP_4 where the $[GeP_4]^{8-}$ tetrahedra are arranged in a similar way.[31]

5.4.2 Crystal structure of $Na_{10}Si_2Te_9$

Diffraction experiments with several crystals of $Na_{10}Si_2Te_9$ were performed at room temperature as well as at lower temperatures. All data sets resulted in an identical, reasonable structure model. To substantiate the proposed crystal structure, the course of the struc-

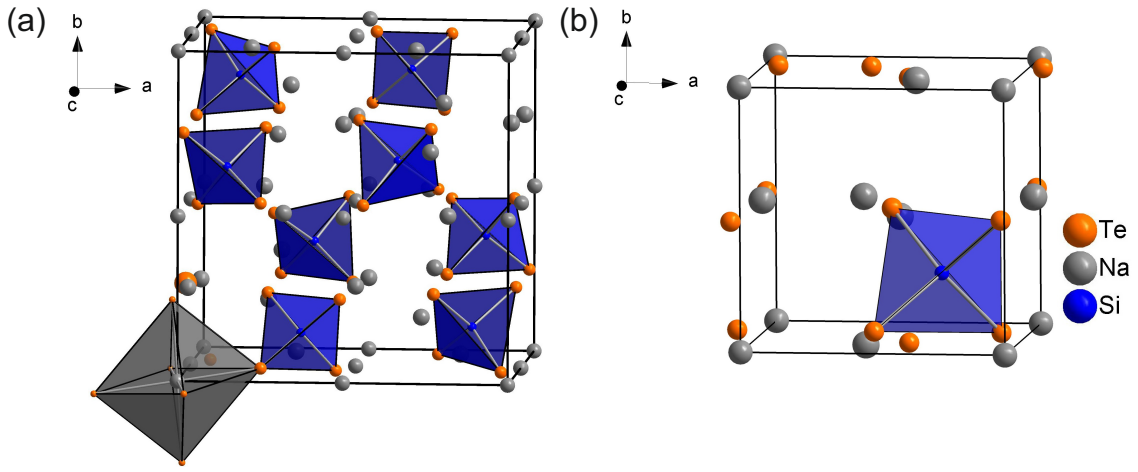

Figure 5.3 (a) Unit cell of Na_4SiTe_4 with isolated $SiTe_4$ tetrahedra. (b) 1/8 of the unit cell representing the structural relation to the rock salt structure type.

ture determination will be described for one of the measured crystals in the following.

The orthorhombic metric and reflection conditions as well as statistics for $E^2 - 1$ of the measured reflections lead to a centrosymmetric structure with space group *Pbcn* (no. 60). 99 % of the measured reflections can be indexed with two components with the same unit cell. The unit cells of the two components are slightly shifted towards each other and 95 % and 2 % of the reflections are separate. For structure solution and refinement only reflections from the first component are used. A structure model with both isolated $[SiTe_4]^{4-}$ tetrahedra and isolated Te^{2-} ions with the composition $Na_{10}Si_2Te_9$ or $Na_{10}(SiTe_4)_2Te$ was obtained from structure solution with direct methods using the *Superflip*[19] algorithm which is implemented in *Jana2006*.[18] Though the structure model seems reasonable from a chemical point of view, the structure refinements of the single crystal data were not entirely satisfactory. The resulting crystal structure exhibits high residual electron densities around Te with distances less than 1 Å as well as high R values (Table C.2). Additionally, one sodium position has to be splitted, which can be explained by too long distances to its tellurium neighbours.

Refinement as inversion twin in the space group $Pna2_1$ (no. 33), which is a subgroup of *Pbcn*, leads to lower, more reasonable R values (0.0437 compared to 0.0562) and all sodium positions can be resolved to fully occupied positions with coordination spheres as expected. The Flack parameter was refined to 0.51(3). Although a Flack parameter close to 0.5 can hint at inversion symmetry, we chose the non-centrosymmetric description to avoid the split sodium positions. The remaining residual electron density decreased

Table 5.1 Crystallographic data and structure determination details for Na_4SiTe_4 and $Na_{10}Si_2Te_9$. Note that the crystal structure of Na_4SiTe_4 was determined from powder data, whereas $Na_{10}Si_2Te_9$ was determined from single crystal data.

compound	Na_4SiTe_4	$Na_{10}Si_2Te_9$
space group	$Pa\bar{3}$ (no. 205)	$Pna2_1$ (no. 33)
formula weight / $g\,mol^{-1}$	630.4	1434.5
shape, color	powder, yellow	block, red
T / K	296	100.0(1)
a / Å	13.0312(1)	12.8235(7)
b / Å		14.8398(8)
c / Å		12.9530(7)
V / $Å^3$	2212.84(2)	2464.9(2)
Z	8	4
radiation	MoKα1	MoKα
wavelength λ / Å	0.70930	0.71073
profile R indexes	$R_P = 0.0422$, $R_{wP} = 0.0567$, $R_{exp} = 0.0326$	
goodness of fit	1.74	1.65
final R values	$R_1 = 0.0408$,	$R_1 = 0.0323$,
$[I>=3\sigma(I)]$	$wR_2 = 0.0469$	$wR_2 = 0.0662$
final R values	$R_1 = 0.0447$,	$R_1 = 0.0437$,
[all data]	$wR_2 = 0.0476$	$wR_2 = 0.0679$
$\Delta\rho_{min}$, $\Delta\rho_{max}$ / $eÅ^{-3}$	-1.36, 1.15	-4.93, 8.06
Flack parameter		0.51(3)

compared to the centrosymmetric solution. According to the difference Fourier map, the electron density peaks surround the Te positions (Figure C.5). This phenomenon of high displacement parameters is often observed in case of solid electrolytes, even for the non mobile ions, which is a hint for the high dynamic behaviour in such materials. A structure refinement with non-harmonic displacement parameters (Gram-Charlier) made these residues disappear but also increased the number of variables significantly. Nevertheless, the proposed crystal structure can be substantiated with X-ray powder diffraction at room temperature via Rietveld refinement. Because of the temperature difference of single crystal and powder diffraction experiment, the compound was checked for a possible phase transition in the temperature range from 20 °C to −150 °C by powder diffraction experiments. The linear decrease of the lattice parameters does not indicate any phase transition (Figure C.7). Further details to the structure determination can be found in

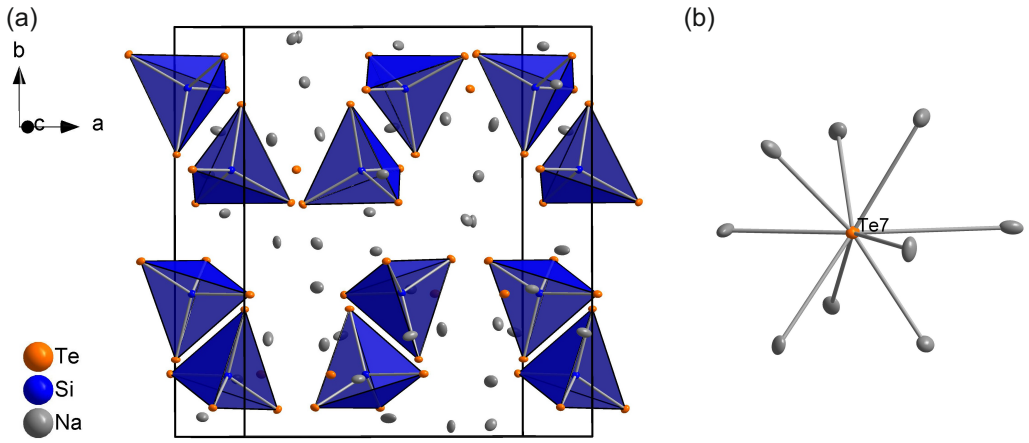

Figure 5.4 (a) Unit cell of $Na_{10}Si_2Te_9$ with isolated $SiTe_4$ tetrahedra. Na-Te bonds are omitted for clarity. (b) Discrete Te^{2-} anion with tricapped trigonal prismatic coordination environment by sodium.

the appendix.

$Na_{10}Si_2Te_9$ crystallizes in the space group $Pna2_1$ (No. 33) with lattice parameters a = 12.8235(7) Å, b = 14.8398(8) Å, c = 12.9530(7) Å and V = 2464.9(2) Å^3 at 100 K. There are four formula units per unit cell. The unit cell contains isolated $[SiTe_4]^{4-}$ tetrahedra as well as isolated Te^{2-} anions (see Figure 5.4a and b). To highlight the presence of the two different anionic units, the sum formula could also be given as $Na_{10}(SiTe_4)_2Te$.

The composition of single crystals of $Na_{10}Si_2Te_9$ was additionally confirmed by EDX (see Table C.4). The measured composition of 46.7 atom-% for Na, 10.6 atom-% for Si and 42.7 atom-% for Te is in accordance with the composition determined from X-ray diffraction (47.6 atom-% for Na, 9.5 atom-% for Si and 42.9 atom-% for Te).

The structure consists of 21 crystallographically independent sites. There are two crystallographically different Si position. Both Si are surrounded by 4 Te resulting in a tetrahedral coordination environment. The $[SiTe_4]^{4-}$ tetrahedra are slightly distorted with Si-Te distances of 2.493(2) Å to 2.526(2) Å and angles of 105.67(7)° to 112.16(7)°. The distances are very similar to the ones found in Na_4SiTe_4 (d(Si-Te) = 2.446(6) Å - 2.523(6) Å).

The coordination sphere of Te7 distinguishes this compound from other alkali tellurosilicates, as this atom does not form bonds to Si. The discrete Te^{2-} anions are coordinated by nine Na atoms resulting in a tricapped trigonal prismatic coordination environment (Figure 5.4b). Na-Te distances vary from 3.114(3) Å to 3.816(2) Å. In sodium telluride Na_2Te[32] distances are in the same order of magnitude (d(Na-Te) = 3.167 Å).

There are two different coordination environments observed for Na. Na1 to Na8 exhibit

Table 5.2 Optimized lattice parameters in comparison to experimentally determined parameters. The calculated cell volume V deviates by less than 1 %.

compound		a / Å	b / Å	c / Å	β / °	V / Å^3	dev. (V) / %
Na_4SiTe_4	exp	13.0312(1)				2212.84(2)	
	HSE06	12.9897				2191.77	-1.0
$Na_{10}Si_2Te_9$	exp	12.9790(2)	14.9308(2)	13.0670(1)		2532.21(5)	
	HSE06	13.0492	14.8605	13.0263		2526.0306	-0.2
$Na_6Si_2Te_6$	exp	8.7789(1)	12.7801(2)	8.8657(2)	119.749(2)	863.30(3)	
	HSE06	8.8409	12.8252	8.9175	120.613	870.20	0.8
$Na_8Si_4Te_{10}$	exp	14.0843(2)	12.8408(2)	14.9389(3)	92.323(2)	2699.54(9)	
	HSE06	14.1431	12.8131	15.0147	92.150	2719.02	0.7

a distorted octahedral coordination environment with Na-Te distances from 3.080(4) Å to 3.910(4) Å. Na9 and Na10 are surrounded by 5 Te resulting in strongly distorted trigonal bipyramidal coordination environment (d(Na-Te)= 3.061(3) Å - 3.461(2) Å). All Na positions are fully occupied. The coordination polyhedra with all distances are shown in Figure C.3.

Crystal structures with isolated Te^{2-} anions were not observed yet in the Na-Tt-Te system (Tt = Si, Ge, Sn, Pb). However, isolated chalcogenide anions Q^{2-} were found in different other crystal structures like in $Ba_7Sn_3Se_{13}$[33] or Ag_8SiTe_6.[34]

The high temperature behavior of $Na_{10}Si_2Te_9$ was examined with in situ high-temperature X-ray powder diffraction (Figure C.8). The compound is stable up to 500 °C and decomposes peritactically to $Na_6Si_2Te_6$ at higher temperature. Upon cooling, the reformation of $Na_{10}Si_2Te_9$ was observed.

5.4.3 Electronic Structure Calculations

The electronic structures of Na_4SiTe_4, $Na_{10}Si_2Te_9$, $Na_6Si_2Te_6$ and $Na_8Si_4Te_{10}$ were evaluated on the basis of DFT calculations. Geometries were optimized using experimentally determined structure data as the starting point. The calculated lattice parameters are in good agreement with those determined from X-ray powder data (Table 5.2). In general, the PBE based functional HSE leads to a good prediction of lattice parameters as it reduces the overestimation of PBE drastically.[26]

Electronic structure calculations reveal indirect band gaps of 2.81 eV for Na_4SiTe_4, 2.77 eV for $Na_6Si_2Te_6$ and 2.69 eV for $Na_8Si_4Te_{10}$. $Na_{10}Si_2Te_9$ exhibits a direct band gap of 2.29 eV. This is in line with the observed sample colors. Powder samples of Na_4SiTe_4 and $Na_6Si_2Te_6$

appear yellow, samples of $Na_{10}Si_2Te_9$ orange and $Na_8Si_4Te_{10}$ yellow to brown.

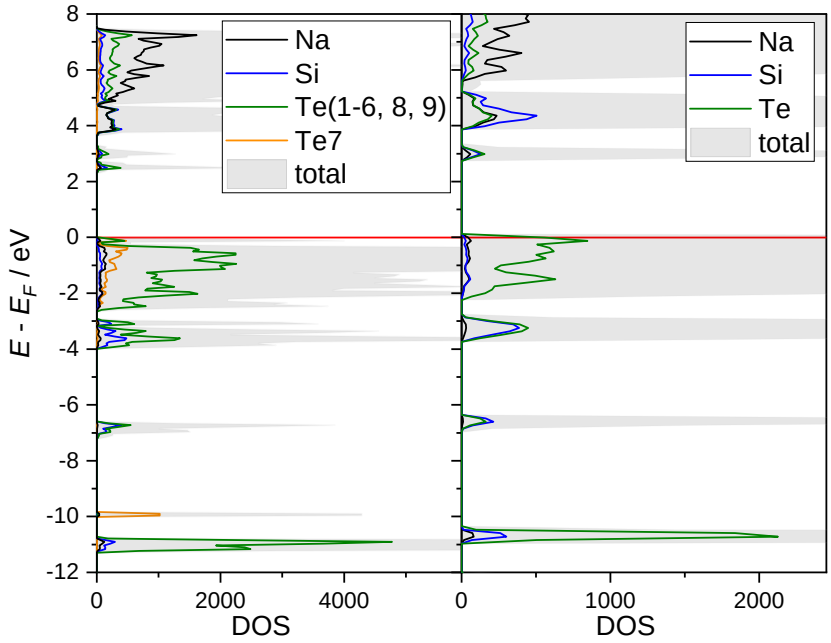

Figure 5.5 DFT calculated electronic DOS for $Na_{10}Si_2Te_9$ (left) and Na_4SiTe_4 (right). The horizontal line at 0 eV represents the Fermi level E_F. For $Na_{10}Si_2Te_9$, the DOS of Te7 (only surrounded by Na) and all other Te positions (surrounded by Na and Si) are shown separately.

The DOS for Na_4SiTe_4 and $Na_{10}Si_2Te_9$ are similar except for additional states at -10.8 eV to -11.2 eV for $Na_{10}Si_2Te_9$ which are attributable to the different coordination sphere of Te7 (Te^{2-} ion). In contrast, the other Te form covalent bonds in the tetrahedral tellurosilicate anions (Figure C.13). Orbital projected DOS calculations reveal mainly *s* character for the respective states. The Mulliken population analysis also prove the difference in the electronic bonding situation between the free telluride and the silicon bonded telluride. The free telluride exhibits a charge of -1.391 whereas the telluride in the $SiTe_4$ tetrahedra has a lower charge ranging from -0.709 to -0.817.

5.4.4 Electrochemical Impedance Spectroscopy

Samples of all title compounds were analyzed by impedance spectroscopy to check for Na ion conductivity at elevated temperatures. All compounds show enhanced Na ion conductivity. The color of the samples and band gap calculations indicate that ionic conduction is predominant in all materials. Selected specific conductivities σ_{spec} are shown in Table 5.3 and Figure 5.6.

Table 5.3 Selected specific conductivities σ_{spec} and activation energies E_A of Na_4SiTe_4, $Na_{10}Si_2Te_9$, $Na_6Si_2Te_6$ and $Na_8Si_4Te_{10}$ from electrochemical impedance spectroscopy. For $Na_8Si_4Te_{10}$ ionic conductivity can only be safely detected above 150 °C.

	$\sigma_{\text{spec}}(50\,°\text{C})$ / $\Omega^{-1}\,\text{cm}^{-1}$	E_A / eV
$Na_6Si_2Te_6$	1.3×10^{-6}	0.42
$Na_{10}Si_2Te_9$	3.9×10^{-7}	0.40
Na_4SiTe_4	2.3×10^{-7}	0.41
	$\sigma_{\text{spec}}(200\,°\text{C})$ / $\Omega^{-1}\,\text{cm}^{-1}$	E_A / eV
$Na_6Si_2Te_6$	1.4×10^{-4}	0.42
$Na_8Si_4Te_{10}$	1.1×10^{-6}	0.55

The highest ionic conductivity was found for $Na_6Si_2Te_6$ ($1.3 \times 10^{-6}\,\Omega^{-1}\,\text{cm}^{-1}$ at 50 °C and $1.4 \times 10^{-4}\,\Omega^{-1}\,\text{cm}^{-1}$ at 200 °C). For $Na_6Si_2Te_6$, $Na_{10}Si_2Te_9$ and Na_4SiTe_4 the determined conductivities only differ by one order of magnitude. Also the activation energies differ only slightly. This does not allow to estimate a clear correlation of the ionic conductivity with the chemical composition of these three compounds. $Na_8Si_4Te_{10}$ shows a significantly lower ionic conductivity ($2.3 \times 10^{-7}\,\Omega^{-1}\,\text{cm}^{-1}$ vs. $4.1 \times 10^{-5}\,\Omega^{-1}\,\text{cm}^{-1}$ for $Na_6Si_2Te_6$ at 150 °C).

Even when the differences are small we shall try to figure out reasons for different conductivities. It can firstly be noted that $Na_8Si_4Te_{10}$ has the lowest Na content (36 %). In contrast, the Na content in $Na_6Si_2Te_6$ (43 %), Na_4SiTe_4 (44 %) and $Na_{10}Si_2Te_9$ (48 %) is significantly higher. A lower charge carrier density leads to a lower conductivity. Nevertheless, there are different further factors that have an influence on the Na ion conductivity, especially the differences in Na coordination environment.

Recently, we reported on the Na ion conductivity of Na selenosilicates. Moderate ionic conductivities were found for Na_4SiSe_4-*oP*36, Na_4SiSe_4-*cP*72 and $Na_4Si_2Se_6$-*oP*48 ($\sigma_{\text{spec}} = 1.0 \times 10^{-7}\,\Omega^{-1}\,\text{cm}^{-1}$ at 75 °C, $\sigma_{\text{spec}} = 1.1 \times 10^{-8}\,\Omega^{-1}\,\text{cm}^{-1}$ and $\sigma_{\text{spec}} = 1.4 \times 10^{-8}\,\Omega^{-1}\,\text{cm}^{-1}$ at 50 °C).[5,16] The formal exchange of Se for the higher homologue Te improves the ionic conductivity by about one order of magnitude. It has been shown for different systems that an enlarged unit cell and a softer, more polarizable anionic sublattice can have a positive impact on the ion mobility.[35–37] Compared to the abovementioned fast Na ion conductors Na_3PS_4 ($4.6 \times 10^{-4}\,\Omega^{-1}\,\text{cm}^{-1}$ at room temperature)[11] and Na_3PSe_4 ($1.2 \times 10^{-3}\,\Omega^{-1}\,\text{cm}^{-1}$ at room temperature),[12] the sodium tellurosilicates can be described as moderate to good

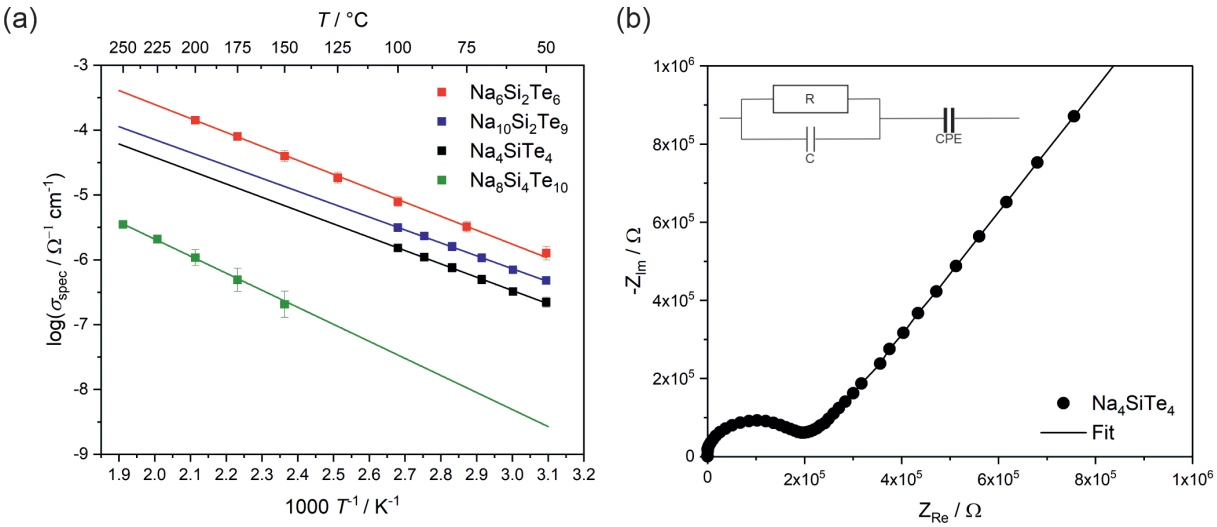

Figure 5.6 (a) Temperature dependent specific ionic conductivities of $Na_6Si_2Te_6$, $Na_{10}Si_2Te_9$, Na_4SiTe_4 and $Na_8Si_4Te_{10}$ with linear fit (solid line). (b) Exemplary Nyquist plot for Na_4SiTe_4 at 100 °C with fit and equivalent circuit.

ionic conductors.

5.5 Conclusion

The sodium tellurosilicates Na_4SiTe_4, $Na_{10}Si_2Te_9$, $Na_6Si_2Te_6$ and $Na_8Si_4Te_{10}$ were synthesized in a two step synthesis procedure consisting of mechanochemical homogenization followed by high-temperature annealing. The crystal structures of the hitherto unknown compounds Na_4SiTe_4 and $Na_{10}Si_2Te_9$ were determined by XRD. Both compounds represent new structure types with isolated $[SiTe_4]^{4-}$ tetrahedra. In the case of $Na_{10}Si_2Te_9$ two tetrahedral units $[SiTe_4]^{4-}$ and also isolated Te^{2-} anions are present. The coordination sphere of the Te^{2-} makes this compound stand out from other alkali chalcogenotetrelates, as there is no Si-Te bond formed. The proposed crystal structure and chemical composition can be substantiated by PXRD and EDX measurements. In accordance with the enhanced ionic mobility the influence of the mobile ions on the whole crystal lattice is observed, i. e., large atomic displacements resulting in significant peaks in final difference Fourier calculations become obvious besides Te atoms.
Electrochemical impedance spectroscopy reveals moderate to good sodium ion conductivity for all compounds. The best ion conductivity was determined for $Na_6Si_2Te_6$ ($\sigma_{spec} = 1.3 \times 10^{-6}\,\Omega^{-1}\,cm^{-1}$ at 50 °C). The detected conductivities for $Na_6Si_2Te_6$, Na_4SiTe_4 and $Na_{10}Si_2Te_9$ are one order of magnitude higher than in comparable sodium selenosilicates. The anionic substructure of $Na_{10}Si_2Te_9$ is reminiscent of Ag_8SiTe_6 which belongs to the large family of argyrodite type compounds. Due to the compositional flexibility of the argyrodite type compounds a similar substitutional variance of $Na_{10}Si_2Te_9$ seems plausible.

References

[1] Eisenmann, B.; Schwerer, H.; Schäfer, H. *Z. Naturforsch. B* **1981**, *36*, 1538–1541.

[2] Eisenmann, B.; Schwerer, H.; Schäfer, H. *Rev. Chim. Minér.* **1983**, *20*, 78–87.

[3] Preishuber-Pflügl, H.; Klepp, K. O. *Z. Kristallogr. - New Cryst. Struct.* **2003**, *218*, 383–384.

[4] Eisenmann, B.; Hansa, J. *Z. Kristallogr. - Cryst. Mater.* **1993**, *203*, 295–296.

[5] Kamm, F.; Pielnhofer, F.; Schlosser, M.; Pfitzner, A. *Inorg. Chem.* **2023**, *62*, 11064–11072.

[6] Eisenmann, B.; Hansa, J.; Schäfer, H. *Z. Anorg. Allg. Chem.* **1985**, *526*, 55–59.

[7] Eisenmann, B.; Schäfer, H. *Z. Anorg. Allg. Chem.* **1982**, *491*, 67–72.

[8] Schlirf, J.; Deiseroth, H. J.; Nilges, T. *Z. Kristallogr. - New Cryst. Struct.* **2000**, *215*, 343–344.

[9] Brinkmann, C.; Eisenmann, B.; Schäfer, H. *Mater. Res. Bull.* **1985**, *20*, 1285–1289.

[10] Jansen, M.; Henseler, U. *J. Solid State Chem.* **1992**, *99*, 110–119.

[11] Hayashi, A.; Noi, K.; Tanibata, N.; Nagao, M.; Tatsumisago, M. *J. Power Sources* **2014**, *258*, 420–423.

[12] Zhang, L.; Yang, K.; Mi, J.; Lu, L.; Zhao, L.; Wang, L.; Li, Y.; Zeng, H. *Adv. Energy Mater.* **2015**, *5*, 1501294.

[13] Krauskopf, T.; Pompe, C.; Kraft, M. A.; Zeier, W. G. *Chem. Mater.* **2017**, *29*, 8859–8869.

[14] Krauskopf, T.; Muy, S.; Culver, S. P.; Ohno, S.; Delaire, O.; Shao-Horn, Y.; Zeier, W. G. *J. Am. Chem. Soc.* **2018**, *140*, 14464–14473.

[15] Harm, S.; Hatz, A.-K.; Schneider, C.; Hoefer, C.; Hoch, C.; Lotsch, B. V. *Front. Chem.* **2020**, *8*, 90.

[16] Kamm, F.; Pielnhofer, F.; Pfitzner, A. *Chem. Mater.* **2024**, *36*, 5643–5650.

[17] WinXPow, Version 3.10; STOE & Cie GmbH, STOE & Cie GmbH: Darmstadt, 2016.

[18] Petříček, V.; Dušek, M.; Palatinus, L. *Z. Kristallogr. - Cryst. Mater.* **2014**, *229*, 345–352.

[19] Palatinus, L.; Chapuis, G. *J. Appl. Crystallogr.* **2007**, *40*, 786–790.

[20] CrysAlisPro (V42); Rigaku Oxford Diffraction Ltd, 2019.

[21] Zahner-Elektrik Zahner Analysis, Version 3.2.4; I. Zahner-Schiller GmbH & Co. KG, Kronach, 2023.

[22] Erba, A.; Desmarais, J. K.; Casassa, S.; Civalleri, B.; Donà, L.; Bush, I. J.; Searle, B.; Maschio, L.; Edith-Daga, L.; Cossard, A.; Ribaldone, C.; Ascrizzi, E.; Marana, N. L.; Flament, J.-P.; Kirtman, B. *J. Chem. Theory Comput.* **2023**, *19*, PMID: 36502394, 6891–6932.

[23] Dovesi, R. et al. CRYSTAL23 User's Manual; University of Torino, 2023.

[24] Sophia, G.; Baranek, P.; Sarrazin, C.; Rerat, M.; Dovesi, R., `https://www.crystal.unito.it/Basis_Sets/sodium.html`, Accessed: 2023-03-06, 2014.

[25] Porter, A. R.; Towler, M. D.; Needs, R. J. *Phys. Rev. B* **1999**, *60*, 13534–13546.

[26] Heyd, J.; Peralta, J. E.; Scuseria, G. E.; Martin, R. L. *J. Chem. Phys.* **2005**, *123*, 174101.

[27] Becke, A. D. *Phys. Rev. A* **1988**, *38*, 3098–3100.

[28] Heyd, J.; Scuseria, G. E.; Ernzerhof, M. *J. Chem. Phys.* **2003**, *118*, 8207–8215.

[29] Hinuma, Y.; Pizzi, G.; Kumagai, Y.; Oba, F.; Tanaka, I. *Comput. Mater. Sci.* **2017**, *128*, 140–184.

[30] Jørgensen, J.-E.; Rasmussen, S. E. *J. Cryst. Growth* **1979**, *47*, 124–126.

[31] Eickhoff, H.; Strangmüller, S.; Klein, W.; Kirchhain, H.; Dietrich, C.; Zeier, W. G.; van Wüllen, L.; Fässler, T. F. *Chem. Mater.* **2018**, *30*, 6440–6448.

[32] Zintl, E.; Harder, A.; Dauth, B. *Z. Elektrochem. Angew. Phys. Chem.* **1934**, *40*, 588–593.

[33] Assoud, A.; Kleinke, H. *Chem. Mater.* **2005**, *17*, 4509–4513.

[34] Boucher, F.; Evain, M.; Brec, R. *J. Solid State Chem.* **1992**, *100*, 341–355.

[35] Bachman, J. C.; Muy, S.; Grimaud, A.; Chang, H.-H.; Pour, N.; Lux, S. F.; Paschos, O.; Maglia, F.; Lupart, S.; Lamp, P.; Giordano, L.; Shao-Horn, Y. *Chem. Rev.* **2016**, *116*, PMID: 26713396, 140–162.

[36] Kraft, M. A.; Culver, S. P.; Calderon, M.; Böcher, F.; Krauskopf, T.; Senyshyn, A.; Dietrich, C.; Zevalkink, A.; Janek, J.; Zeier, W. G. *J. Am. Chem. Soc.* **2017**, *139*, 10909–10918.

[37] Xuan, M.; Xiao, W.; Xu, H.; Shen, Y.; Li, Z.; Zhang, S.; Wang, Z.; Shao, G. *J. Mater. Chem. A* **2018**, *6*, 19231–19240.

6 Conclusion and Outlook

In the present work compounds in the system Na-Tt-Q with Tt = Si, Ge, Sn and Q = Se, Te were investigated. In the past, few materials containing these elements were structurally characterized but physical and chemical properties were still mostly unknown. By using a two-step synthesis procedure consisting of mechanochemical homogenization followed by annealing, the phase pure synthesis of literature known compounds as well as hitherto unknown compounds was possible.

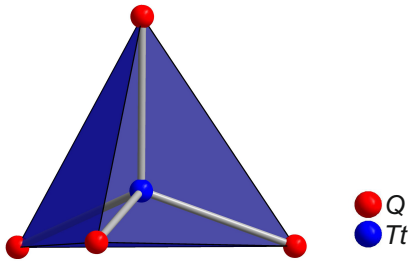

Figure 6.1 TtQ_4^{4-} tetrahedra.

The simplest anionic units which are observed in this class of compounds are isolated TtQ_4^{4-} tetrahedra (Figure 6.1). In chapter 3 sodium selenotetrelates with such isolated $Tt\mathrm{Se}_4^{4-}$ tetrahedra (Tt = Si, Ge, Sn) were characterized regarding their crystal structures and sodium ion conductivities. Two different modifications of Na_4SiSe_4 were observed. The formation of both modifications from the ball milled reaction mixture was investigated by in-situ high-temperature X-ray powder diffraction. While heating the reaction mixture, at first the metastable orthorhombic modification, Na_4SiSe_4-$oP36$, was observed. By heating further, a cubic modification is formed. Na_4SiSe_4-$cP72$ crystallizes in the Ba_4SiAs_4 structure type and is only stable in a small temperature range of 350 °C to 400 °C. At higher temperatures, the cubic modification retransforms to Na_4SiSe_4-$oP36$. DFT calculations reveal Na_4SiSe_4-$cP72$ to be the more stable modification (ΔE = 8.6 kJ mol^{-1}).

For Na_4SnSe_4 also a new modification was synthesized. Na_4SnSe_4-$tI216$ crystallizes in the Na_4SnTe_4-$tI216$ structure type. DFT modeling reveals Na_4SnSe_4-$tI216$ to be metastable. The already known modification, Na_4SnSe_4-$tP18$, is more stable by 2.5 kJ mol^{-1}.

DFT calculations were performed for all $Na_4Tt\mathrm{Se}_4$ compounds including modelling of further hypothetical structure types for the 4 : 1 : 4 composition. The existence of

additional compounds seems probable as there are only small energy differences between different structure types, e.g. hypothetical Na_4SiSe_4-$tP18$ (Na_4SnS_4 structure type) is $1.9\,kJ\,mol^{-1}$ lower in energy than Na_4SiSe_4-$cP72$.

For Na_4GeSe_4 three different hypothetic structure types were observed which are lower in energy with respect to the experimentally observed Na_4GeSe_4-$oP72$. The plausibility for hypothetical Na_4SiSe_4-$tP18$ and Na_4GeSe_4-$tP18$ was additionally substantiated with phonon dispersion calculations. Thus, the existence of further modifications of Na_4SiSe_4 and Na_4GeSe_4 seems plausible.

All investigated compounds show moderate sodium ion conductivity. The best ion conductivity was determined for Na_4GeSe_4 with $\sigma_{spec} = 6.6 \times 10^{-8}\,S\,cm^{-1}$ at 50 °C. The other compounds show slightly lower conductivities. Other selenotetrelates exhibit similar ionic conductivities (see below).

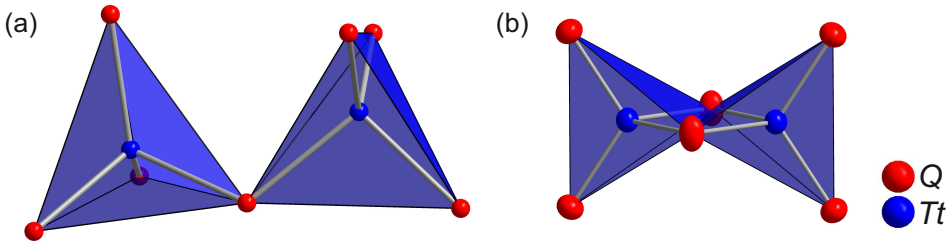

Figure 6.2 (a) corner-sharing tetrahedra units $Tt_2Q_7^{6-}$ and (b) edge-sharing tetrahedra units $Tt_2Q_6^{4-}$.

Besides isolated tetrahedra, the anionic units can also consist of several tetrahedra which are connected in different ways. The next larger anionic unit would consist of two tetrahedra (Figure 6.2). In $Na_6Si_2Se_7$ two tetrahedra sharing common corners form $Si_2Se_7^{6-}$ units (Figure 6.2a), whereas edge sharing tetrahedra were not observed before. $Na_4Si_2Se_6$-$tP24$ represents the first compound in the regarded system where edge sharing tetrahedra form $Si_2Se_6^{4-}$ units (Figure 6.2b). As described in chapter 4, $Na_4Si_2Se_6$ exists in two different modifications with different anionic structures. The second polymorph, $Na_4Si_2Se_6$-$oP48$, crystallizes in a new structure type with *zweier* single chains $^1_\infty[Si_2Se_6]^{4-}$ (Figure 6.3).

The phase transition was observed after application of pressure (0.1 GPa) as well as after high temperature annealing. DFT calculations reveal that both polymorphs are very close in energy and that the existence of further modifications seems plausible. $Na_4Si_2Se_6$-$oP48$ exhibits moderate Na ion conductivity in the same order of magnitude as found for $Na_4\,TtSe_4$ ($\sigma_{spec}(Na_4Si_2Se_6\text{-}oP48) = 1.4 \times 10^{-8}\,S\,cm^{-1}$ at 50 °C).

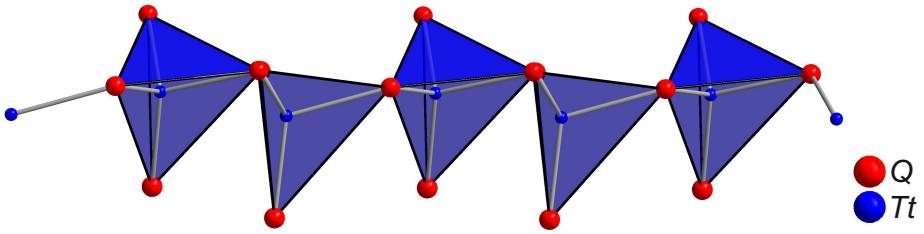

Figure 6.3 Chain of corner-sharing TtQ_4-tetrahedra.

In the hypochalcogenoditetrelates $Na_6Ge_2Se_6$, $Na_6Si_2Te_6$ and $Na_6Ge_2Te_6$ ethane-like $Tt_2Q_6^{6-}$ anionic units were observed (Figure 6.4a). The synthesis of the corresponding silicon compound $Na_6Si_2Se_6$ still remains challenging. Heating a ball-milled reaction mixture in the corresponding stochiometric ratio to high temperatures (750 °C to 800 °C) seems a promising synthesis approach. First attempts suggest the existence of $Na_6Si_2Se_6$ which appears to be at least structurally related to $Na_6Ge_2Se_6$. Nevertheless, the synthesis conditions have to be adjusted to get powder data of good quality.

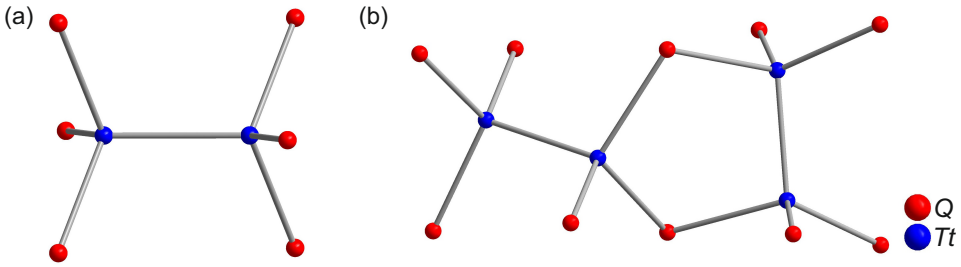

Figure 6.4 (a) Ethane-like $Tt_2Q_6^{6-}$ units and (b) $Tt_4Q_{10}^{8-}$ units.

In chapter 5 sodium tellurosilicates were investigated regarding their Na ion conductivity. Besides the literature-known $Na_6Si_2Te_6$ and $Na_8Si_4Te_{10}$ (Figure 6.4 a and b) two new compounds were characterized. Na_4SiTe_4 and $Na_{10}Si_2Te_9$ both represent new structure types with isolated $SiTe_4^{4-}$ tetrahedra. In the case of $Na_{10}Si_2Te_9$, also isolated Te^{2-} anions were observed. This structural feature was not yet observed in other alkali chalcogenotetrelates, but is already known from other substance classes, e.g. from argyrodites.

The electronic structures of all mentioned sodium tellurosilicates were evaluated on the basis of DFT calculations. All compounds exhibit semiconducting behavior with band gaps in the range of 2.29 eV ($Na_{10}Si_2Te_9$) to 2.81 eV (Na_4SiTe_4).

Electrochemical impedance spectroscopy reveals moderate to good sodium ion conductivity for $Na_6Si_2Te_6$, $Na_{10}Si_2Te_9$ and Na_4SiTe_4. The conductivities are one to two orders of

magnitudes higher than in the investigated selenosilicates.
Synthesis attempts were also made for the corresponding Se compound $Na_{10}Si_2Se_9$ but have not been successful so far. First experiments suggested the existence of mixed compounds $Na_{10}Si_2Te_8Se$ and $Na_{10}Si_2Te_7Se_2$. According to X-ray powder diffraction experiments, both compounds crystallize isotypically to $Na_{10}Si_2Te_9$ but the exact position of the Se atoms could not be determined. Se is expected to form isolated Se^{2-} anions, but this expectation can not be verified with X-ray powder diffraction. A more precise structure characterization via single crystal X-ray diffraction is still necessary.

One main aspect of this work was the determination of the sodium ion conductivity of the synthesized compounds. All considered compounds show moderate to good sodium ion conductivities. The temperature dependent specific ionic conductivities of all compounds described in this work are shown in Figure 6.5.

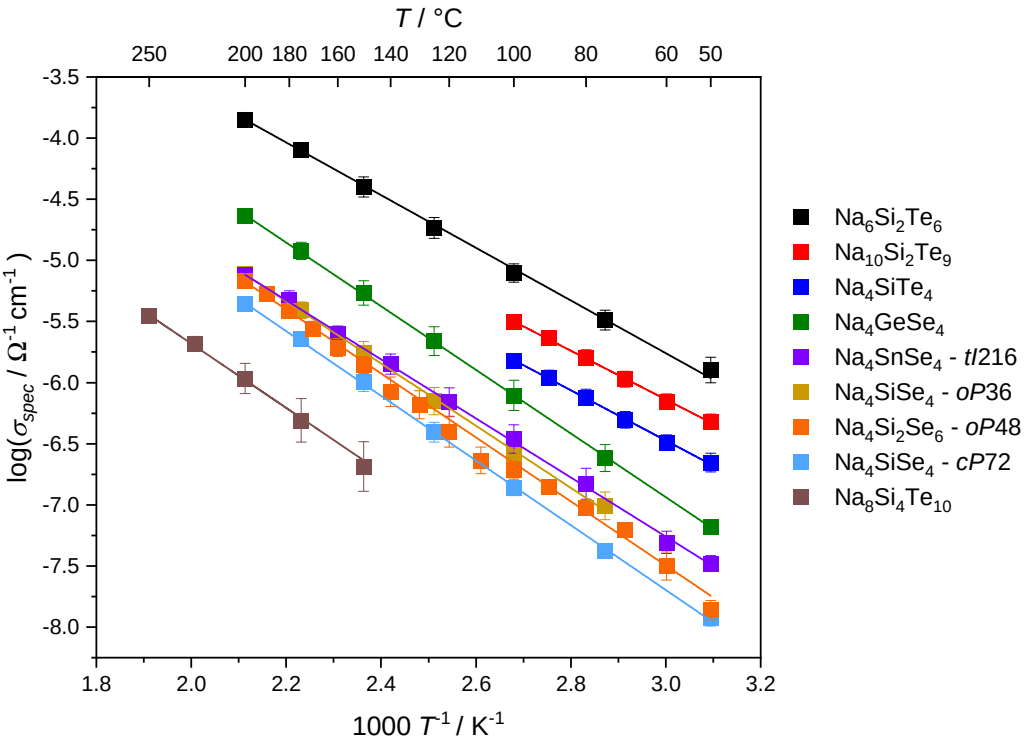

Figure 6.5 Temperature dependent specific ionic conductivity of all compounds described in this work with linear fits (solid lines).

The conductivities are in the range of $\sigma_{spec}(200\,°C) = 1.4 \times 10^{-4}\,\Omega^{-1}\,cm^{-1}$ for $Na_6Si_2Te_6$ to $\sigma_{spec}(200\,°C) = 1.1 \times 10^{-6}\,\Omega^{-1}\,cm^{-1}$ for $Na_8Si_4Te_{10}$. To explain the observed trend in Na ion conductivities, several different influencing factors have to be taken into account. For

the following classification and possible explanations it has to be kept in mind, that conductivity measurements differing by less than one order of magnitude are not significantly different. However, some key aspects determining the conductivities will be mentioned. One main influencing factor is the number of available charge carriers. The trend of conductivities can be followed roughly by considering the sodium content in the respective compounds. The highest sodium content was found for $Na_{10}Si_2Te_9$ (47.6 %) which has the second highest conductivity ($\sigma_{spec} = 3.9 \times 10^{-7}\,\Omega^{-1}\,cm^{-1}$ vs. $1.3 \times 10^{-6}\,\Omega^{-1}\,cm^{-1}$ for $Na_6Si_2Te_6$ (42.9 %) at 50 °C). This is followed by the compounds with the 4 : 1 : 4 composition (44.4 %) and $Na_4Si_2Se_6$-*oP*48 (33.3 %). The lowest sodium ion conductivity was determined for $Na_8Si_4Te_{10}$ which also has the second lowest sodium content (36.4 %). Apart from this, also the Na coordination environments influences the conductivity. In general, a higher versatility in the Na coordination spheres should result in a flatter energy surface and enhances the Na ion conductivity. Furthermore, the formal exchange of Se for the higher homologue Te can also improve the ionic conductivity. Na_4SiSe_4 has a slightly lower conductivity ($1.0 \times 10^{-7}\,\Omega^{-1}\,cm^{-1}$ at 75 °C) compared to the higher homologue Na_4SiTe_4 ($2.3 \times 10^{-7}\,\Omega^{-1}\,cm^{-1}$ at 50 °C).

In a next step, it is necessary to examine further compounds in the regarded system concerning their sodium ion conductivity for a more detailed understanding of the trend in conductivities. Moreover, the aim of future work should be the synthesis and characterization of the hitherto unknown but conceivable compounds like $Na_6Si_2Se_6$ or compounds including new anionic units like cyclosilicates and exhibit channels or layered structures for an enhanced sodium ion mobility.

A Supporting Information for Chapter 3

A.1 Na_4SiSe_4-*cP*72

Table A.1 Crystallographic data and details of the structure determination of Na_4SiSe_4-*cP*72.

chemical formula	Na_4SiSe_4
powder color	brown
T / K	296
crystal system	cubic
space group	$P\bar{4}3n$ (No. 218)
a / Å	12.1295(1)
V / Å^3	1784.543(5)
formula units Z	8
calculated density ρ_{calc} / g cm^{-3}	3.2448
diffractometer	STOE Stadi P, Debye-Scherrer geometry
radiation	CuKα_1 (λ = 1.5406 Å)
measurement range $2\Theta_{\min}$ / $2\Theta_{\max}$	2.000° / 90.545°
2Θ step	0.015°
number of parameters / restraints	23 / 0
R_P, wR_P, R_{exp}	0.0490, 0.0681, 0.0430
goodness of fit	1.58
R_{gt}, wR_{gt} ($I > 3\sigma$)	0.0376, 0.0452
R_{all}, wR_{all}	0.0398, 0.0456
$\Delta\rho_{min}$, $\Delta\rho_{max}$ / e/Å^3	-0.79, 0.85

Table A.2 Atomic positions and displacement parameters in Na_4SiSe_4-$cP72$ at room temperature.

	wyck. positions	x	y	z	U_{iso}
Na1	24i	0.4125(3)	0.3684(2)	0.1510(4)	0.042(1)
Na2	8e	0.1517(4)	x	x	0.041(3)
Si1	2a	1/2	1/2	1/2	0.029(5)
Si2	6c	1/4	1/2	0	0.028(2)
Se1	8e	0.3930(1)	x	x	0.032(1)
Se2	24i	0.14874(8)	0.39921(9)	0.11887(6)	0.0248(3)

Table A.3 Comparison of selected interatomic distances (Å) and angles (°) of Na_4SiSe_4-$cP72$ and Na_4SiSe_4-$oP36$.[1] In each case, Si is surrounded by four Se and Na by six Se.

	Na_4SiSe_4-$cP72$	Na_4SiSe_4-$oP36$
Si1 - Se	2.248(2)	2.248 - 2.270
Si2 - Se	2.254(1)	
Na1 - Se	2.933(4) - 3.245(4)	2.816 - 3.705
Na2 - Se	3.028(5), 3.230(5)	2.963 - 3.886
Na3 - Se		2.883 - 3.711
Se - Si1 - Se	109.47(6)	107.401 - 116.33
Se - Si2 - Se	107.27(4), 113.97(3)	

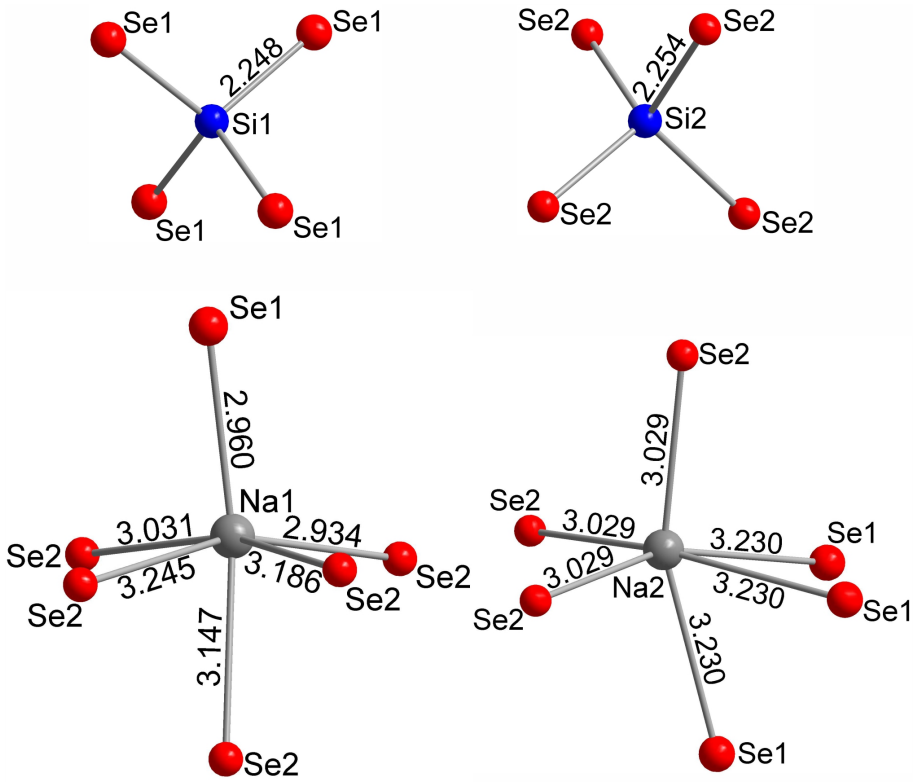

Figure A.1 Coordination polyhedra of Si and Na in Na_4SiSe_4-$cP72$ with bond lengths in Å.

A.2 Na_4SiSe_4-*oP*36

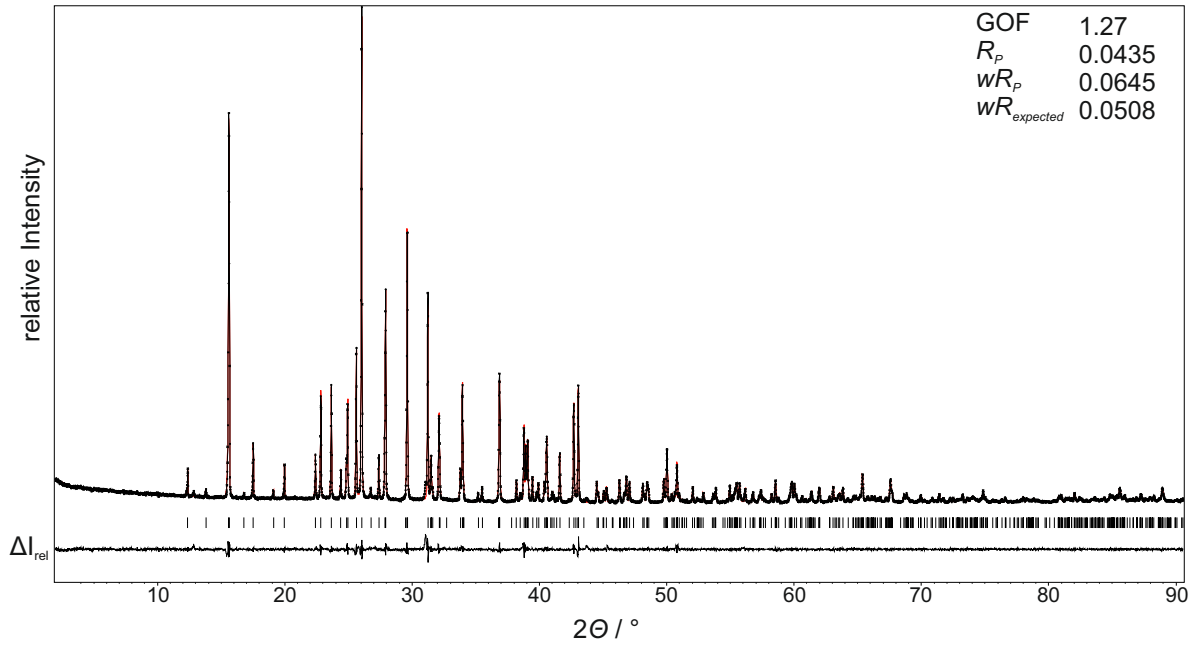

Figure A.2 X-ray powder diffraction pattern of Na_4SiSe_4-*oP*36. Profile fit and refinement of lattice parameter was done using a structure model from *Preishuber-Pflügl*.[1]

Table A.4 Refined lattice parameters of Na_4SiSe_4-*oP*36 from X-ray powder data and published lattice parameters.[1] The lattice parameters from the CAD4 are typically slightly smaller than the corresponding data from powder diffraction.

	a / Å	b / Å	c / Å	V / Å^3
refined	14.2564(1)	9.2729(1)	7.1563(1)	946.050(9)
published	14.182(5)	9.208(3)	7.122(3)	930.05

A.3 Na_4GeSe_4

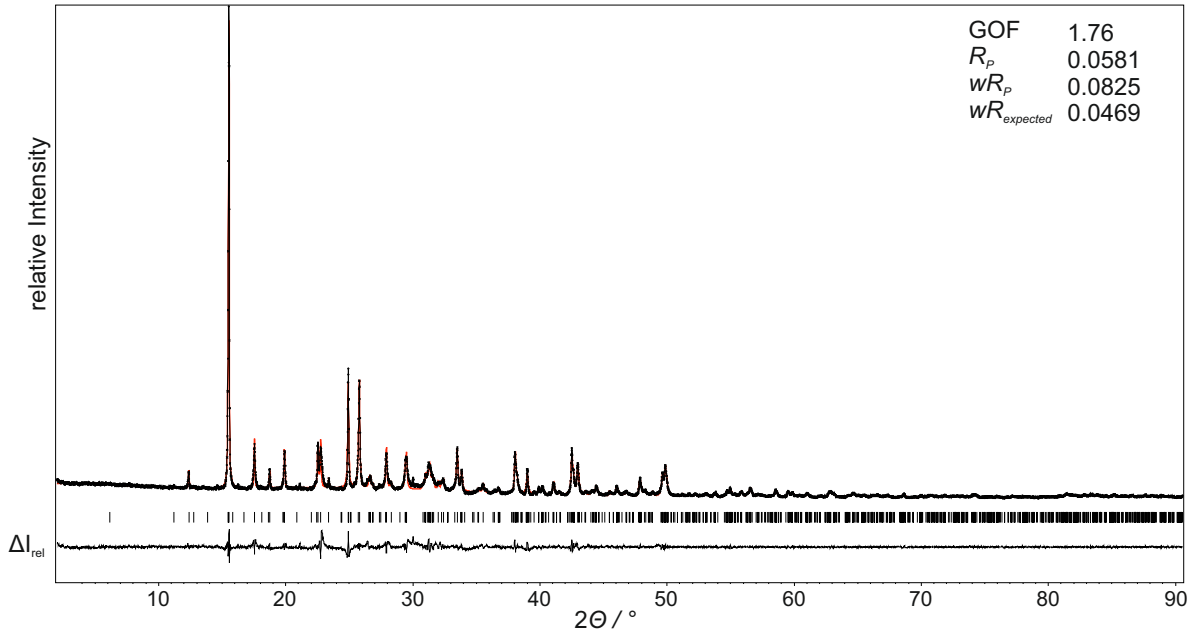

Figure A.3 X-ray powder diffraction pattern of Na_4GeSe_4. Profile fit and refinement of lattice parameters was done using a structure model from *Klepp*.[2]

Table A.5 Refined lattice parameters of Na_4GeSe_4 from X-ray powder data in comparison to the published data.[2]

	a / Å	b / Å	c / Å	V / Å^3
refined	28.539(2)	9.4505(8)	7.1377(6)	1925.1(3)
published	28.518	9.447	7.128	1920.35

A.4 Na_4SnSe_4-*tI*216

Table A.6 Crystallographic data and structure determination details of Na_4SnSe_4-*tI*216.

chemical formula	Na_4SnSe_4
crystal shape, color	block, yellow
size	0.241 × 0.15 × 0.096
T / K	296.0(3)
crystal system	tetragonal
space group	$I\bar{4}/acd$ (No.142)
a / Å	14.4053(4)
c / Å	28.5751(8)
V / Å^3	5929.7(3)
formula units Z	24
calculated density ρ_{calc} / g cm^{-3}	3.5386
diffractometer	Rigaku SuperNova Dualflex, AtlasS2
radiation	MoKα ($\lambda = 0.710\,73$ Å)
measurement method	ω - scan
measurement range Θ_{min} / Θ_{max}	2.46° / 37.74°
index range *hkl*	-19 < h < 24, -24 < k < 24, -48 < l < 43
measured / independent reflections (R_{int})	35971 / 3861 (0.0295)
independent reflections [$I \geq 3\sigma(I)$]	3233
completeness	0.999
absorption coefficient $\mu_{\mathrm{MoK}\alpha}$	17.41 mm^{-1}
absorption correction	gaussian
transmission T_{min}, T_{max}	0.132 / 0.49
structure solution	*Superflip*
structure refinement	*Jana2006*
data / restraints / parameter	3861 / 0 / 65
goodness of fit	1.22
final R, wR [$I \geq 2\sigma(I)$]	1.87, 4.22
final R, wR [all data]	2.74, 4.51
$\Delta\rho_{\mathrm{min}}$, $\Delta\rho_{\mathrm{max}}$ / e/Å^3	-1.29, 0.75

Table A.7 Atomic positions and displacement parameters in Na_4SnSe_4-*tI*216 at room temperature.

	wyck. positions	x	y	z	U_{ani}
Na1	16*e*	0.95266(8)	3/4	3/8	0.0377(4)
Na2	16*c*	3/4	1/2	3/8	0.0410(4)
Na3	16*f*	0.72478(6)	0.77522(6)	1/2	0.0432(3)
Na4	16*d*	1/2	1/2	0.62623(5)	0.0456(5)
Na5	32*g*	0.75220(6)	0.52568(7)	0.50402(3)	0.0396(3)
Sn1	8*a*	1/2	1/2	1/2	0.01710(4)
Sn2	16*e*	1/4	0.704629(10)	5/8	0.01709(4)
Se1	32*g*	0.80748(1)	0.65522(1)	0.428472(5)	0.01890(4)
Se2	32*g*	0.58833(1)	0.61230(1)	0.550315(6)	0.02477(5)
Se3	32*g*	0.35402(1)	0.60472(1)	0.675403(6)	0.02189(4)

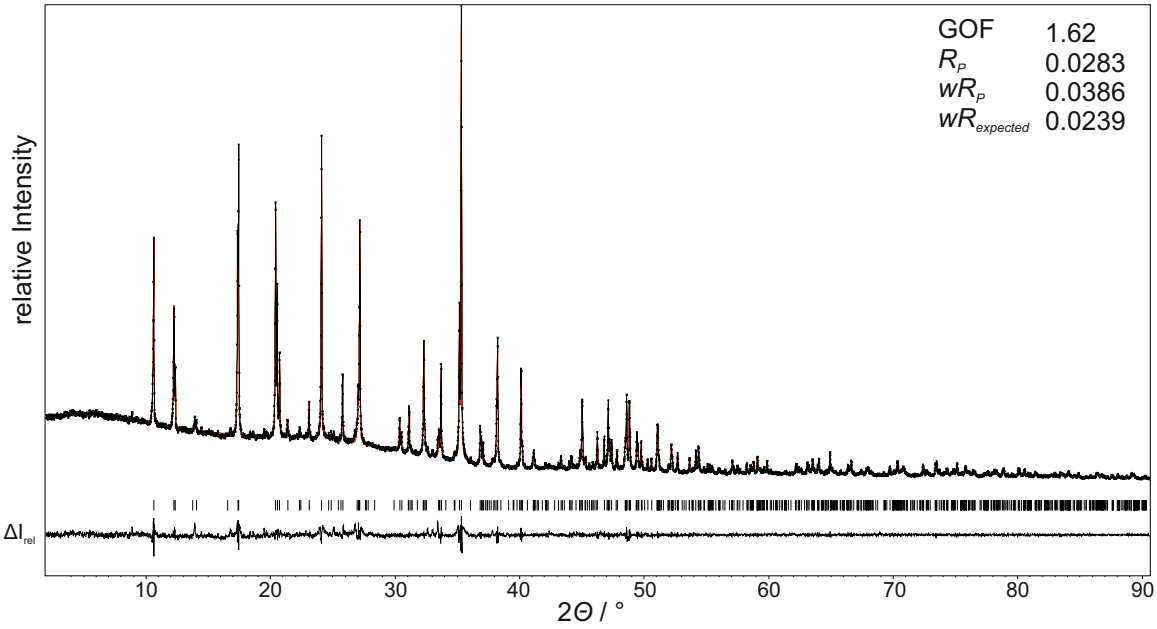

Figure A.4 X-ray powder diffraction pattern of Na_4SnSe_4-*tI*216. Profile fit and refinement was done using a structure model from single crystal diffraction.

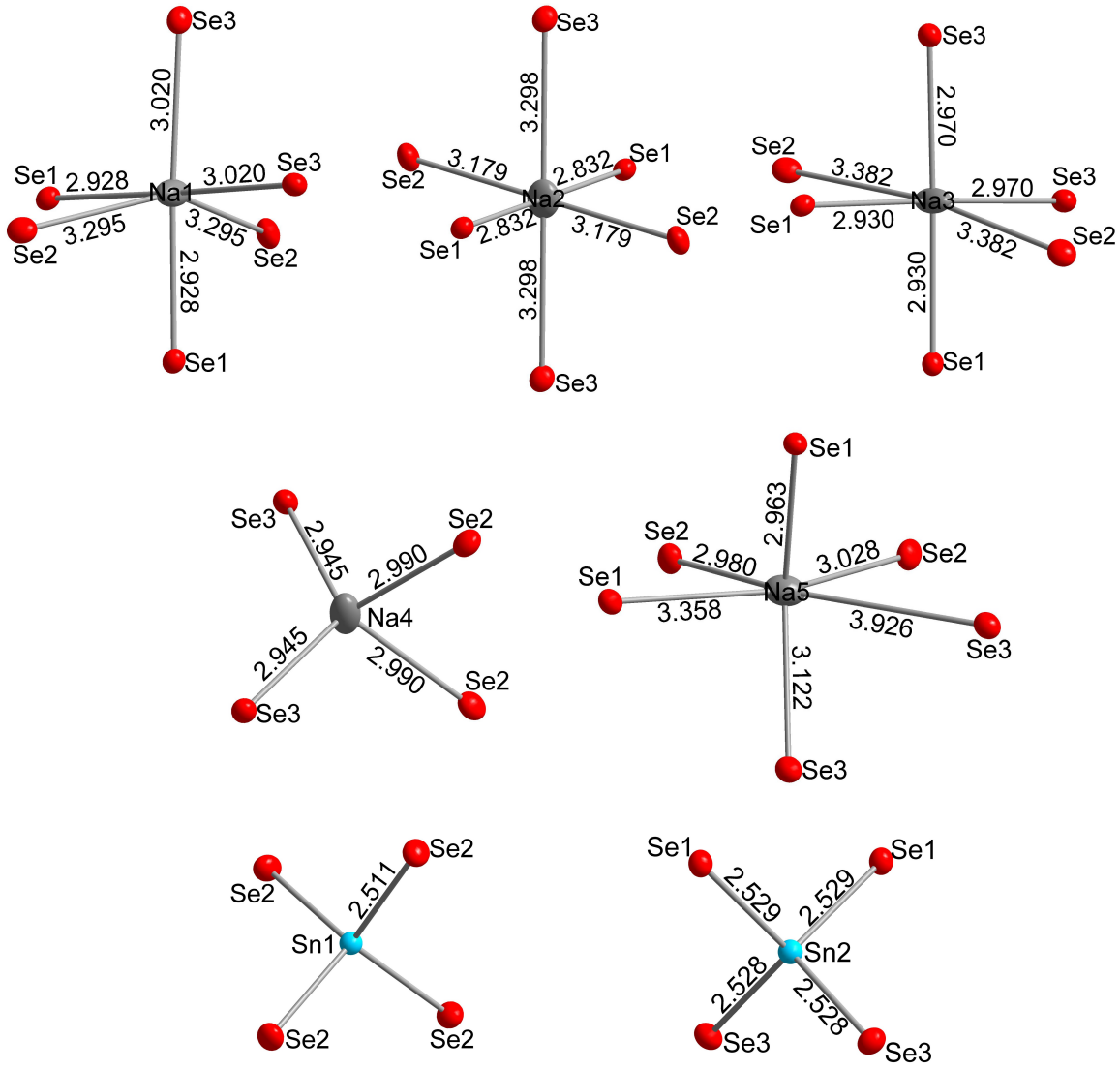

Figure A.5 Coordination polyhedra of Na and Sn in Na_4SnSe_4-*tI*216 with distances in Å.

Table A.8 Comparison of selected interatomic distances (Å) and angles (°) of Na_4SnSe_4-*tI*216 and Na_4SnSe_4-*tP*18.[3] In each case, Sn is surrounded by four Se. In Na_4SnSe_4-*tI*216, Na1, Na2, Na3 and Na5 are surrounded by six Se (Na_{oct}) and Na4 by four Se (Na_{tet}). In Na_4SnSe_4-*tP*18 Na is surrounded by five Se (Na_{pent}).

	Na_4SnSe_4-*tI*216	Na_4SnSe_4-*tP*18
Sn1 - Se	2.5106(2)	2.523
Sn2 - Se	2.5286(2), 2.5280(2)	
Na_{oct}	2.8320(2) - 3.9255(9)	
Na_{tet}	2.9449(7) - 2.990(1)	
Na_{pent}		2.922 - 3.224
Se - Sn1 - Se	109.145(6), 110.126(6)	107.569, 113.347
Se - Sn2 - Se	108.264(8) - 110.965(6)	

A.5 Differential thermal analysis (DTA)

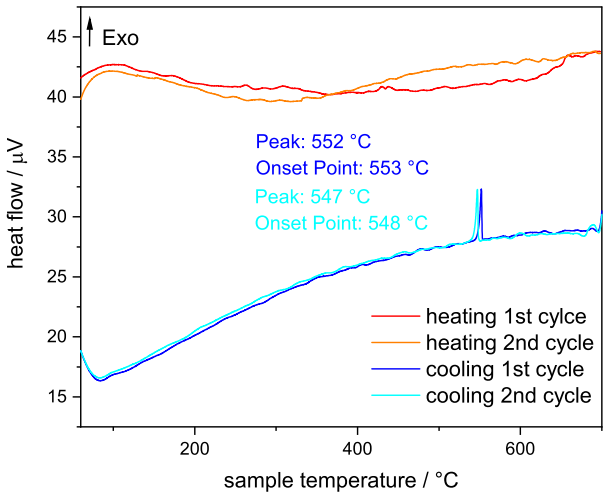

Figure A.6 DTA curve of a sample of pristine "Na_4SiSe_4" after ball milling (heating/cooling rate 5 °C min^{-1}). Peaks at 553 °C and 548 °C in the first and second cooling cycle are observed.

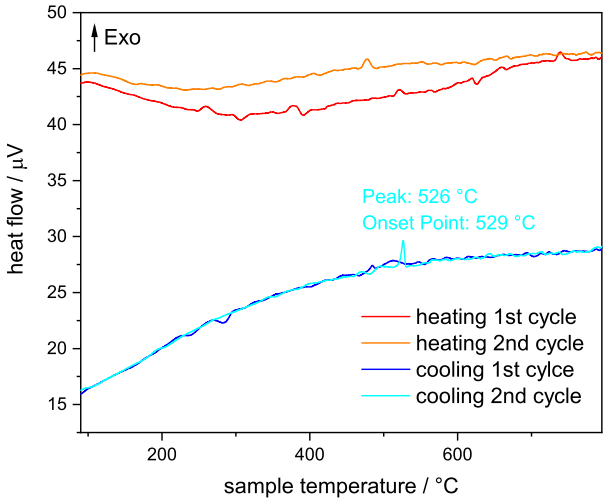

Figure A.7 DTA curve of a sample of Na_4SiSe_4-*cP*72. The heating/ cooling rate was set to 5 °C min^{-1}. The peak at 529 °C in the second cooling cycle probably stems from the reformation of Na_4SiSe_4-*oP*36.

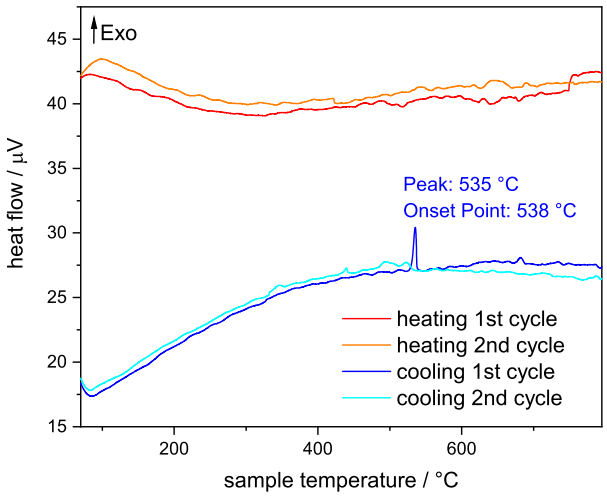

Figure A.8 DTA curve of a sample of Na_4SiSe_4-*oP*36. The heating/ cooling rate was set to 5 °C min^{-1}. The peak at 538 °C in the first cooling cycle probably stems from the reformation of Na_4SiSe_4-*oP*36.

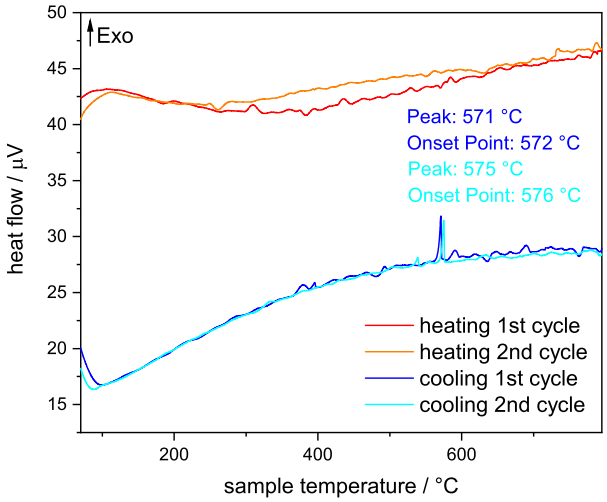

Figure A.9 DTA curve of a sample of Na_4GeSe_4. The heating/ cooling rate was set to $5\,°C\,min^{-1}$. The peaks at 572 °C and 576 °C in the first and second cooling cycle probably stem from the reformation of Na_4GeSe_4.

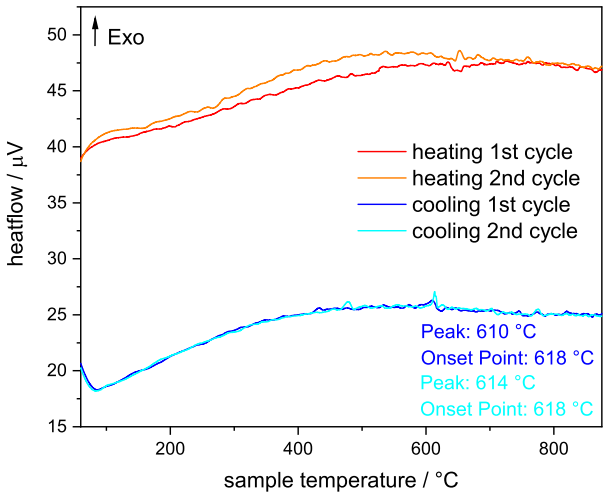

Figure A.10 DTA curve of a sample of Na_4SnSe_4-$tI216$ (heating/ cooling rate $5\,°C\,min^{-1}$). The peaks at 618 °C in the first and second cooling cycle can be assigned to the phase transition from Na_4SnSe_4-$tI216$ to Na_4SnSe_4-$tP18$. The corresponding transformation from low temperature to high temperature polymorph is not clearly visible.

A.6 DFT modeling

A.6.1 Basis Sets

Basis sets were taken from the CRYSTAL homepage (Na,[4] Si,[5] Ge,[6] Sn[7] and Se[8]). The outer shells were optimized for Na_4SiSe_4-$oP36$, Na_4GeSe_4 and Na_4SnSe_4-$tP18$, respectively. For modelling of further polymorphs with the same composition also these optimized basis sets were used. The optimized outer shells of all used basis sets are given in the following.

Table A.9 Na basis set optimized for Na_4SiSe_4-$oP36$ and Na_4GeSe_4.

Na	exponent	coefficient
$4sp$	0.1917	s: 1.0 p: 1.0
$3d$	0.1	1.0

Table A.10 Si Basis set optimized for Na_4SiSe_4-$oP36$.

Si	exponent	coefficient
$6sp$	0.1581	s: 1.0 p: 1.0
$3d$	0.3250	1.0

Table A.11 Se Basis set optimized for Na_4SiSe_4-$oP36$.

Se	exponent	coefficient
$4sp$	0.13307	s: 1.0 p: 1.0
$4d$	1.0422	1.0

Table A.12 Ge basis set optimized for Na_4GeSe_4.

Ge	exponent	coefficient
$4p$	0.1	1.0
$4d$	0.2632	1.0

Table A.13 Se basis set optimized for Na_4GeSe_4.

Se	exponent	coefficient
5*sp*	0.1349	*s*: 1.0 *p*: 1.0
4*d*	1.0421	1.0

Table A.14 Na basis set optimized for Na_4SnSe_4-*tP*18.

Na	exponent	coefficient
4*sp*	0.2241	*s*: 1.0 *p*: 1.0
3*d*	0.1	1.0

Table A.15 Sn basis set optimized for Na_4SnSe_4-*tP*18.

Sn	exponent	coefficient
6*sp*	0.1	*s*: 1.0 *p*: 1.0
5*d*	0.1451	1.0

Table A.16 Se basis set optimized for Na_4SnSe_4-*tP*18.

Se	exponent	coefficient
6*sp*	0.1	*s*: 1.0 *p*: 1.0
4*d*	1.0551	1.0

A.6.2 Equation of State calculations

The calculated E and V values were fitted with the Birch-Murnaghan EOS[9–11] (equation 1).

$$E(V) = E_0 + \frac{9V_0B_0}{16}\left\{\left[\left(\frac{V_0}{V}\right)^{\frac{2}{3}} - 1\right]^3 B_0' + \left[\left(\frac{V_0}{V}\right)^{\frac{2}{3}} - 1\right]^2 \left[6 - 4\left(\frac{V_0}{V}\right)^{\frac{2}{3}}\right]\right\} \quad \text{(A.1)}$$

Table A.17 Fit data for Birch-Murnaghan EOS.

Polymorph	B_0 / GPa	B_0'
Na_4SiSe_4-$cP72$	21.3	4.4
Na_4SiSe_4-$oP36$	20.4	5.1
Na_4SiSe_4-$oP72$	20.4	5.1
Na_4SiSe_4-$tP18$	19.4	11.8
Na_4SiSe_4-$tI216$	21.9	5.1
Na_4SnSe_4-$tP18$	16.4	11.3
Na_4SnSe_4-$tI216$	17.8	5.7

A.6.3 Band Structures

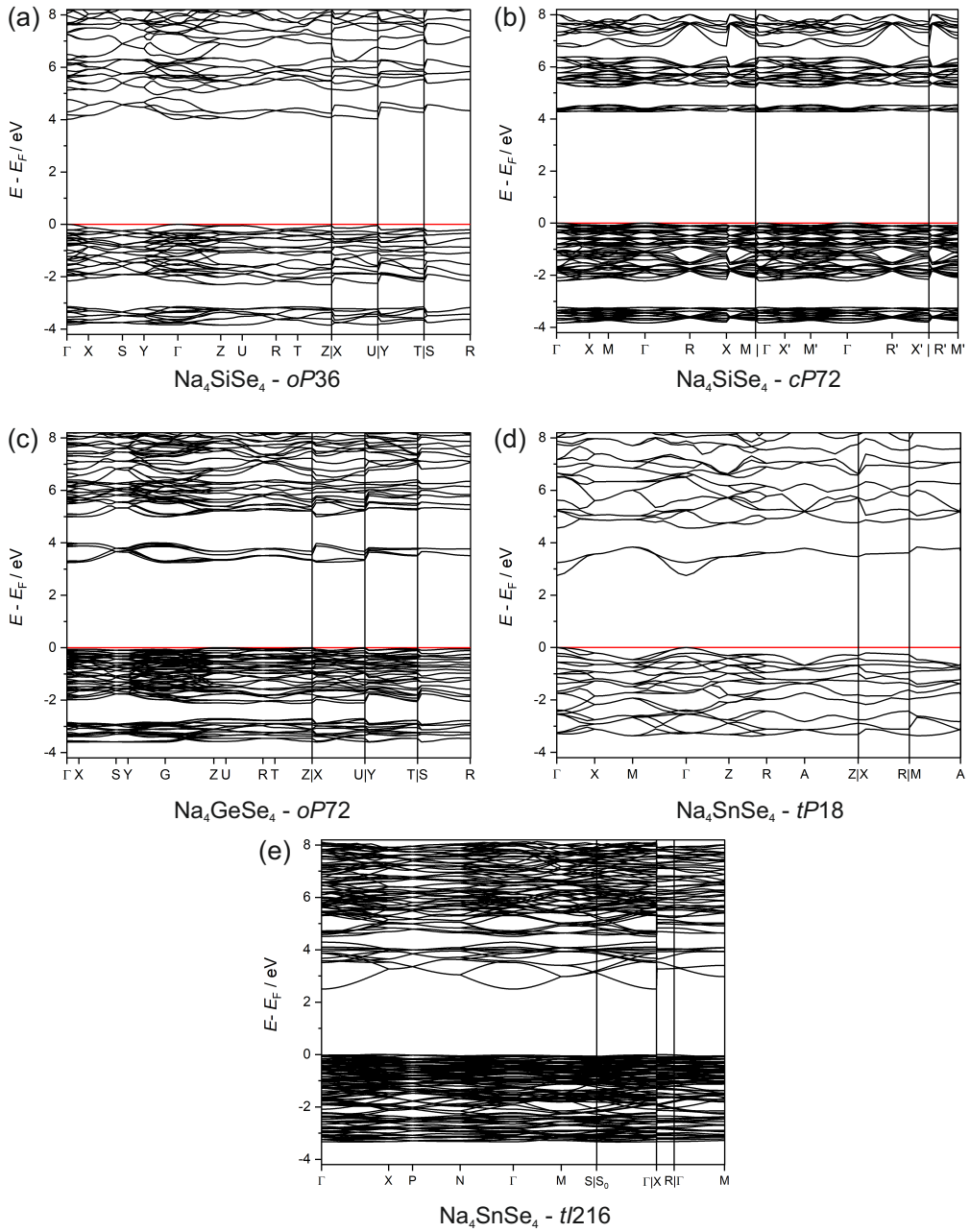

Figure A.11 DFT calculated band structures of (a) Na_4SiSe_4-*oP*36, (b) Na_4SiSe_4-*cP*72, (c) Na_4GeSe_4-*oP*72, (d) Na_4SnSe_4-*tP*18 and (e) Na_4SnSe_4-*tI*216.

A.6.4 Density of States

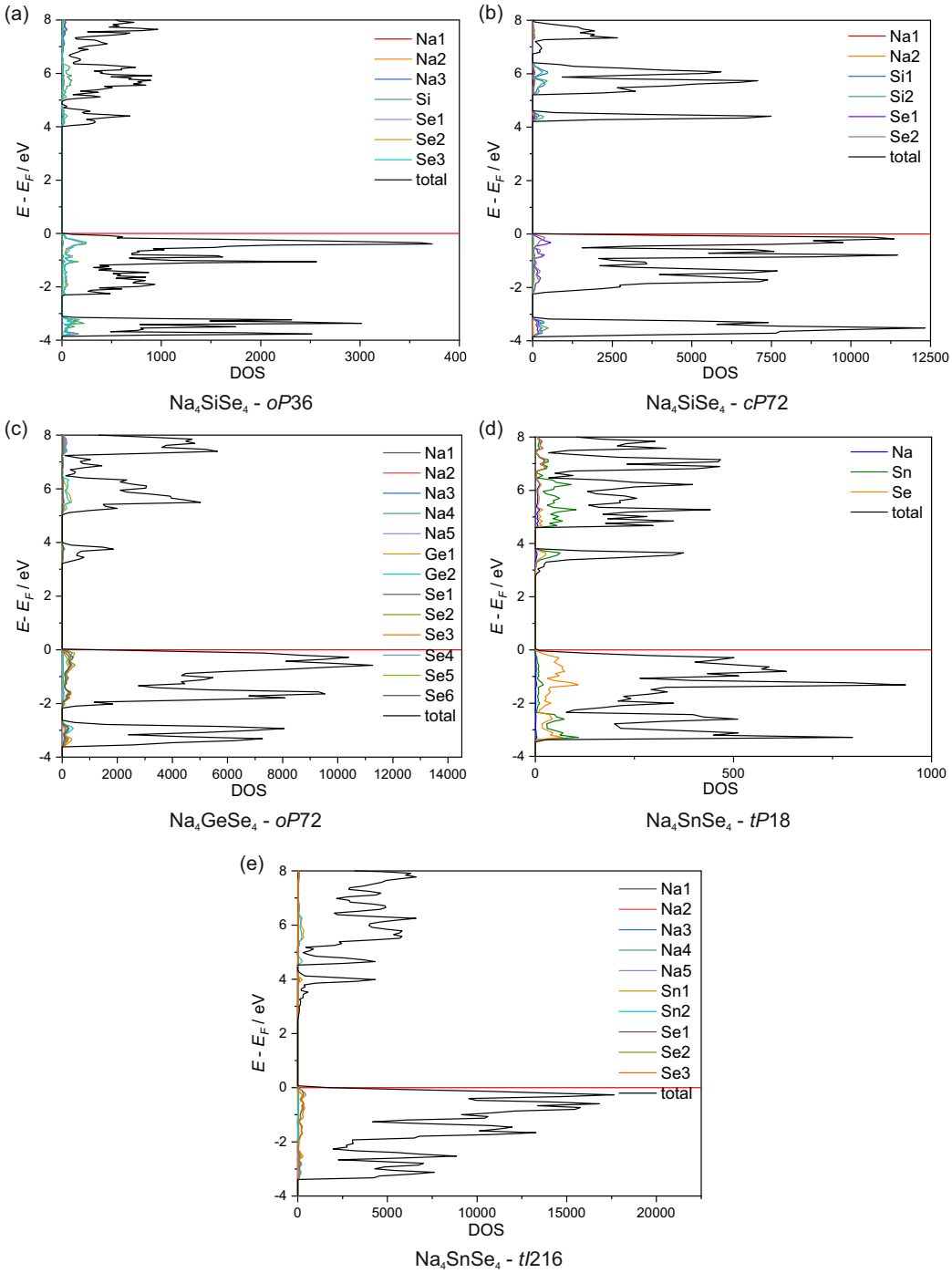

Figure A.12 DFT calculated density of states of (a) Na_4SiSe_4-*oP*36, (b) Na_4SiSe_4-*cP*72, (c) Na_4GeSe_4-*oP*72, (d) Na_4SnSe_4-*tP*18 and (e) Na_4SnSe_4-*tI*216.

A.6.5 Phonon Dispersion

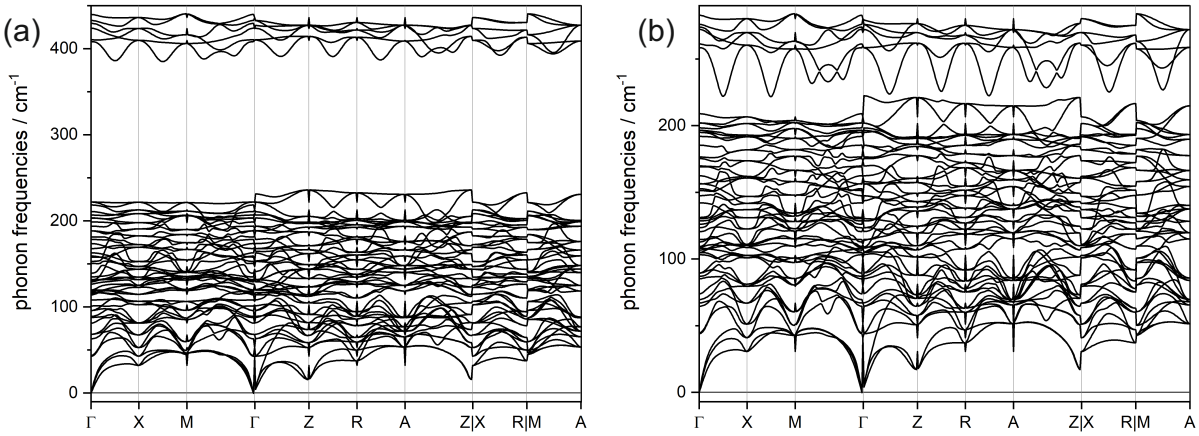

Figure A.13 Phonon dispersion of hypothetic (a) Na_4SiSe_4-$tP18$ and (b) Na_4GeSe_4-$tP18$ (Na_4SnS_4 structure type).

A.7 Impedance Spectroscopy

Table A.18 Resistances and capacities determined from fitted impedance spectra at 200 °C.

compound	R_1 / Ω	R_2 / Ω	C_1 / F	C_2 / F	CPE / F	α
Na_4SiSe_4-$oP36$	47×10^3		8×10^{-12}	103×10^{-12}	12×10^{-9}	0.38
Na_4SiSe_4-$cP72$	43×10^3		127×10^{-12}		20×10^{-9}	0.64
Na_4GeSe_4	18×10^3	6×10^6	120×10^{-12}		35×10^{-9}	0.62
Na_4SnSe_4-$tI216$	36×10^3		18×10^{-12}	114×10^{-12}		

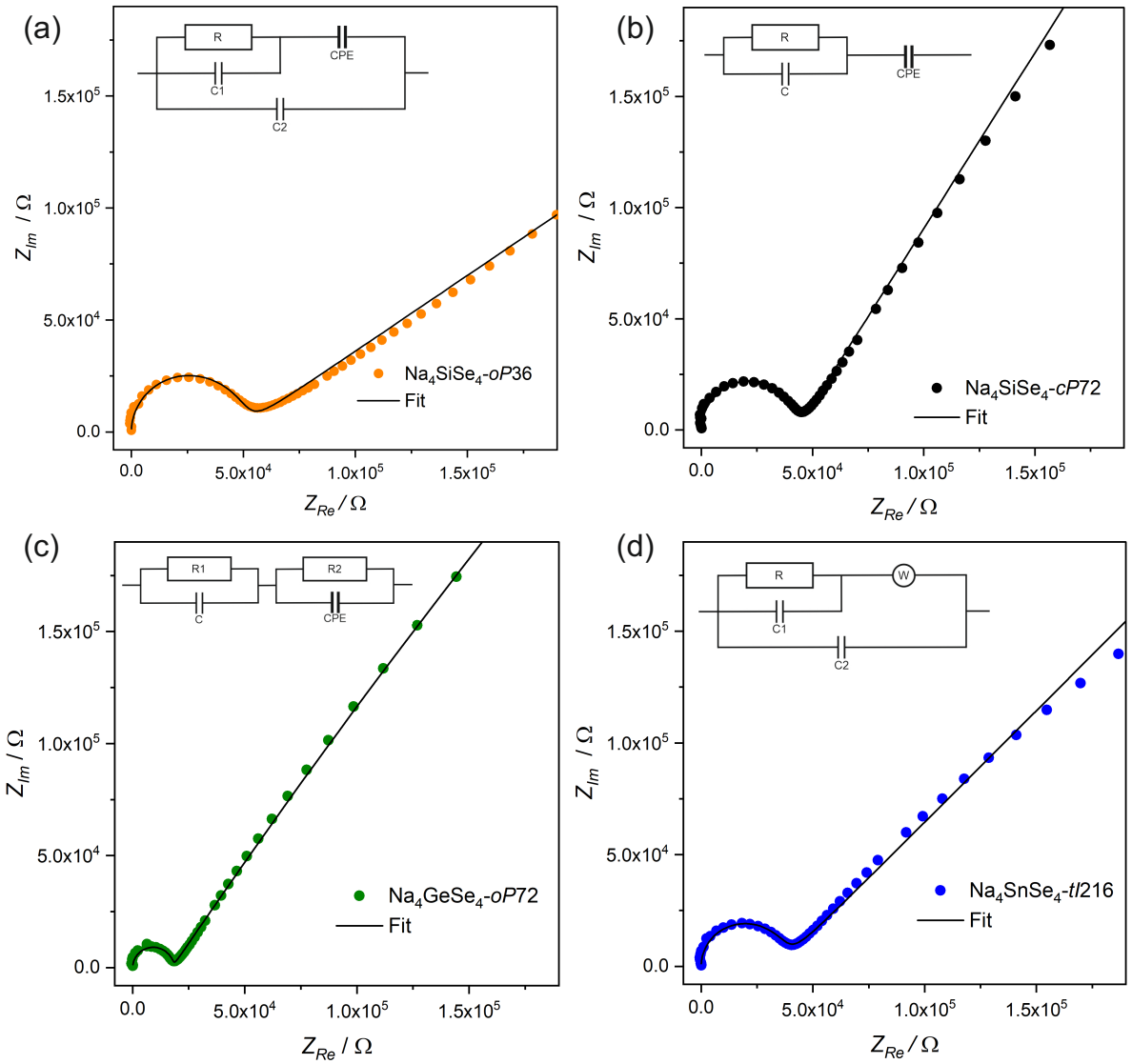

Figure A.14 Nyquist plots including fit at 200 °C for Na_4SiSe_4-*oP*36 (a), Na_4SiSe_4-*cP*72 (b), Na_4GeSe_4-*oP*72 (c) and Na_4SnSe_4-*tI*216 (d). The corresponding equivalent circuits for fitting of the Nyquist plots are also included.

References

[1] Preishuber-Pflügl, H.; Klepp, K. O. *Z. Kristallogr. - New Cryst. Struct.* **2003**, *218*, 383–384.

[2] Klepp, K. O. *Z. Naturforsch. B* **1985**, *40*, 878–882.

[3] Klepp, K. O. *Z. Naturforsch. B* **1992**, *47*, 411–417.

[4] Sophia, G.; Baranek, P.; Sarrazin, C.; Rerat, M.; Dovesi, R., `https://www.crystal.unito.it/Basis_Sets/sodium.html`, Accessed: 2023-03-06, 2014.

[5] Porter, A. R.; Towler, M. D.; Needs, R. J. *Phys. Rev. B* **1999**, *60*, 13534–13546.

[6] Heyd, J.; Peralta, J. E.; Scuseria, G. E.; Martin, R. L. *J. Chem. Phys.* **2005**, *123*, 174101.

[7] Causà, M.; Dovesi, R.; Roetti, C. *Phys. Rev. B* **1991**, *43*, 11937–11943.

[8] Towler, M. D.; Zicovich-Wilson, C., `https://vallico.net/mike_towler/crystal.html`, Accessed: 2023-03-06, 1995.

[9] Murnaghan, F. D. *Amer. J. Math.* **1937**, *59*, 235–260.

[10] Murnaghan, F. D. *Proc. Natl. Acad. Sci.* **1944**, *30*, 244–247.

[11] Birch, F. *Phys. Rev.* **1947**, *71*, 809–824.

B Supporting Information for Chapter 4

B.1 Synthesis

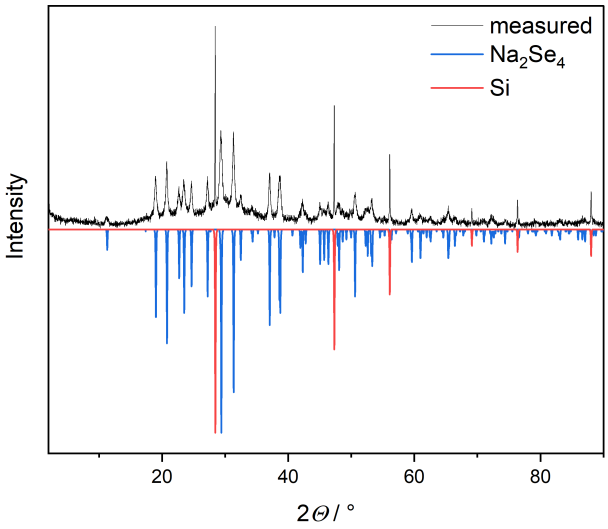

Figure B.1 X-ray powder diffraction pattern of the stochiometric mixture of Na, Si and Se after ball milling. For comparison, the calculated powder patterns of Na_2Se_4[1] and Si[2] are shown with negative intensities.

B.2 Crystal structure of $Na_4Si_2Se_6$-*tP*24

Table B.1 Crystallographic data and details of structure determination of $Na_4Si_2Se_6$-*tP*24.

chemical formula	$Na_4Si_2Se_6$
formula weight	$621.9\,g\,mol^{-1}$
crystal shape, color	block, yellow
size	$0.118 \times 0.056 \times 0.034$
T / K	300.0(1)
crystal system	tetragonal
space group	$P4_2/mcm$ (No.132)
a / Å	7.2793(2)
c / Å	12.4960(4)
V / $Å^3$	662.14(3)
formula units Z	2
calculated density ρ_{calc} / $g\,cm^{-3}$	3.1192
diffractometer	Rigaku Synergy DW
radiation	CuKα ($\lambda = 1.541\,84$ Å)
measurement method	ω - scan
measurement range Θ_{min} / Θ_{max}	6.08° / 73.97°
index range *hkl*	$-9 < h < 8$, $-8 < k < 8$, $-15 < l < 15$
measured / independent reflections (R_{int})	23411 / 393 (0.0364)
independent reflections [$I \geq 3\sigma(I)$]	377
completeness	0.99
absorption coefficient $\mu_{CuK\alpha}$	$22.201\,mm^{-1}$
absorption correction	gaussian
transmission T_{min}, T_{max}	0.218 / 0.623
structure solution	*Superflip*
structure refinement	*Jana2006*
data / restraints / parameter	393 / 0 / 23
goodness of fit	1.73
final R indexes [$I \geq 2\sigma(I)$]	1.62, 2.12
final R indexes [all data]	1.73, 2.16
$\Delta\rho_{min}$, $\Delta\rho_{max}$ / $e/Å^3$	-0.49, 0.26

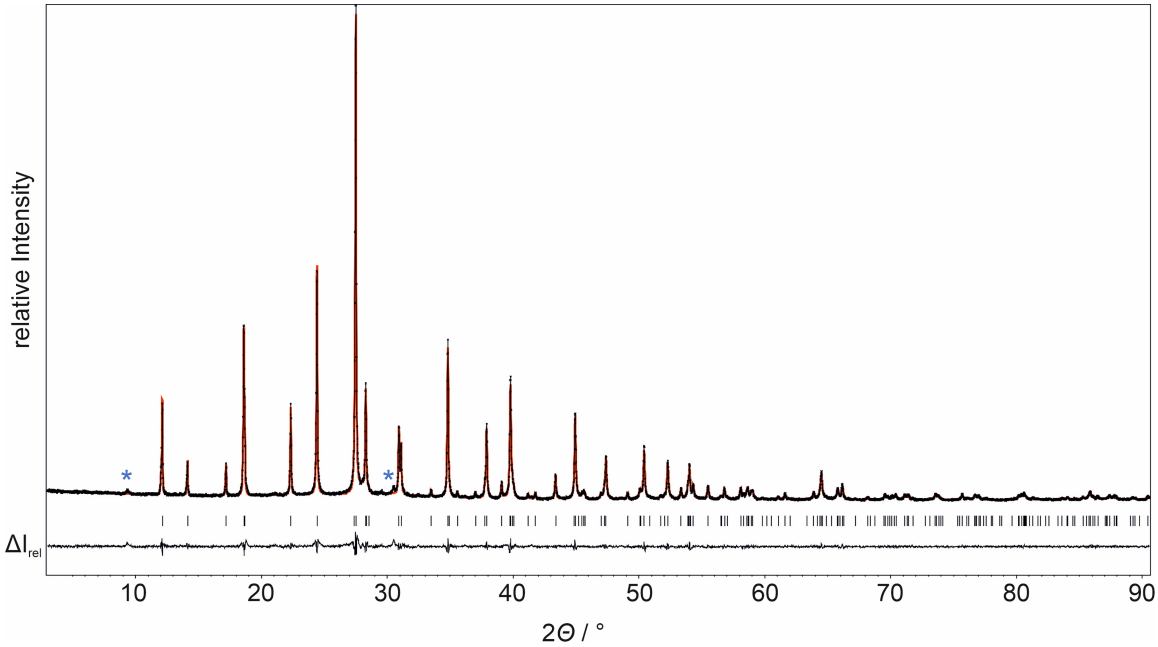

Figure B.2 Refined powder pattern of $Na_4Si_2Se_6$-*tP*24 with difference plot, measured with CuKα_1 radiation at room temperature. Unindexed reflections are marked with a blue star.

Table B.2 Refinement results from X-ray powder diffraction pattern of $Na_4Si_2Se_6$-*tP*24 compared to data from single crystal diffraction.

	XRPD	single crystal
a / Å	7.2783(1)	7.2793(2)
b / Å	12.5018(2)	12.4960(4)
V / Å^3	662.27(1)	662.14(3)
GOF	1.31	
R_P, wR_P, R_{exp}	0.0485, 0.0645, 0.0493	

Table B.3 Atomic positions and displacement parameters in $Na_4Si_2Se_6$-$tP24$ at room temperature.

	wyck. positions	x	y	z	U_{ani}
Na1	$2d$	1/2	1/2	1/4	0.0413(5)
Na2	$4e$	1/2	0	1/4	0.0555(7)
Na3	$2a$	0	0	0	0.0615(7)
Si	$4j$	0.6524(1)	1-x	0	0.0282(2)
Se1	$8o$	0.7708(1)	1-x	0.1483(1)	0.0364(1)
Se2	$4i$	0.3333(1)	x	0	0.0389(1)

Table B.4 Interatomic distances d in $Na_4Si_2Se_6$-$tP24$.

	d / Å
Si-Se1	2.2187(5)
Si-Se2	2.3247(2)
Na1-Se1	3.0635(3)
Na2-Se1	2.8781(3)
Na3-Se1	3.0006(3)
Na3-Se2	3.4314(3)

B.3 Crystal Structure of $Na_4Si_2Se_6$-*oP*48

Table B.5 Crystallographic data and details of structure determination of $Na_4Si_2Se_6$-*oP*48.

chemical formula	$Na_4Si_2Se_6$
formula weight	$621.9\,g\,mol^{-1}$
powder color	light grey
T / K	293
crystal system	orthorhombic
space group	*Pbca* (No. 61)
a / Å	12.9276(1)
b / Å	15.9324(1)
c / Å	6.0349(1)
V / Å^3	1243.00(2)
formula units Z	4
calculated density ρ_{calc} / $g\,cm^{-3}$	3.3232
diffractometer	STOE Stadi P, Debye-Scherrer geometry
radiation	CuKα_1 ($\lambda = 1.5406$ Å)
measurement range $2\Theta_{min}$ / $2\Theta_{max}$	3.0005° / 90.545°
2Θ step	0.015°
number of parameters / restraints	38 / 0
R_P, wR_P, R_{exp}	0.0490, 0.0617, 0.0421
goodness of fit	1.47
R_{gt}, wR_{gt} ($I > 3\sigma$)	0.0281, 0.0352
R_{all}, wR_{all}	0.0282, 0.0352
$\Delta\rho_{min}$, $\Delta\rho_{max}$ / e/Å^3	-0.60, 0.67

Table B.6 Atomic positions and displacement parameters in $Na_4Si_2Se_6$-$oP48$ at room temperature.

	wyck. position	x	y	z	U_{iso}
Na1	8c	0.5376(5)	0.1668(3)	0.502(1)	0.037(3)
Na2	8c	0.3563(5)	0.0274(4)	0.982(2)	0.050(2)
Si	8c	0.2402(4)	0.1715(2)	0.5338(7)	0.009(2)
Se1	8c	0.2835(1)	0.1970(1)	0.9072(3)	0.0198(7)
Se2	8c	0.0711(2)	0.1472(1)	0.4918(4)	0.0219(7)
Se3	8c	0.3457(1)	0.0656(1)	0.4642(3)	0.0185(7)

Table B.7 Interatomic distances d in $Na_4Si_2Se_6$-$oP48$.

	d / Å
Si-Se1	2.301(4)
Si-Se2	2.235(5)
Si-Se3	2.209(5)
Na1-Se2	2.995(5)
Na1-Se2	3.030(7)
Na1-Se3	2.968(6)
Na2-Se1	2.896(6)
Na2-Se2	2.937(6)
Na2-Se3	2.975(9)
Na2-Se3	3.005(6)
Na2-Se3	3.373(7)

B.4 Calculation details

B.4.1 Basis sets

Basis sets were taken from literature.[3–5] All basis sets are available in the basis set library at the Crystal homepage. The outer shells were then adjusted so that the calculated energy was minimized. The basis sets used are as followed:

Table B.8 Na basis set optimized for $Na_4Si_2Se_6$-$tP24$.

Na	exponent	contraction coefficient
1s	56700	0.000225
	8060	0.00191
	1704	0.0105
	443.6	0.05006
	133.1	0.1691
	45.8	0.3658
	17.75	0.3998
	7.38	0.1494
2sp	119.0	s: -0.00673 p:0.00803
	25.33	s: -0.0798 p: 0.0639
	7.80	s: -0.0793 p: 0.2074
	3.00	s: 0.3056 p: 0.3398
	1.289	s: 0.5639 p: 0.3726
3sp	0.5437	s: 1.0 p: 1.0
4sp	0.1355	s: 1.0 p: 1.0
3d	0.1	1.0

Table B.9 Si basis set optimized for $Na_4Si_2Se_6$-$tP24$.

Si	exponent	contraction coefficient
$1s$	149866	0.0001215
	22080.6	0.0009770
	4817.5	0.0055181
	1273.5	0.0252
	385.11	0.0926563
	128.429	0.2608729
	45.4475	0.4637538
	16.2589	0.2952
$2sp$	881.111	s: -0.0003 p: 0.0006809
	205.840	s: -0.005 p: 0.0059446
	64.8552	s: -0.0368 p: 0.0312
	23.9	s: -0.1079 p: 0.1084
	10.001	s: 0.0134 p: 0.2387
	4.4722	s: 0.3675 p: 0.3560066
	2.034	s: 0.5685 p: 0.341
	0.9079	s: 0.2065 p: 0.1326
$3sp$	3.7087	s: 1.0 p: 1.0
$4sp$	1.0537	s: 1.0 p: 1.0
$5sp$	0.3851	s: 1.0 p: 1.0
$6sp$	0.1659	s: 1.0 p: 1.0
$3d$	0.3054	1.0

Table B.10 Se basis set optimized for $Na_4Si_2Se_6$-*tP*24.

Se	exponent	contraction coefficient
1*s*	2275090.0	0.000038
	319959.0	0.0003344
	64974.1	0.0021238
	15718.0	0.011193
	4347.15	0.047900
	1367.7	0.157400
	483.334	0.352332
	187.066	0.423303
	75.1333	0.153645
2*sp*	5241.62	*s*: -0.000373 *p*: 0.0009764
	1192.97	*s*: -0.0072305 *p*: 0.0092853
	354.263	*s*: -0.061887 *p*: 0.056735
	121.56	*s*: -0.145788 *p*: 0.218068
	46.765	*s*: 0.246071 *p*: 0.447931
	19.7469	*s*: 0.712463 *p*: 0.395229
	8.44148	*s*: 0.239375 *p*: 0.09678
3*sp*	103.375	*s*: 0.0039064 *p*:-0.014826
	36.4438	*s*: -0.054067 *p*: -0.071387
	15.4097	*s*: -0.323251 *p*: 0.116639
	6.326	*s*: 0.264172 *p*: 0.970063
	2.62943	*s*: 0.954686 *p*: 1.21262
	1.04921	*s*: 0.236846 *p*: 0.328426
3*d*	202.635	0.005270
	59.7021	0.04036
	21.5166	0.162038
	8.3345	0.368724
	3.15228	0.46438
4*d*	1.0552	1.0
4*sp*	2.318094	*s*: -0.908900 *p*: -0.1759
	0.945900	*s*: -0.595800 *p*: 0.5555
	0.409815	*s*: 3.163300 *p*: 2.8121
5*d*	0.1421	1.0

B.4.2 Testing of different functionals

Table B.11 Energy difference $\Delta E = E_{tP24}$ - E_{oP48} depending on the chosen functional and experimental and calculated lattice parameters.

Functional		a / Å	b / Å	c / Å	V / Å^3	$\Delta E/Z$ / kJ mol^{-1}
exp	$tP24$	7.2793(2)		12.4960(4)	662.14(3)	
	$oP48$	12.9276(1)	15.9323(1)	6.0349(1)	1243.00(2)	
PBE	$tP24$	7.36081		12.5393	679.40	
	$oP48$	13.0649	16.1346	6.0587	1277.15	-5.8
PBE0	$tP24$	7.3212		12.5473	672.54	
	$oP48$	13.0596	16.0009	6.0158	1257.09	-4.5
HSE06	$tP24$	7.3238		12.5467	672.98	
	$oP48$	13.0601	16.0112	6.01984	1258.79	-3.4
PBEsol	$tP24$	7.2542		12.2588	645.10	
	$oP48$	12.7956	15.8695	5.9513	1208.46	7.1
PBE-D3	$tP24$	7.1732		12.2114	628.33	
	$oP48$	12.6556	15.6660	5.9328	1176.25	15.2
LDA	$tP24$	7.0958		12.0535	606.89	
	$oP48$	12.5377	15.5052	5.8580	1138.78	19.9

B.4.3 DOS and COHP

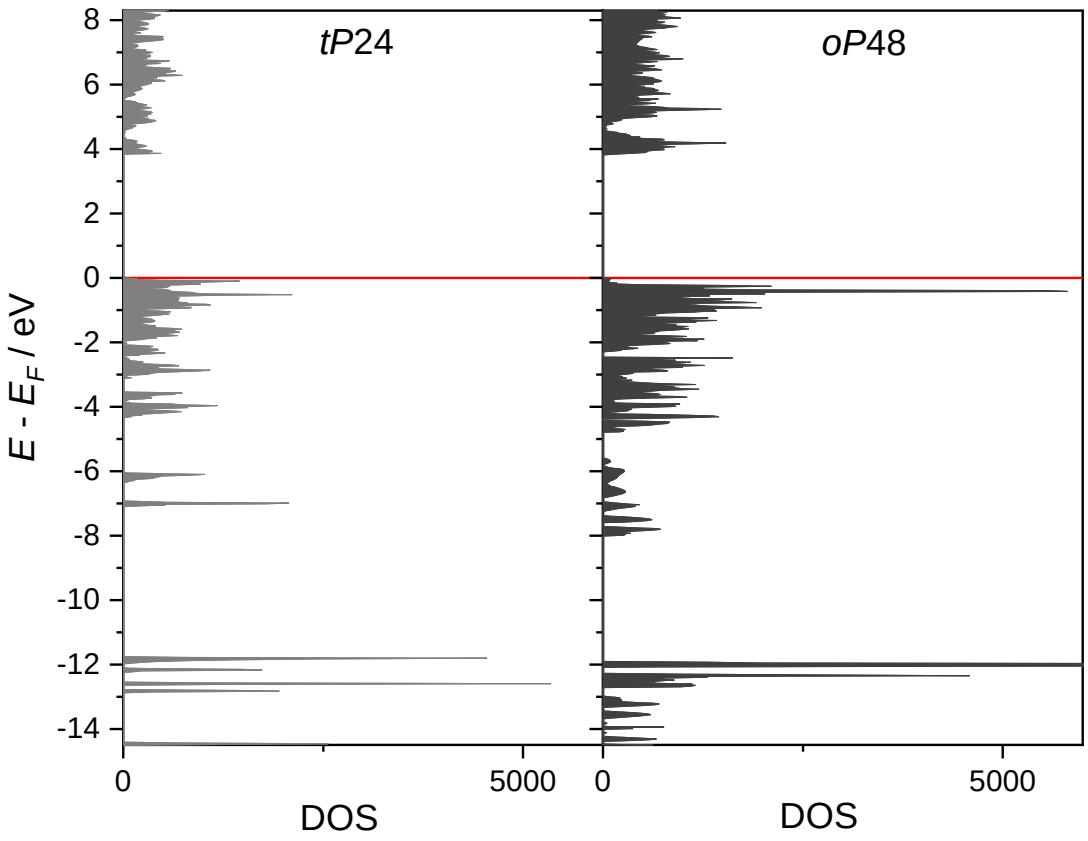

Figure B.3 Calculated DOS for $Na_4Si_2Se_6$-*tP*24 and $Na_4Si_2Se_6$-*oP*48.

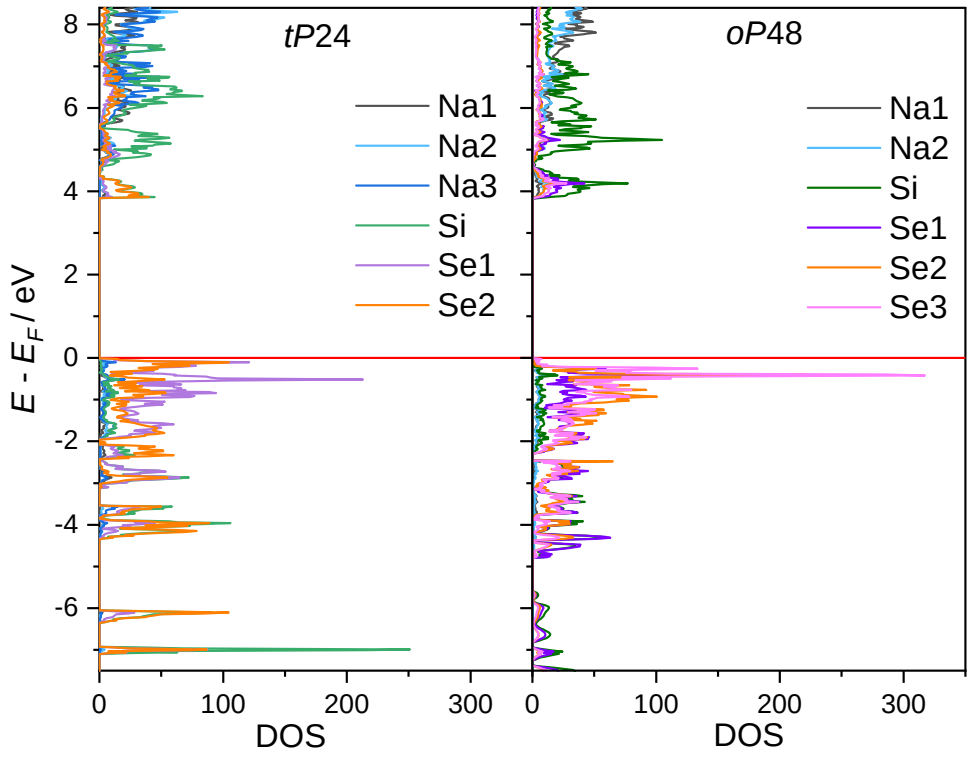

Figure B.4 Calculated atomic site projected DOS for $Na_4Si_2Se_6$-*tP*24 and $Na_4Si_2Se_6$-*oP*48.

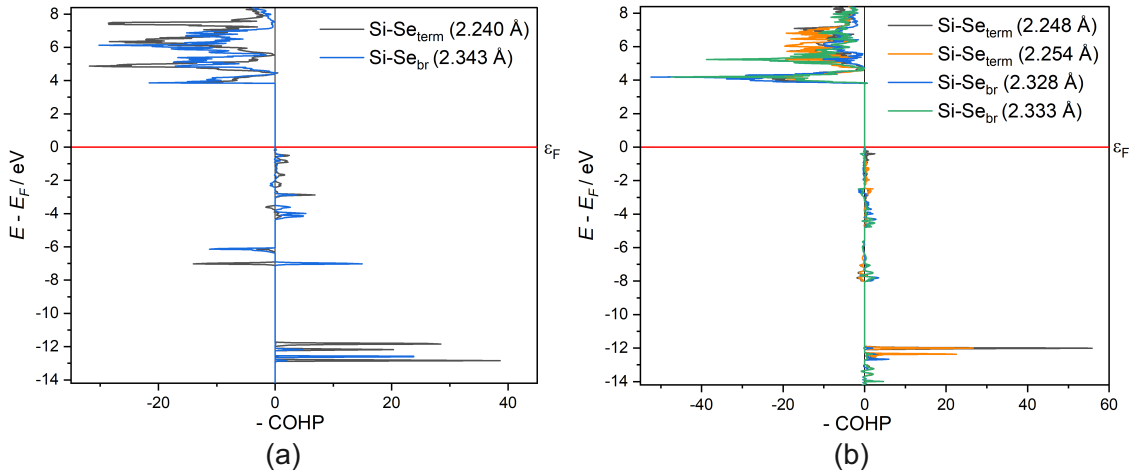

Figure B.5 Calculated Crystal Orbital Hamiltonian Population (COHP) for Si - Se interactions in (a) $Na_4Si_2Se_6$-*tP*24 and (b) $Na_4Si_2Se_6$-*oP*48.

B.4.4 Equation of State calculations

The calculated E and V values were fitted with the Birch-Murnaghan EOS[6–8] (equation 1).

$$E(V) = E_0 + \frac{9V_0B_0}{16}\left\{\left[\left(\frac{V_0}{V}\right)^{\frac{2}{3}} - 1\right]^3 B_0' + \left[\left(\frac{V_0}{V}\right)^{\frac{2}{3}} - 1\right]^2 \left[6 - 4\left(\frac{V_0}{V}\right)^{\frac{2}{3}}\right]\right\} \quad \text{(B.1)}$$

Table B.12 Fit data for Birch-Murnaghan EOS.

Polymorph	B_0 / GPa	B_0'
$Na_4Si_2Se_6$-$tP24$	19.5	4.5
$Na_4Si_2Se_6$-$oP48$	20.7	4.5

B.4.5 Possible other structure types

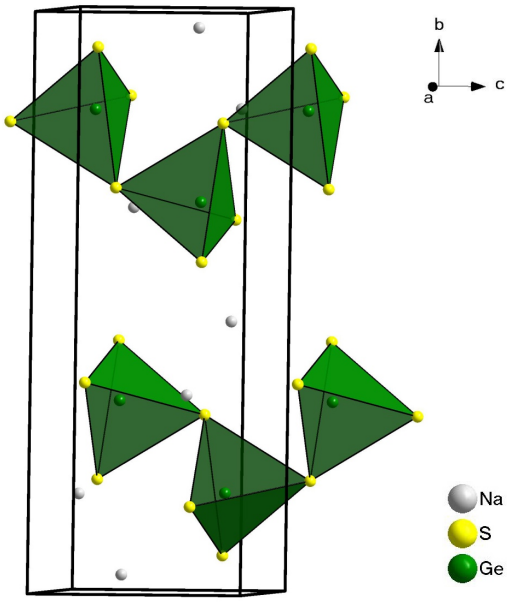

Figure B.6 Unit cell of $Na_4Ge_2S_6$ with corner-sharing GeS_4-tetrahedra forming zweiersingle chains.[9]

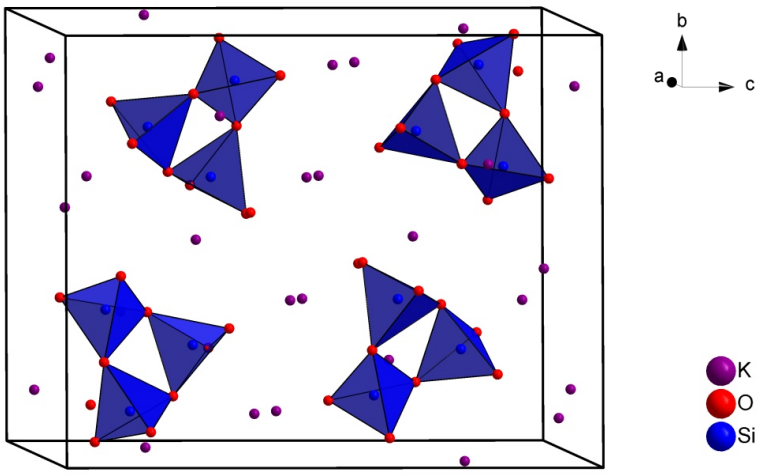

Figure B.7 Unit cell of $K_6Si_3O_9$ with corner-sharing SiO_4-tetrahedra forming rings.[10]

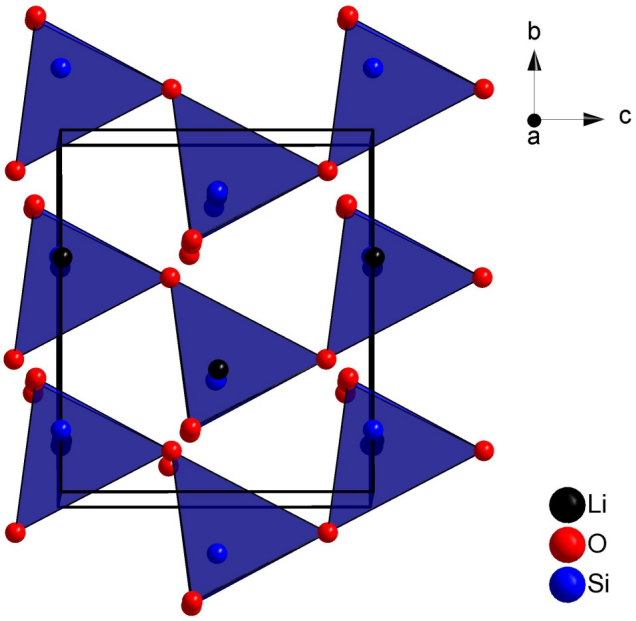

Figure B.8 Unit cell of $Li_4Si_2O_6$ with corner-sharing SiO_4-tetrahedra forming zweiersingle chains.[11]

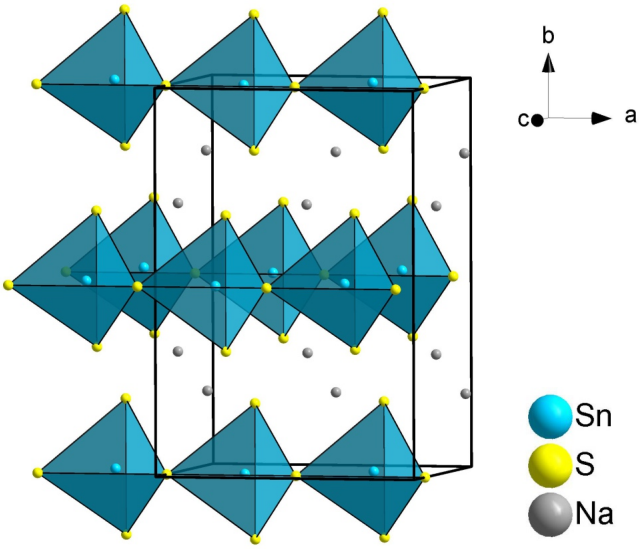

Figure B.9 Unit cell of $Na_4Sn_2S_6$ with corner-sharing SnS_4-tetrahedra forming nearly linear zweiersingle chains.[12]

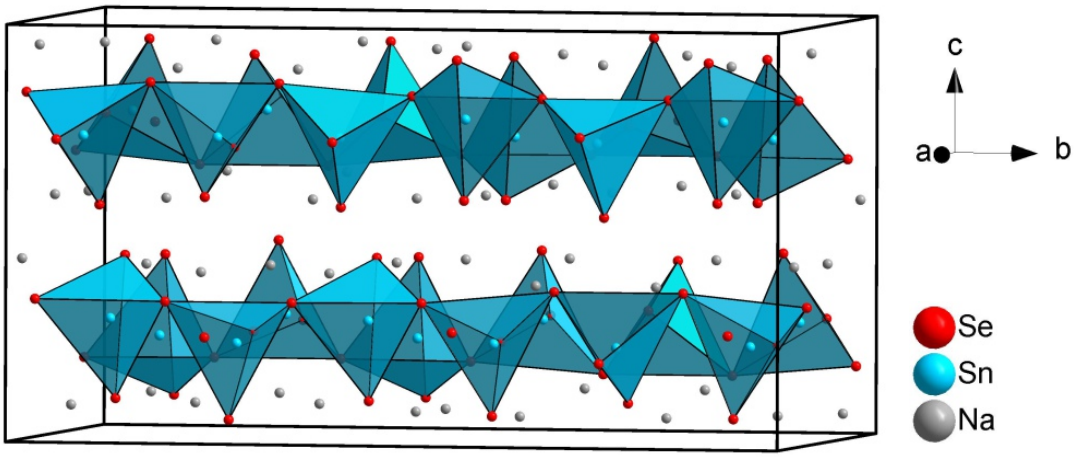

Figure B.10 Unit cell of $Na_6Sn_3Se_{12}$ with corner-sharing $SnSe_4$-tetrahedra forming sechsersingle chains.[13]

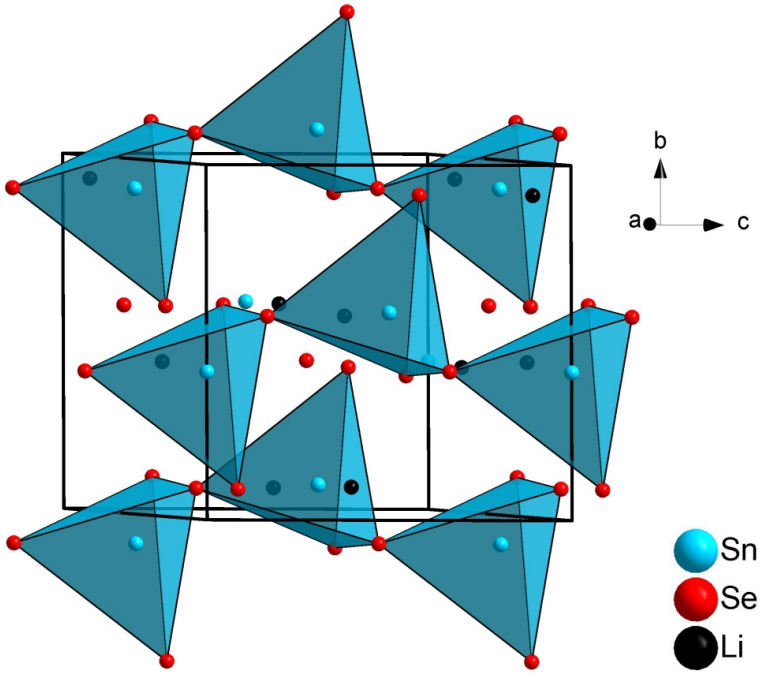

Figure B.11 Unit cell of $Li_4Sn_2Se_6$ with corner-sharing $SnSe_4$-tetrahedra forming zweiersingle chains.[14]

B.4.6 MAPLE calculations

Table B.13 Results of MAPLE calculations for $Na_4Si_2Se_6$-*tP*24.

atom	MAPLE
Na1	55.1439
Na2	123.5923
Na3	130.6464
Se1	428.6121
Se2	544.8478
Si	1409.3964
Madelung	40.4945
Coulomb part of lattice energy / $kJ\,mol^{-1}$	2530.0524

Table B.14 Results of MAPLE calculations for $Na_4Si_2Se_6$-*oP*48.

atom	MAPLE
Na1	103.2805
Na2	122.8929
Se1	532.6358
Se2	439.9007
Se3	416.5732
Si	1409.7225
Madelung	20.6838
Coulomb part of lattice energy / $kJ\,mol^{-1}$	13001.7427

B.5 High pressure experiments

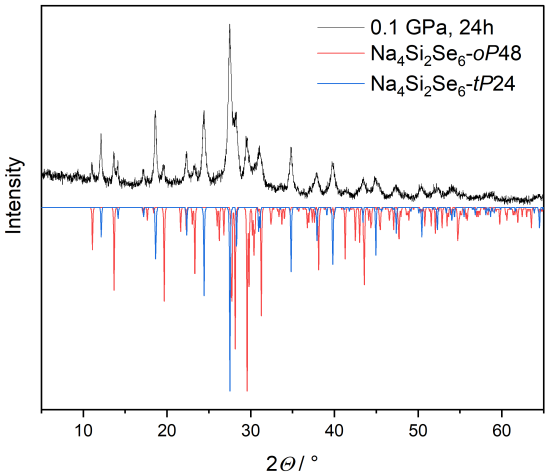

Figure B.12 X-ray powder diffraction pattern after application of a pressure of $P = 0.1\,\mathrm{GPa}$ for 24 h on a sample of $Na_4Si_2Se_6$-$tP24$. Calculated patterns of $Na_4Si_2Se_6$-$tP24$ (blue) and $Na_4Si_2Se_6$-$oP48$ (red) are shown with negative intensities.

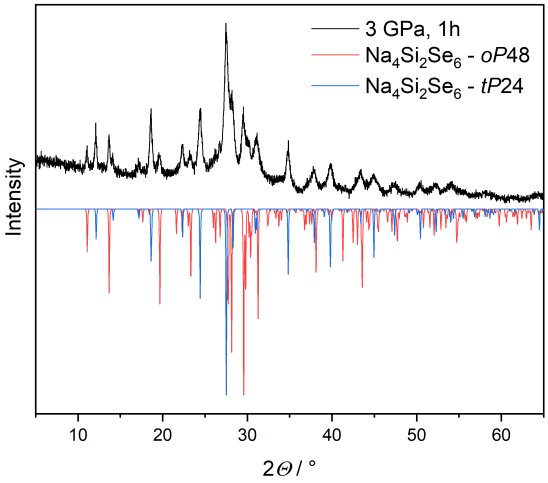

Figure B.13 X-ray powder diffraction pattern after application of a pressure of $P = 3\,\mathrm{GPa}$ for 1 h on a sample of $Na_4Si_2Se_6$-$tP24$. Calculated patterns of $Na_4Si_2Se_6$-$tP24$ (blue) and $Na_4Si_2Se_6$-$oP48$ (red) are shown with negative intensities.

B.6 Impedance Spectroscopy

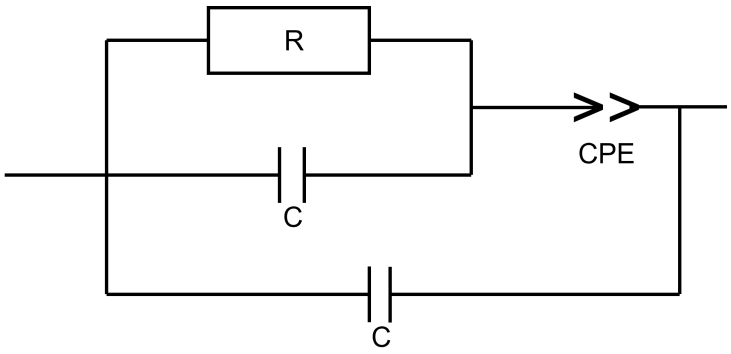

Figure B.14 Equivalent circuit used for fitting of Nyquist plots.

B.7 Differential Thermal Analysis (DTA)

DTA measurements were carried out using a SETARAM TG-DTA 92.16.18. Both samples were analyzed up to 900 °C.

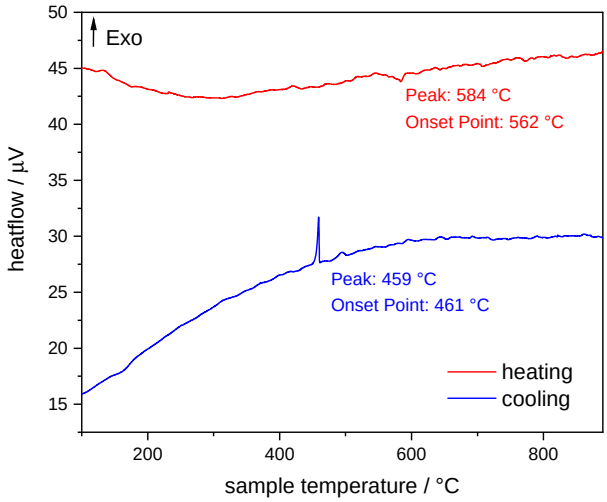

Figure B.15 DTA curve of a sample of $Na_4Si_2Se_6$-*tP*24 (heating/ cooling rate 5 °C min^{-1}). The peaks at 562 °C in the heating cycle and 461 °C in the cooling cycle can be assigned to the phase transition from the high temperature polymorph to the low temperature polymorph. The corresponding reaction from low temperature to high temperature polymorph is not clearly visible.

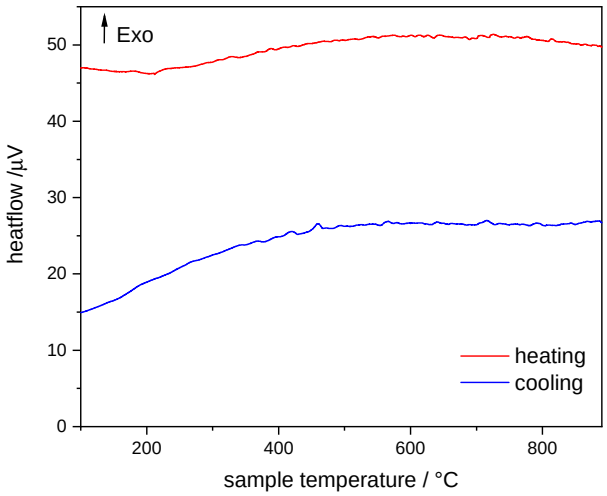

Figure B.16 DTA curves of a sample of $Na_4Si_2Se_6$-*oP*48 (heating/ cooling rate $5\,^{\circ}C\,min^{-1}$). Multiple small effects which can not be clearly assigned to the phase transition are visible.

References

[1] Getzschmann, J.; Rönsch, E.; Böttcher, P. *Z. Kristallogr. - New Cryst. Struct.* **1997**, *212*, 87–87.

[2] Straumanis, M. E.; Aka, E. Z. *J. Appl. Phys.* **1952**, *23*, 330–334.

[3] Sophia, G.; Baranek, P.; Sarrazin, C.; Rerat, M.; Dovesi, R., `https://www.crystal.unito.it/Basis_Sets/sodium.html`, Accessed: 2023-03-06, 2014.

[4] Porter, A. R.; Towler, M. D.; Needs, R. J. *Phys. Rev. B* **1999**, *60*, 13534–13546.

[5] Towler, M. D.; Zicovich-Wilson, C., `https://vallico.net/mike_towler/crystal.html`, Accessed: 2023-03-06, 1995.

[6] Murnaghan, F. D. *Amer. J. Math.* **1937**, *59*, 235–260.

[7] Murnaghan, F. D. *Proc. Natl. Acad. Sci.* **1944**, *30*, 244–247.

[8] Birch, F. *Phys. Rev.* **1947**, *71*, 809–824.

[9] Eisenmann, B.; Hansa, J.; Schäfer, H. *Z. Naturforsch. B* **1985**, *40*, 450–457.

[10] Werthmann, R. et al. *Rev. Chim. Minér.* **1981**, *18*, 593–607.

[11] Seemann, H. *Acta Crystallogr.* **1956**, *9*, 251–252.

[12] Benkada, A.; Hartmann, F.; Poschmann, M.; Indris, S.; Lühmann, H.; Bensch, W. *Eur. J. Inorg. Chem.* **2023**, *26*, e202200687.

[13] Eisenmann, B.; Hansa, J. *Z. Kristallogr. - Cryst. Mater.* **1993**, *203*, 291–292.

[14] Kaib, T.; Bron, P.; Haddadpour, S.; Mayrhofer, L.; Pastewka, L.; Järvi, T. T.; Moseler, M.; Roling, B.; Dehnen, S. *Chem. Mater.* **2013**, *25*, 2961–2969.

C Supporting Information for Chapter 5

C.1 Na_4SiTe_4

Table C.1 Crystallographic data and details of structure determination of Na_4SiTe_4.

chemical formula	Na_4SiTe_4
powder color	yellow
T / K	293
crystal system	cubic
space group	$Pa\bar{3}$ (No. 205)
a / Å	13.0312(5)
V / Å^3	2212.84(2)
formula units Z	8
calculated density ρ_{calc} / g cm^{-3}	3.7847
diffractometer	STOE Stadi P, Debye-Scherrer geometry
radiation	MoKα ($\lambda = 0.709\,30$ Å)
measurement range $2\Theta_{\min}$ / $2\Theta_{\max}$	2.000° / 61.385°
2Θ step	0.015°
number of parameters / restraints	19 / 0
R_P, wR_P, R_{exp}	0.0422, 0.0567, 0.0326
goodness of fit	1.74
R_{gt}, wR_{gt} ($I > 3\sigma$)	0.0408, 0.0469
R_{all}, wR_{all}	0.0447, 0.0476
$\Delta\rho_{min}$, $\Delta\rho_{max}$ / e/Å^3	-1.36, 1.15

Table C.2 Atomic coordinates and isotropic displacement parameters for Na_4SiTe_4.

atom	wyck. position	x	y	z	U_{eq} / Å^2
Na1	24d	0.7370(7)	0.2987(4)	0.4850(8)	0.048(2)
Na2	4a	0	0	0	0.04(1)
Na3	4b	1/2	1/2	1/2	0.04(1)
Si	8c	0.6372(4)	x	x	0.014(2)
Te1	24d	0.7490(1)	0.54036(5)	0.51226(7)	0.0260(3)
Te2	8c	0.7456(1)	x	x	0.0275(5)

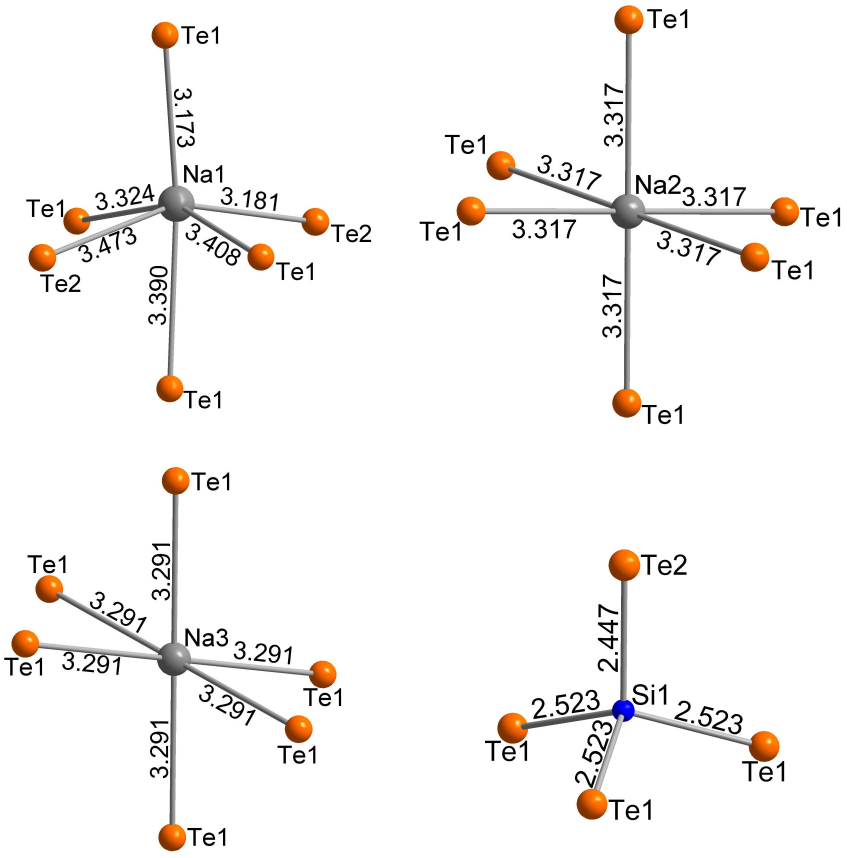

Figure C.1 Coordination polyhedra of Na and Si in Na_4SiTe_4 with distances in Å.

C.2 $Na_{10}Si_2Te_9$

C.2.1 Structure Determination from Single Crystal X-ray Diffraction

Due to various problems during the structure determination of $Na_{10}Si_2Te_9$ several different crystals were measured at different temperatures and two different diffractometers (Rigaku SuperNova and Rigaku Synergy, DW systems) to exclude artifacts from bad crystal quality of individual crystals.

All determined structure models show rather high residual electron densities and R values are higher than expected. This can have various reasons, e.g. the assumed symmetry is higher than the real symmetry or the measured data is affected by twinning which is leading to a wrong crystal structure.

The measured reflections can be indexed with a unit cell with orthorhombic metric. In all cases, more than 90 % of the reflections can be indexed. The measured diffraction pattern was also checked for twinning by the twin unit cell finding algorithm which is implement in *CrysAlisPro*,[1] but only small parts of unindexed reflections can be indexed to a second unit cell with the same lattice dimensions.

The orthorhombic metric, the statistics of $E^2 - 1$ and the observed absence conditions lead to the centrosymmetric space group *Pbcn* (No. 60). A structure model with both isolated $[SiTe_4]^{4-}$ tetrahedra and isolated Te^{2-} units with the composition $Na_{10}Si_2Te_9$ or $Na_{10}(SiTe_4)_2Te$, respectively was obtained from structure solution with direct methods. Though the structure model seems reasonable from a chemical point of view, the structure refinement was not entirely satisfactory. The resulting crystal structure exhibits high residual electron density around Te with distances less than 1 Å and converges with unexpected high R values. The crystallographic data and details of structure determination are shown in Table C.2, exemplary for one of the analyzed crystals. Additionally, the structures exhibits some splitted sodium positions with a reduced occupancy of 50 % and short interatomic distances.

By refinement as inversion twin in space group $Pna2_1$ (No. 33), which is a subgroup of *Pbcn*, the suspicious sodium positions can be resolved to fully occupied positions with coordination spheres as expected. Also the R values dropped to more reasonable values. Besides that, the residual electron density remains higher as can be expected. The resulting crystallographic data and details of the structure determination are listed in Table C.3. Note that all given data (refinement in *Pbcn* and $Pna2_1$) stems from the same measurement data.

To solve the problematic residual electron density (Figure C.5), different further orthorhombic, monoclinic and triclinic space groups were tested. Also various twinning options did not lead to reasonable structure solutions.

Figure C.2 Crystallographic data and details of structure determination of $Na_{10}Si_2Te_9$ from single crystal X-ray diffraction in the centrosymmetric space group *Pbcn*.

chemical formula	$Na_{10}Si_2Te_9$
chemical formula weight / $g\,mol^{-1}$	1434.5
crystal color	red
T / K	100.1(4)
crystal system	orthorhombic
space group	*Pbcn* (No. 60)
a / Å	12.9530(7)
b / Å	14.8399(8)
c / Å	12.8235(7)
V / $Å^3$	2464.9(2)
formula units Z	4
calculated density ρ_{calc} / $g\,cm^{-3}$	3.8654
diffractometer	Rigaku XtaLAB Synergy R, DW system, HyPix-Arc 150
radiation	MoKα ($\lambda = 0.710\,73$ Å)
measurement method	ω - scans
measurement range $2\Theta_{min}$ / $2\Theta_{max}$	2.09° / 39.85°
index range *hkl*	-21 < h < 23, -26 < k < 24, -22 < l < 22
measured / independent reflections (R_{int})	66640 / 7335 (0.0332)
absorption coefficient $\mu_{MoK\alpha}$	$10.746\,mm^{-1}$
absorption correction	gaussian
transmission T_{min}, T_{max}	0.622 / 0.764
structure solution	*Superflip*
structure refinement	*Jana2006*
data / restraints / parameter	7335 / 0 / 105
goodness of fit	2.95
final R, wR [$I \geq 2\sigma(I)$]	4.60, 10.60
final R, wR [all data]	5.62, 10.71
$\Delta\rho_{min}$, $\Delta\rho_{max}$ / $e/Å^3$	-5.94, 9.93

Table C.3 Crystallographic data and details of structure determination of $Na_{10}Si_2Te_9$ from single crystal X-ray diffraction in space group $Pna2_1$.

chemical formula	$Na_{10}Si_2Te_9$
chemical formula weight / $g\,mol^{-1}$	1434.5
crystal color	red
T / K	100.1(4)
crystal system	orthorhombic
space group	$Pna2_1$ (No. 33)
a / Å	12.8235(7)
b / Å	14.8398(8)
c / Å	12.9530(7)
V / $Å^3$	2464.9(2)
formula units Z	4
calculated density ρ_{calc} / $g\,cm^{-3}$	3.8654
diffractometer	Rigaku XtaLAB Synergy R, DW system, HyPix-Arc 150
radiation	MoKα ($\lambda = 0.710\,73$ Å)
measurement method	ω - scans
measurement range $2\Theta_{min}$ / $2\Theta_{max}$	2.09° / 39.85°
index range *hkl*	-23 < h < 21, -26 < k < 24, -22 < l < 22
measured / independent reflections (R_{int})	67682 / 11789 (0.0294)
absorption coefficient $\mu_{MoK\alpha}$	$10.746\,mm^{-1}$
absorption correction	gaussian
transmission T_{min}, T_{max}	0.614 / 0.747
structure solution	*Superflip*
structure refinement	*Jana2006*
data / restraints / parameter	14472 / 0 / 190
goodness of fit	1.65
final R, wR [$I \geq 2\sigma(I)$]	3.23, 6.62
final R, wR [all data]	4.37, 6.79
$\Delta\rho_{min}$, $\Delta\rho_{max}$ / $e/Å^3$	-4.93, 8.06

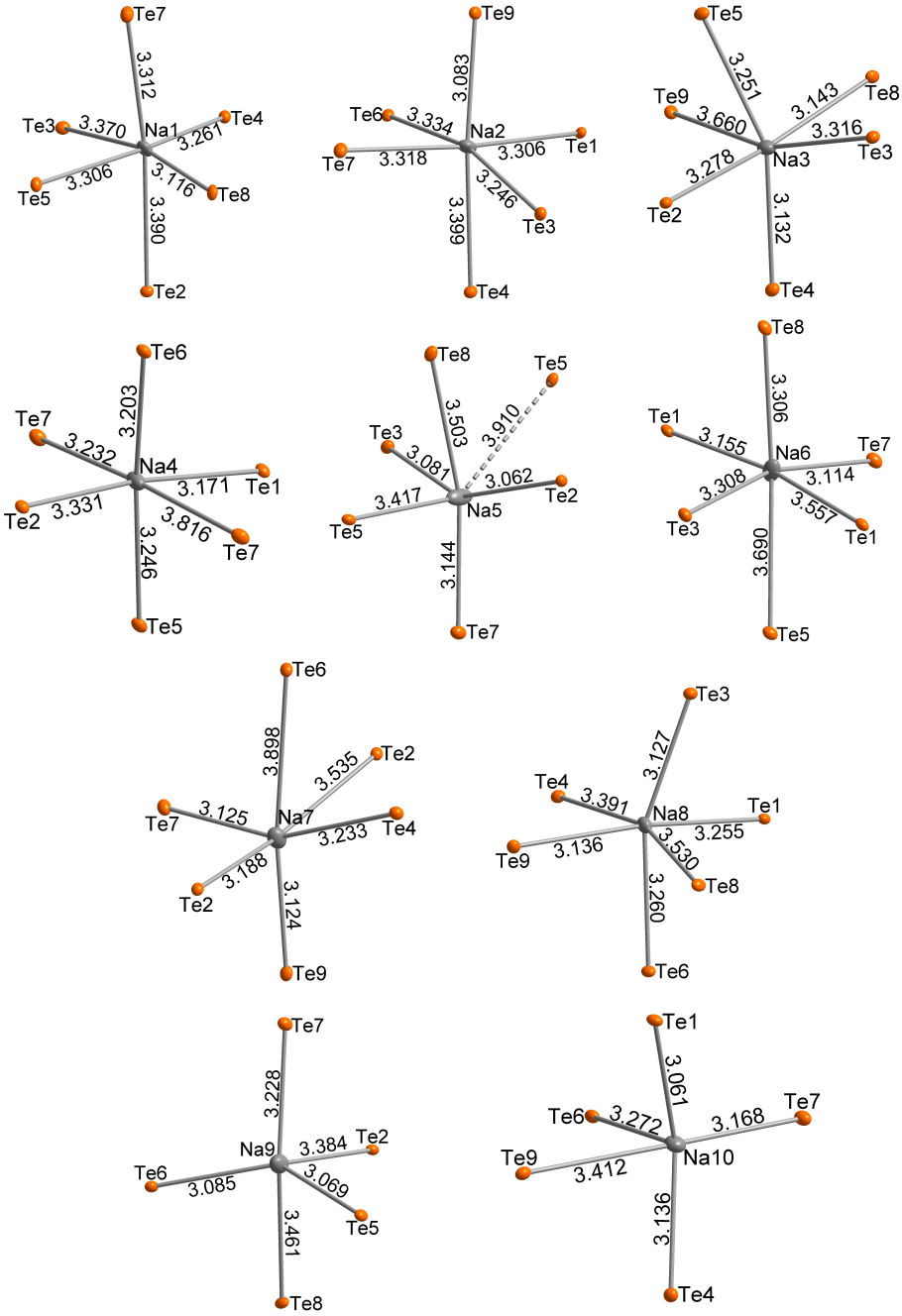

Figure C.3 Coordination polyhedra of Na in $Na_{10}Si_2Te_9$ with distances in Å.

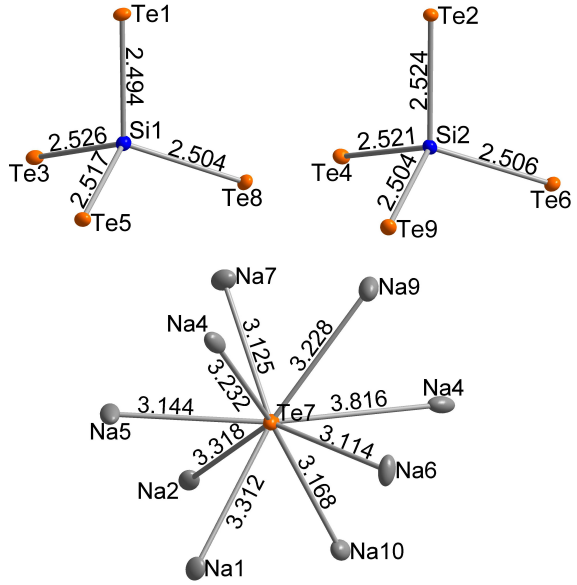

Figure C.4 Coordination polyhedra of Si and Te9 in $Na_{10}Si_2Te_9$ with distances in Å.

Table C.4 EDX analysis of crystalline $Na_{10}Si_2Te_9$. The analysis confirms the composition determined from X-ray diffraction experiments, which corresponds to 47.62 atom-% for Na, 9.52 atom-% for Si and 42.86 atom-% for Te.

element	mass norm. /%	atom-%	abs. error / %	rel. error / %
Na	15.73	46.68	0.96	6.36
Si	4.36	10.58	0.20	4.78
Te	79.92	42.73	2.28	2.96

Table C.5 Atomic coordinates and isotropic displacement parameters for $Na_{10}Si_2Te_9$ from single crystal X-ray diffraction.

atom	wyck. position	x	y	z	U_{eq} / Å^2
Na1	4a	0.1682(2)	0.4751(2)	-0.3719(3)	0.0167(8)
Na2	4a	-0.1654(2)	0.0285(2)	0.3684(3)	0.0179(8)
Na3	4a	0.0839(3)	0.6406(2)	-0.9438(3)	0.0197(9)
Na4	4a	-0.0242(2)	1.2537(2)	0.0043(2)	0.0206(6)
Na5	4a	0.0650(3)	0.5454(2)	-0.6053(3)	0.030(1)
Na6	4a	-0.2251(3)	-0.2388(2)	0.7128(2)	0.0234(8)
Na7	4a	0.2248(3)	0.7251(2)	-0.7294(3)	0.0219(7)
Na8	4a	-0.0903(2)	-0.1406(2)	0.9419(3)	0.0163(8)
Na9	4a	-0.2174(2)	-0.3650(2)	0.4565(2)	0.0254(7)
Na10	4a	-0.0591(2)	-0.0481(2)	0.5971(3)	0.0178(8)
Si1	4a	0.5071(2)	0.8490(1)	-0.2217(2)	0.0101(5)
Si2	4a	-0.5072(2)	-0.3510(1)	0.2242(1)	0.0089(5)
Te1	4a	0.5450(1)	0.6883(1)	-0.2636(1)	0.0093(1)
Te2	4a	-0.5476(1)	-0.1886(1)	0.2662(1)	0.0086(1)
Te3	4a	0.3678(1)	0.8470(1)	-0.0837(1)	0.0108(1)
Te4	4a	-0.3696(1)	-0.3462(1)	0.0854(1)	0.0099(1)
Te5	4a	0.4350(1)	0.9301(1)	-0.3767(1)	0.0101(1)
Te6	4a	-0.4327(1)	-0.4288(1)	0.3793(1)	0.0096(1)
Te7	4a	0.2511(1)	0.6518(1)	-0.5047(1)	0.0127(1)
Te8	4a	0.6665(1)	0.9289(1)	-0.1580(1)	0.0102(1)
Te9	4a	-0.6635(1)	-0.4334(1)	0.1568(1)	0.0102(1)

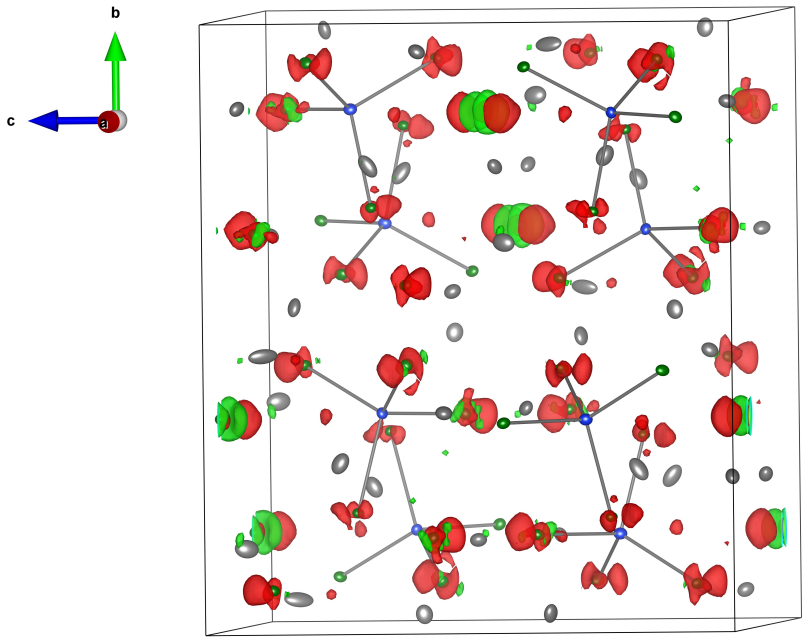

Figure C.5 Difference Fourier map (F(obs)-F(calc)) with residual electron density near Te. For rendering a isosurface level of 1.2 was used.

C.2.2 Structure Determination from Powder X-ray Diffraction

Table C.6 Crystallographic data and details of structure determination of $Na_{10}Si_2Te_9$ from powder X-ray diffraction.

chemical formula	$Na_{10}Si_2Te_9$
powder color	orange
T / K	293
crystal system	orthorhombic
space group	$Pna2_1$ (No. 33)
a / Å	12.9790(2)
b / Å	14.9308(2)
c / Å	13.0670(1)
V / Å^3	2532.21(5)
formula units Z	4
calculated density ρ_{calc} / g cm^{-3}	3.7627
diffractometer	STOE Stadi P, Debye-Scherrer geometry
radiation	MoKα (λ = 0.7093 Å)
measurement range $2\Theta_{\min}$ / $2\Theta_{\max}$	2.000° / 50.585°
2Θ step	0.015°
number of parameters / restraints / constraints	53 / 0 / 11
R_P, wR_P, R_{exp}	0.0211, 0.0272, 0.0139
goodness of fit	1.96
R_{gt}, wR_{gt} ($I > 3\sigma$)	0.0224, 0.0292
R_{all}, wR_{all}	0.0225, 0.0293
$\Delta\rho_{min}$, $\Delta\rho_{max}$ / e/Å^3	-0.61, 0.61

Table C.7 Atomic coordinates and isotropic displacement parameters for $Na_{10}Si_2Te_9$. Displacement parameters of Na and Si were restricted to be equal.

atom	wyck. position	x	y	z	U_{eq} / Å^2
Na1	4a	0.095(3)	0.647(2)	0.026(3)	0.063(2)
Na2	4a	0.255(3)	0.740(3)	0.377(3)	0.063(2)
Na3	4a	0.652(3)	0.031(2)	0.452(2)	0.063(2)
Na4	4a	0.417(2)	0.048(2)	0.212(2)	0.063(2)
Na5	4a	0.673(2)	0.518(2)	0.197(2)	0.063(2)
Na6	4a	0.454(2)	0.547(2)	0.500(2)	0.063(2)
Na7	4a	0.499(3)	0.236(3)	0.110(2)	0.063(2)
Na8	4a	0.215(2)	0.853(2)	0.556(2)	0.063(2)
Na9	4a	0.083(3)	0.130(3)	0.632(3)	0.063(2)
Na10	4a	0.226(3)	0.729(3)	0.821(3)	0.063(2)
Si1	4a	0.511(2)	0.349(1)	0.347(2)	0.009(3)
Si2	4a	0.505(2)	0.855(2)	0.2962(1)	0.009(3)
Te1	4a	0.5521(5)	0.1891(6)	0.3218(5)	0.031(2)
Te2	4a	0.5388(5)	0.6885(6)	0.3513(5)	0.032(2)
Te3	4a	0.6657(6)	0.4297(7)	0.4222(5)	0.045(3)
Te4	4a	0.4293(6)	0.4322(6)	0.2165(5)	0.040(3)
Te5	4a	0.6618(6)	0.9330(6)	0.2418(5)	0.029(2)
Te6	4a	0.4378(6)	0.9281(6)	0.4690(5)	0.030(2)
Te7	4a	0.3740(6)	0.3483(6)	0.5076(5)	0.037(3)
Te8	4a	0.3632(6)	0.8473(6)	0.1779(5)	0.030(2)
Te9	4a	0.250(1)	0.1530(2)	0.0903(9)	0.044(1)

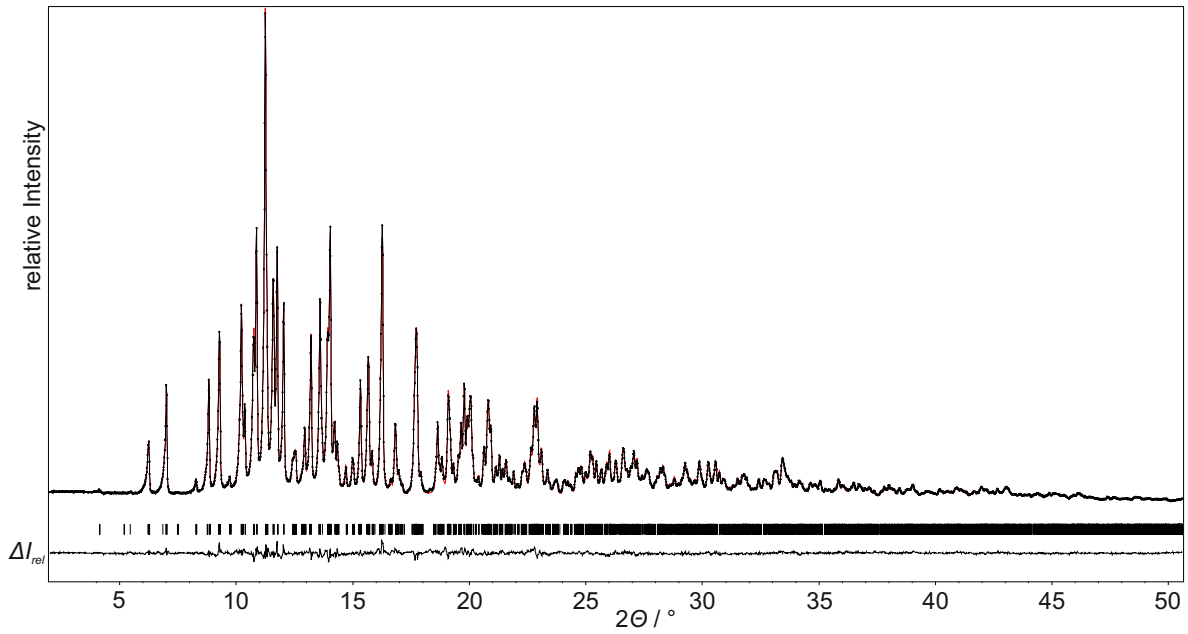

Figure C.6 Powder diffraction pattern of $Na_{10}Si_2Te_9$ with difference plot from Rietveld refinement. The diffraction pattern was measured with MoKα_1 radiation (λ = 0.7093 Å) at room temperature. For the structure refinement the structure model from single crystal diffraction was used.

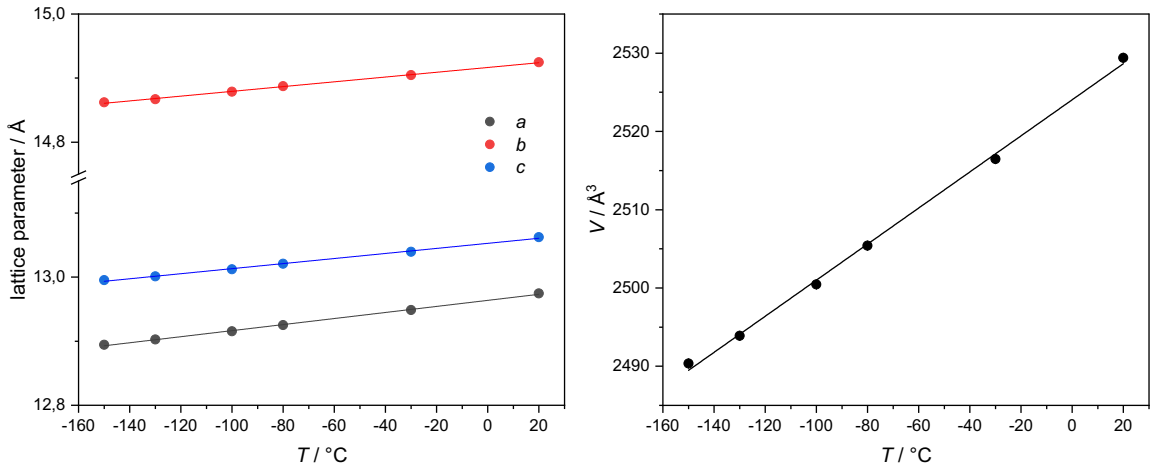

Figure C.7 Lattice parameters of $Na_{10}Si_2Te_9$ at different temperatures. The parameters were determined via le Bail refinement from powder X-ray diffraction patterns. The linear course indicates no phase transition of $Na_{10}Si_2Te_9$ in the investigated temperature range (−150 °C to 20 °C).

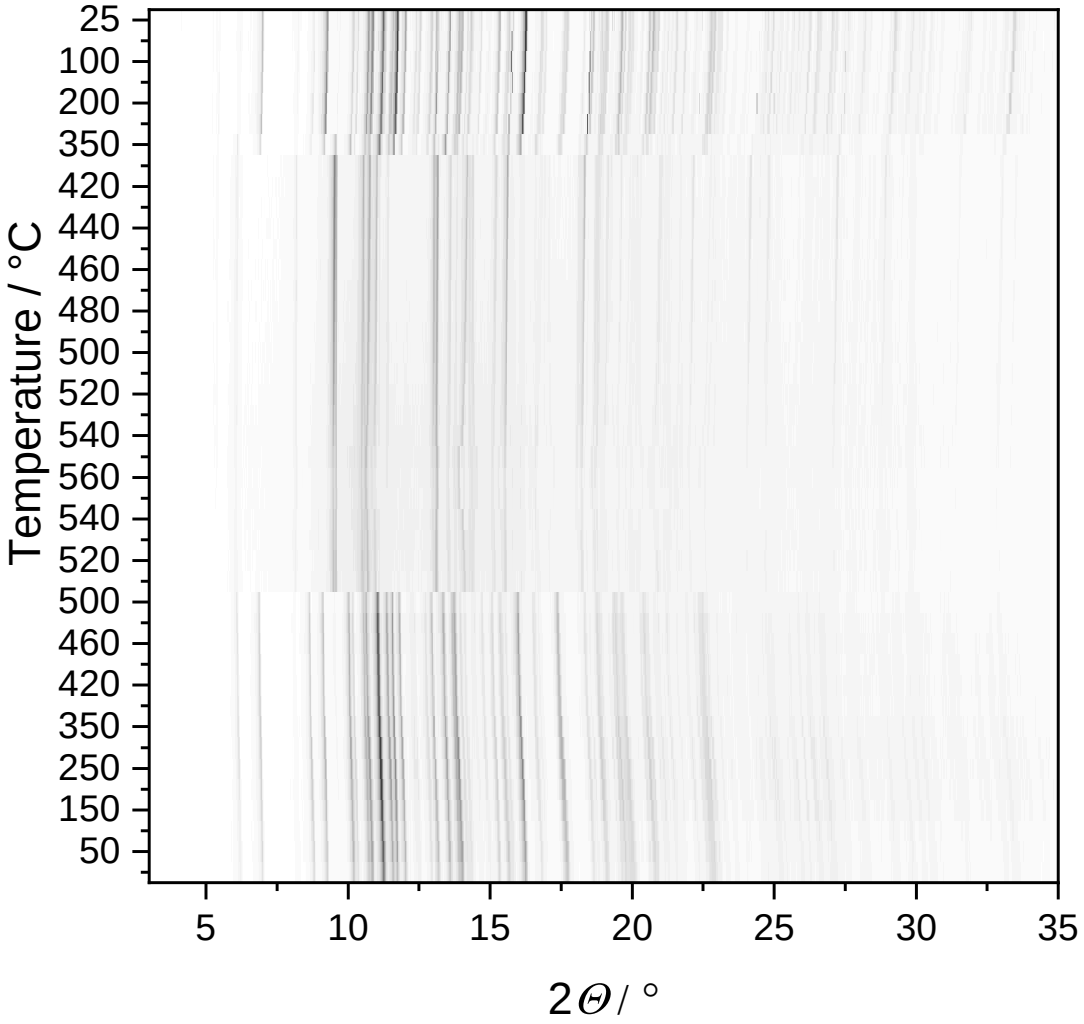

Figure C.8 In situ high-temperature X-ray powder diffraction of $Na_{10}Si_2Te_9$ in the temperature range of 25 °C to 560 °C. $Na_{10}Si_2Te_9$ is present up to 500 °C. By further heating it decomposes and $Na_6Si_2Te_6$ and Na_2Te is formed. Upon cooling, the partial reformation of $Na_{10}Si_2Te_9$ can be observed.

C.3 $Na_6Si_2Te_6$

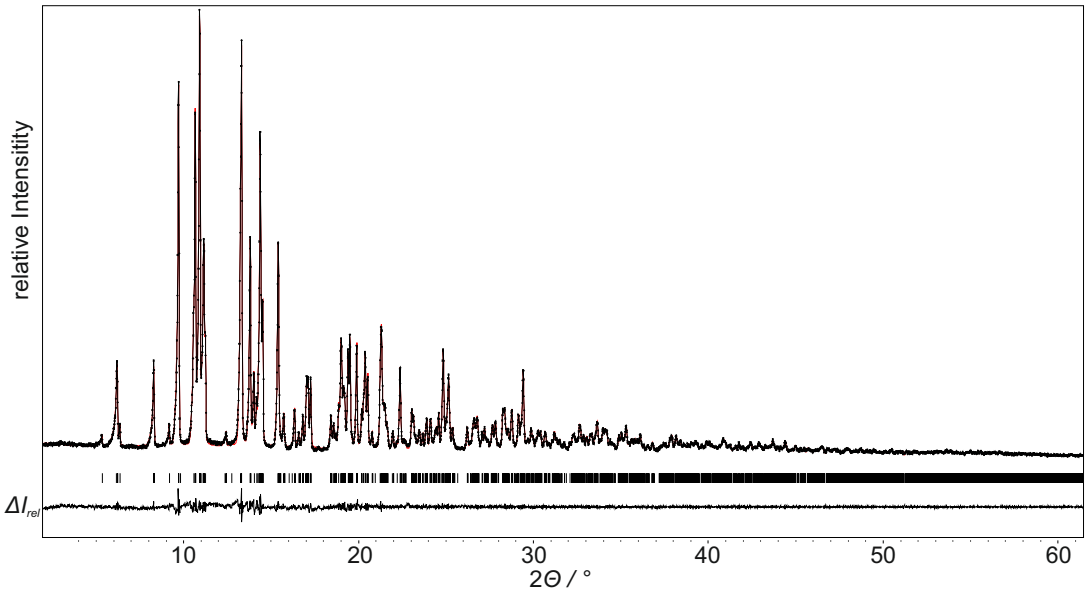

Figure C.9 Refined powder diffraction pattern of $Na_6Si_2Te_6$ with difference plot, measured with MoKα_1 radiation ($\lambda = 0.7093$ Å) at room temperature. For the le Bail refinement, the structure model of Eisenmann et al. was used.[2]

Table C.8 Unit cell parameters and R values from the refined powder diffraction pattern of $Na_6Si_2Te_6$.

	measured	literature[2]
a / Å	8.7789(1)	8.786
b / Å	12.7801(2)	12.78
c / Å	8.8657(2)	8.864
β / °	119.749(2)	119.71
V / Å^3	863.60(3)	864.46
GOF	1.03	
R_P, wR_P, wR_{exp}	0.0320, 0.0447, 0.0436	

C.4 $Na_8Si_4Te_{10}$

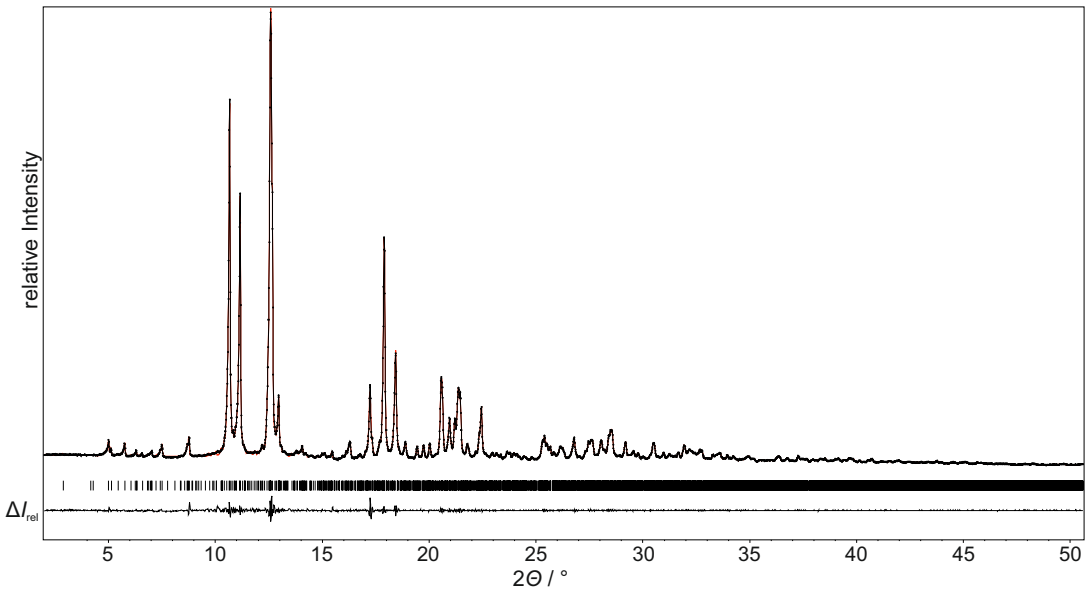

Figure C.10 Refined powder diffraction pattern of $Na_8Si_4Te_{10}$ with difference plot, measured with MoKα_1 radiation ($\lambda = 0.7093$ Å) at room temperature. For the le Bail refinement, the structure model of Eisenmann et al. was used.[3]

Table C.9 Unit cell parameters and R values from the refined powder diffraction pattern of $Na_8Si_4Te_{10}$.

	measured	literature[3]
a / Å	14.0843(2)	14.073
b / Å	12.8408(2)	12.842
c / Å	14.9389(3)	14.882
β / °	92.323(2)	92.22
V / Å^3	2699.54(9)	2687.54
GOF	1.73	
R_P, wR_P, wR_{exp}	0.0176, 0.0273, 0.0158	

C.5 Impedance Spectroscopy

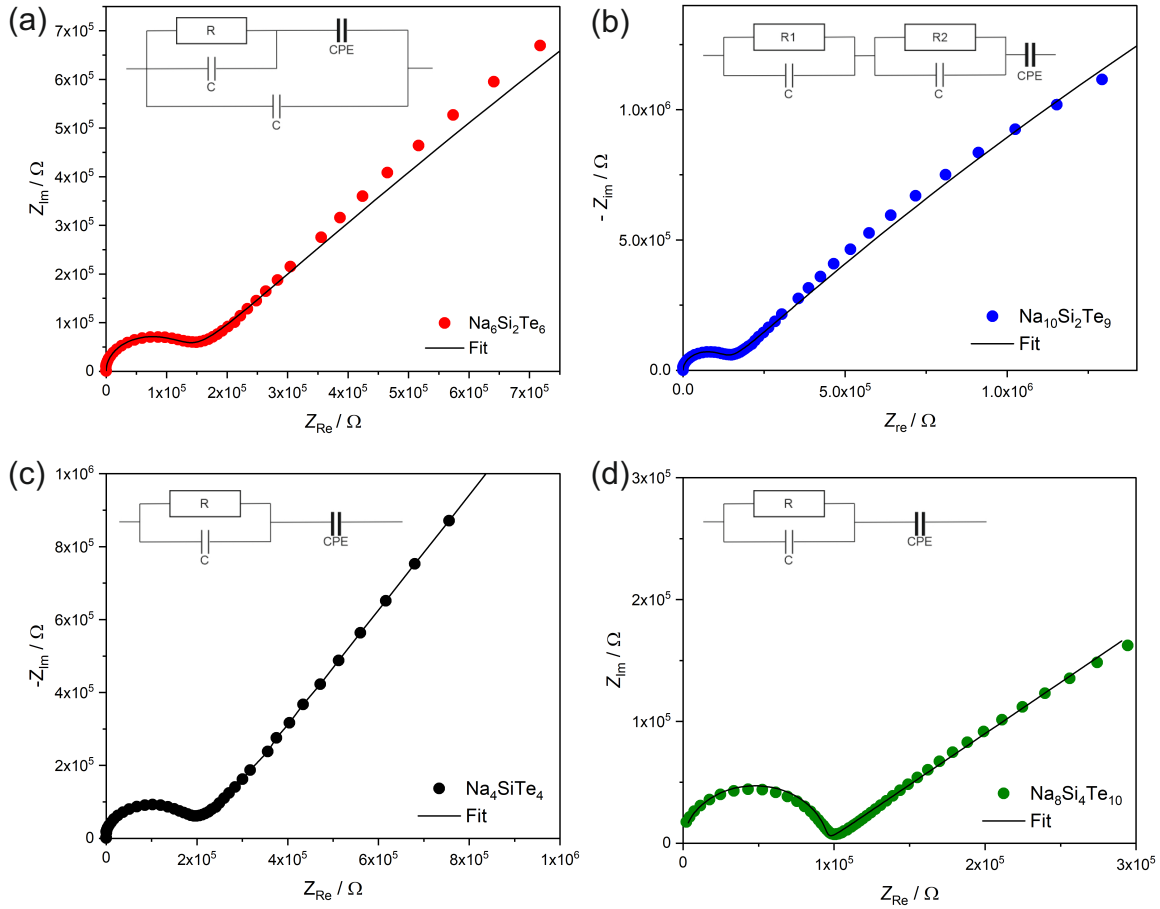

Figure C.11 Nyquist plots including fit at 100 °C for $Na_6Si_2Te_6$ (a), $Na_{10}Si_2Te_9$ (b), Na_4SiTe_4 (c) and at 200 °C for $Na_8Si_4Te_{10}$ (d). Corresponding equivalent circuits for fitting of the Nyquist plots are also included.

C.6 Calculation Details

Basis sets were taken from the literature.[4–6] All basis sets are available in the basis set library at the Crystal homepage. The outer shells were adjusted so that the calculated energy was minimized. The basis sets used are as followed:

Table C.10 Na basis set optimized for Na_4SiTe_4.

Na	exponent	contraction coefficient
$4sp$	0.1947	s: 1.0 p: 1.0
$3d$	0.1	1.0

Table C.11 Si basis set optimized for Na_4SiTe_4.

Si	exponent	contraction coefficient
$6sp$	0.1527	s: 1.0 p: 1.0
$3d$	0.3335	1.0

Table C.12 Te basis set optimized for Na_4SiTe_4.

Te	exponent	contraction coefficient
$5d$	0.2888	1.0

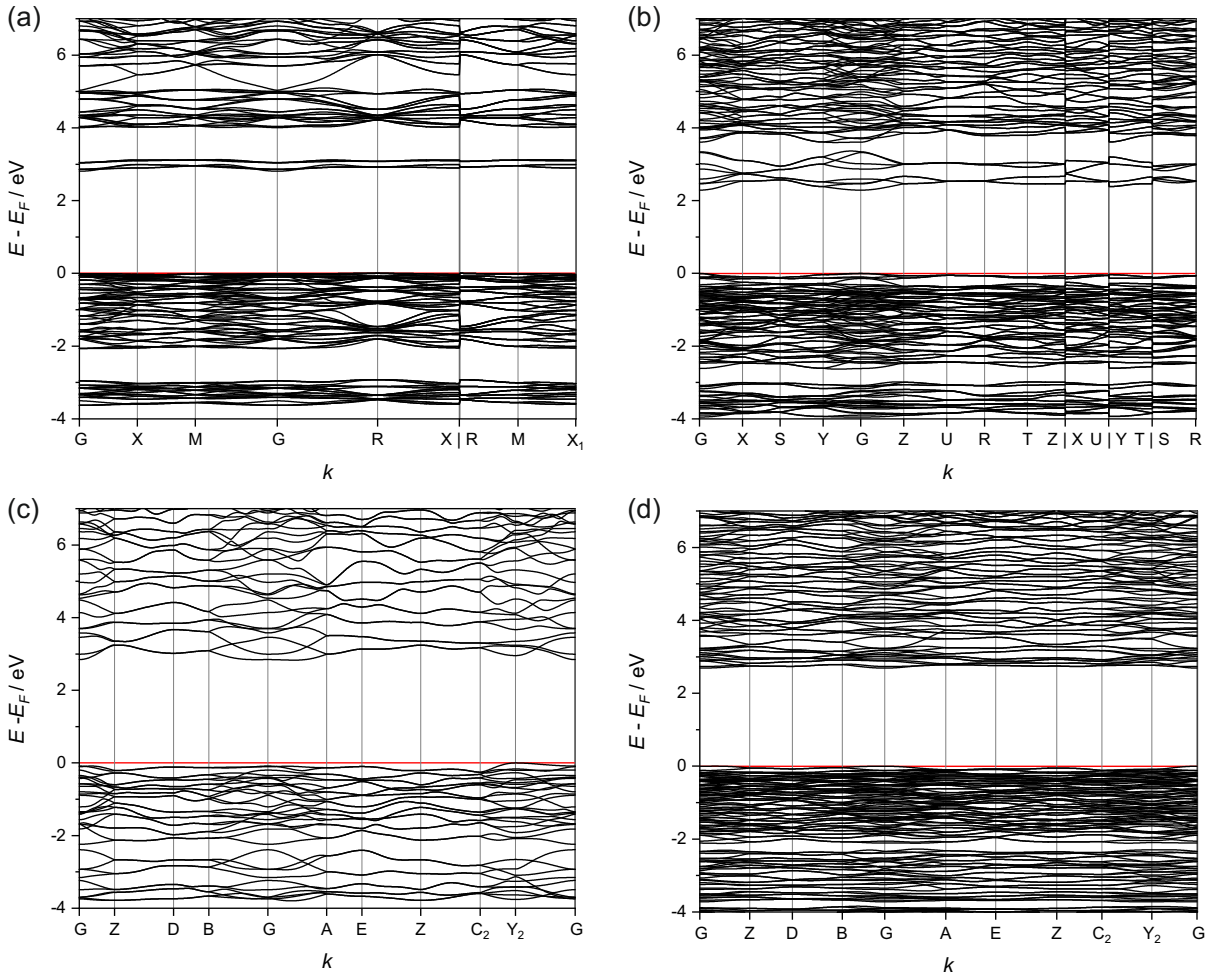

Figure C.12 Calculated band structures of (a) Na_4SiTe_4, (b) $Na_{10}Si_2Te_9$, (c) $Na_6Si_2Te_6$ and (d) $Na_8Si_4Te_{10}$.

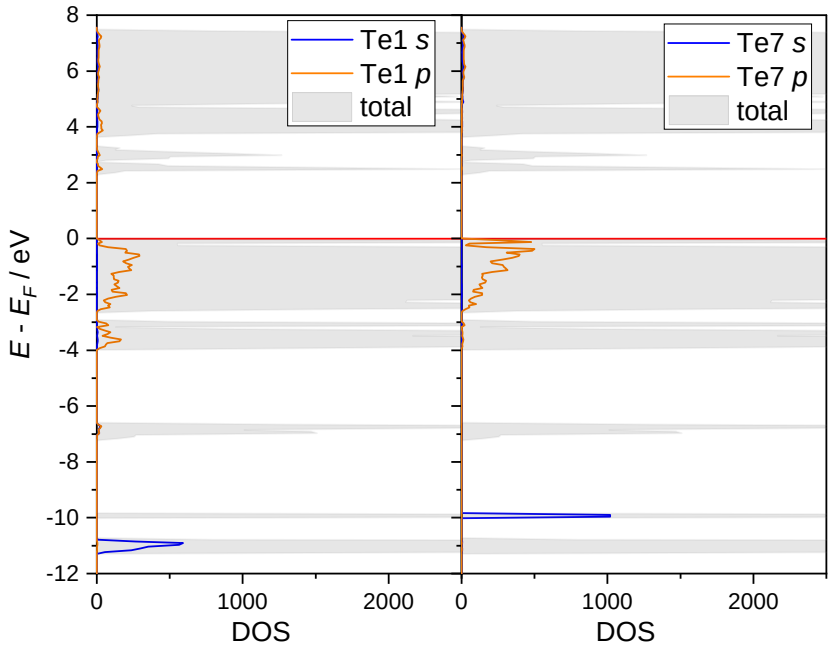

Figure C.13 Orbital projected density of states for Te1 and Te7 in $Na_{10}Si_2Te_9$.

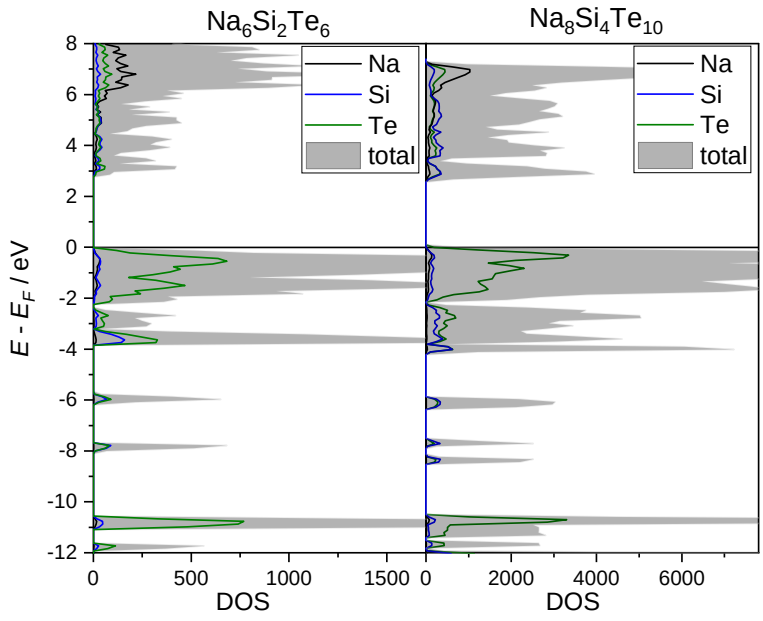

Figure C.14 Electronic DOS of $Na_6Si_2Te_6$ and $Na_8Si_4Te_{10}$.

References

[1] CrysAlisPro (V42); Rigaku Oxford Diffraction Ltd, 2019.

[2] Eisenmann, B.; Schwerer, H.; Schäfer, H. *Z. Naturforsch. B* **1981**, *36*, 1538–1541.

[3] Eisenmann, B.; Schwerer, H.; Schäfer, H. *Rev. Chim. Minér.* **1983**, *20*, 78–87.

[4] Sophia, G.; Baranek, P.; Sarrazin, C.; Rerat, M.; Dovesi, R., `https://www.crystal.unito.it/Basis_Sets/sodium.html`, Accessed: 2023-03-06, 2014.

[5] Porter, A. R.; Towler, M. D.; Needs, R. J. *Phys. Rev. B* **1999**, *60*, 13534–13546.

[6] Heyd, J.; Peralta, J. E.; Scuseria, G. E.; Martin, R. L. *J. Chem. Phys.* **2005**, *123*, 174101.